# Fe-based composite materials with advanced mechanical properties

DISSERTATION

zur Erlangung des akademischen Grades

Doktoringenieur
(Dr.-Ing.)

vorgelegt

der Fakultät Maschinenwesen
der Technischen Universität Dresden

von

M. Sc. Katarzyna Werniewicz
geb. am 13.08.1978 in Warschau, Polen

05.01.2010, Dresden

*"All truths are easy to understand once they are discovered;*

*the point is to discover them"*

**Galileo Galilei**

*… to my mother*

*… dla mojej najukochańszej mamy*

**Katarzyna Werniewicz**

# Fe-based composite materials with advanced mechanical properties

# TABLE OF CONTENTS

# ABSTRACT

*In a word...*

In this study a series of novel Fe-based materials derived from a bulk metallic glass-forming composition was investigated to improve the ductility of this high-strength glassy alloy. The interplay between the factors chemistry, structure and resulting mechanical properties was analyzed in detail. It has been recognized that subtle modifications of the chemical composition (carbon addition) lead to appreciable changes in the phase formation, which occurs upon solidification (from *a single-phase structure* to *composite materials*). As a consequence, significant differences in the mechanical response of the particular samples have been observed.

The materials developed here were fabricated by centrifugal casting. To explore the structure features of the as-cast cylinders, manifold experimental techniques (X-ray diffraction, optical, as well as electron microscopy) were employed. The occurrence of the numerous reflections on the X-ray diffraction patterns has confirmed the crystalline nature of the studied Fe-based alloy systems. The subsequent extensive research on their deformation behavior (Vickers hardness and room temperature compression tests) has revealed that, although the glass-forming ability of the investigated compositions is not high enough to obtain a glassy phase as a product of casting, excellent mechanical characteristics (high strength - **comparable to that of the reference bulk metallic glass (BMG)** - associated with good ductility) were achieved for the "composite-like" alloys. In contrast, the single phase cylinders, subjected to compressive loading, manifested an amazing capacity for plastic deformation – no failure occurred.

The fracture motives developed during deformation of the "composite-structured" samples were studied by scanning electron microscopy. The main emphasis has been put on understanding the mechanisms of crack propagation. Owing to the structural complexity of the deformed samples, it was crucial to elucidate the properties of the individual compounds. Based on the obtained results it was concluded that the coexistence of a soft f.c.c. γ-Fe phase in combination with a hard complex matrix is responsible for the outstanding mechanical response of the tested composites. While the

soft particles of an austenite contribute to the ductility (they hinder the crack propagation and hence, cause unequivocal strain-hardening), the hard constituents of the matrix phase yield the strength.

*More detail…*

To ascertain the effect of the fabricating route on the phase formation and the deformability of the multi-component $Fe_{81.2}Cr_{5.2}Mo_{5.2}Ga_{5.2}Si_{3.2}$ and $Fe_{78.0}Cr_{5.2}Mo_{5.2}Ga_{5.2}Si_{6.4}$ alloys, two different crucible materials were used ($Al_2O_3$ and glassy carbon). Significant changes in the microstructure for the differently prepared as-cast rods have been observed. Generally, the samples manufactured by using a ceramic crucible exhibit a single-phase microstructure (b.c.c. $\alpha$-Fe), whereas the cylinders prepared by employing a glassy carbon crucible show the composite structure formation. The origins responsible for such dissimilarities are attributed to the presence of carbon, which diffuses from the crucible into the molten alloy. Together with the structure evolution from a single-phase to a complex multi-phase material, a great improvement of the mechanical properties was achieved. The reported fracture strengths $\sigma_f$ for the compressed composites are 2.9 GPa and 3.2 GPa, respectively. The corresponding values of fracture strain are found to be 13% and 6%. On the basis of fracture analysis results it can be claimed that the combination of high strength and good ductility results from the special interplay between soft and hard constituents of the structure.

To evaluate the carbon influence on the deformation mode, $(Fe_{84.4}Cr_{5.2}Mo_{5.2}Ga_{5.2})_{91}C_9$[1] and $(Fe_{84.4}Cr_{5.2}Mo_{5.2}Ga_{5.2})_{83}C_{17}$ composite alloys have been prepared. It has been recognized that, with increasing carbon content, the ductility of the investigated alloys decreases from $\varepsilon_f = 36\%$ to $\varepsilon_f = 16\%$. In strong contrast, the apparent fracture strength is nearly the same, i.e. $\sigma_f = 2.8$ GPa and $\sigma_f = 3.03$ GPa, respectively. While the obtained values of fracture strength are similar to data reported for the

---

[1] Please note that this expression is not rigorous – it should be $(Fe_{0.844}Cr_{0.052}Mo_{0.052}Ga_{0.052})_{100-x}C_x$. Nevertheless, it is more convenient and common to write a chemical composition in a simplified form. Following this habit, throughout the thesis the following expression is used $(Fe_{84.4}Cr_{5.2}Mo_{5.2}Ga_{5.2})_{100-x}C_x$ (x = 9,17 at.%).

reference $Fe_{65.5}Cr_4Mo_4Ga_4P_{12}C_5B_{5.5}$ BMG ($\sigma_f$ = 3.27 GPa), the values of fracture strain are greatly improved for the studied crystalline materials.

The structural observations have affirmed the previously discussed results. The coexistence of a ductile Ga-enriched dendritic phase dispersed in a high strength Cr- and Mo-enriched matrix was ascertained. Due to this fact, the resulting mechanical behavior can be explained as being due to the formation of a composite material with a specific complex crystalline structure.

To investigate the Ga effect on the microstructure and the mechanical response, Ga-free composite materials with overall compositions $(Fe_{89.0}Cr_{5.5}Mo_{5.5})_{91}C_9$[2] and $(Fe_{89.0}Cr_{5.5}Mo_{5.5})_{83}C_{17}$ were fabricated. It was expected that the modifications of the chemical composition will lead to changes in the microstructure and, obviously, in the mechanical response of the alloys. Surprisingly, the combined results obtained from the present as well as previous investigations clearly indicate that the Ga substitution does not cause tremendous differences in the phase formation, which occurs upon casting. However, for the alloys with higher C concentration, it was found that Ga additions lead to a significant improvement of the plasticity. While the as-cast $(Fe_{89.0}Cr_{5.5}Mo_{5.5})_{83}C_{17}$ rod sustains about 5% strain up to failure, its Ga-containing counterpart shows about 16% strain in the compression test ($\varepsilon_f$ is three times higher). On the other hand, for both alloys the achievable strength at fracture is nearly the same, i.e. $\sigma_f$ = 3.3 GPa for $(Fe_{89.0}Cr_{5.5}Mo_{5.5})_{83}C_{17}$ and $\sigma_f$ = 3.03 GPa for $(Fe_{84.4}Cr_{5.2}Mo_{5.2}Ga_{5.2})_{83}C_{17}$. These findings can be explained as being due to the specific interaction between the soft $\gamma$-Fe dendrites and the hard interdendritic phases, as observed for the Fe-based compositions. In the case of the previous alloys as well as the $(Fe_{89.0}Cr_{5.5}Mo_{5.5})_{91}C_9$ alloy, the ductile dendritic phase acts as an obstacle for the crack propagation and, therefore, causes the pronounced strain-hardening. These composites are characterized by their excellent mechanical properties: high strength (from the matrix) connected with very good plasticity (from the dendrites). Contrary, such a strengthening effect has not been observed for the as-cast

---

[2] Please note that this expression is not rigorous – it should be $(Fe_{0.89}Cr_{0.055}Mo_{0.055})_{100-x}C_x$. Nevertheless, it is more convenient and common to write a chemical composition in a simplified form. Following this habit, throughout the thesis the following expression is used $(Fe_{89.0}Cr_{5.5}Mo_{5.5})_{100-x}C_x$ (x = 9,17 at.%).

$(Fe_{89.0}Cr_{5.5}Mo_{5.5})_{83}C_{17}$ rod. The detailed studies on its fracture behavior have revealed that the cracks initiated during plastic deformation proceed through the austenitic phase. The soft γ-Fe dendrites do not hinder crack propagation. Taking into account all results demonstrated, it is evident that only appropriate alloying additions (Ga and C) lead to the improvement of the mechanical properties of the complex Fe-based materials developed here.

Summarizing, the mechanical characteristics, as reported for the investigated alloys, are superior compared to the monolithic reference BMG.

# List of symbols and abbreviations

| | |
|---|---|
| (B)MG | (Bulk) Metallic Glass |
| BAS | Bulk Amorphous Steel |
| DSC | Differential Scanning Calorimetry |
| $G$ | Gibbs Free Energy |
| XRD | X-Ray Diffraction |
| SEM | Scanning Electron Microscopy |
| TEM | Transmission Electron Microscopy |
| EDX | Energy Dispersive X-ray Spectroscopy |
| WDX | Wave-Length Dispersive X-ray Spectroscopy |
| $RT$ | Room Temperature |
| $T$ | Temperature |
| $T_l$ | Liquidus Temperature |
| $T_s$ | Solidus Temperature |
| $T_m$ | Melting Temperature |
| $M_s$ | Starting Temperature of Martensitic Transformation |
| b.c.c. | Body-Centered Cubic |
| f.c.c. | Face-Centered Cubic |
| b.c.t. | Body-Centered Tetragonal |
| $E$ | Young's Modulus |
| $\sigma_y$ | Yield Strength |
| $\varepsilon_y$ | Yield Strain |
| $\sigma_f$ | Fracture Strength |
| $\varepsilon_f$ | Fracture Strain |
| $\varepsilon_{pl}$ | Plastic Strain |
| $HV$ | Vickers Microhardness |
| GFA | Glass Forming Ability |
| SCL | Supercooled Liquid |
| $T_g$ | Glass Transition Temperature |

| | |
|---|---|
| $T_x$ | Crystallization Temperature |
| $R_c$ | Critical Cooling Rate |
| SRO | Short Range Order |
| LRO | Long Range Order |
| PDF | Pair Distribution Function |
| MA | Mechanical Alloying |
| QC | Quasi-Crystal |
| STZ | Shear Transformation Zones |

# CHAPTER 1

# Introduction

As we begin the $21^{st}$ century, we find ourselves fully in the age of technology. Due to the rising human requirements, everything is getting better, faster and more convenient. Obviously, the further progress in the field of technology is strongly related to the development of novel materials with unique functional and structural properties.

One of civilisation's most important and highly-developed engineering materials is steel. According to Branagan [Bra05] steel is defined as any Fe-based alloy in which no other single element is present in excess of 30 wt.%, the iron content amounts to at least 55 wt.% while the amount of carbon is limited to a maximum value of 2 wt.%. Based on historical notes, steel was already known in antiquity. Some of the first steel brands come from East Africa, dating back to 1400 BC[3] [Hoo96]. Due to its cost-efficient production in tremendous amounts associated with broad and rather readily tunable properties, more than 2000 steel brands have been evolved up to date [Sta]. However, the human thought has not only been limited to manufacturing crystalline materials. Among the discoveries crucial for the civilization as well as for the advancement of the materials science field *glass* plays a special role. Glassmaking is thought to have begun in Mesopotamia about 2500 BCE[4] with the fashioning of beads in imitation of precious stones [Gre07]. The early knowledge on fabricating the sharp cutting edges made of obsidian (the best known natural glass) has successfully been used for the construction of the first tools and weapons: e.g. knives, arrowheads and spears. Although the glassy materials have such a long history of usage, there is still lack of a universal definition for the glassy state. The details regarding the nature of a glass as well as "Under what conditions can a glass be formed?" [Duw60, Tur69] will be presented in chapter 2 "**Theoretical principles**".

---

[3] BC – Before Christ
[4] BCE – Before the Common Era

However, what kind of effect can be expected when the features characterizing the conventional metallic alloys will meet those of the glasses? The answer is simple: metallic glass formation will be observed. When in 1960 Klement, Willens and Duwez synthesized the first metallic glass – $Au_{75}Si_{25}$ [Kle60], the classical theories describing the structures of conventional solid metallic states had to be verified [Cot55]. Duwez and his co-workers have demonstrated that under certain conditions the formation of the crystalline periodic structure typical for metals can be suppressed [Duw60]. By employing the rapid solidification technique small amounts of molten alloy were cooled at rates high enough ($\approx 10^6$ $Ks^{-1}$) to bypass the nucleation and growth of equilibrium phases. Instead of the well-known ordered state, a highly disordered arrangement of the atoms in the solidified Au-Si alloy system was observed [Duw60].

*Metallic glass* (glassy alloy or amorphous alloy) – a metastable alloy, which lacks the
*(MG)* transitional symmetry typical of crystalline materials and retains its amorphous liquid-like structure at room temperature [Kle60].

Shortly after this decisive discovery, Turnbull and Cohen pointed out that the occurrence of the glassy phase in $Au_{75}Si_{25}$ can mainly be attributed to the specific alloy composition being close to a deep eutectic [Coh61]. By choosing an alloy in the vicinity of the eutectic composition, the melt could be cooled to a temperature at which its viscosity is quite high (low atomic diffusivity) and, therefore, the stability of the metallic liquid is sufficient to prevent the crystal nucleation. As a result of the above-mentioned remarks, a number of various glass-forming metallic systems have subsequently been reported: Pd-Si [Duw65], Nb-Ni [Ruh67], Fe-C-P [Duw67] and Zr-TM [TM = Ni, Pd, Cu, Co] [Ray68].

The pioneering work of Duwez *et al.* as well as the further contributions made by Turnbull and Cohen [Coh61, Tur69] have opened a new chapter in the history of materials science. The appearance of a novel class of metallic alloys with a unique non-crystalline structure has attracted an intense interest of the scientific community. It was assumed that such disordered atomic structures may offer a range of outstanding physical and technological properties. The primary studies were mainly focused on the magnetic

behavior of the "*mysterious*" glassy alloys. The discovery of an amorphous ferromagnetic phase in the ternary Fe-C-P system [Duw67] resulted in the development of a series of transition metal – metalloid glass-forming compositions with a good soft magnetic performance. Moreover, the mechanical testing carried out for selected amorphous alloys in the 1970s [Che70, Mas71, Pam74a, Pam74b] and 1980s [Don89] has revealed their impressive suite of mechanical characteristics. Due to the absence of well-defined dislocation faults typical for conventional crystalline metals, an excellent failure strength approaching theoretical values was observed. Furthermore, while most of the engineering materials exhibit elastic strains of 0.2% or less, amorphous alloys are able to sustain up to 2.0% of elastic deformation. In addition to the above-discussed features, an extremely high corrosion resistance was reported for chosen glassy systems [Mas78].

However, the ambition of scientists for understanding the glass-formation phenomenon as well as for finding a universal model describing their structure and, finally, exploring their physical, mechanical and chemical properties could not have been satisfied yet. The major problem, which severely limited the progress of research on the metallic glasses (MGs) arose from the extremely high cooling rates ($10^5 – 10^7$ Ks$^{-1}$) required for retaining the glassy state. Therefore, the samples obtainable (ribbons, wires and droplets) were very small and sometimes irregular in shape. This drawback in turn strongly restricted their possible applications as structural materials.

Hence, the next logical step was to search for alloy compositions with a higher glass-forming ability (GFA). The success came in 1969, when Chen and Turnbull were able to prepare fully amorphous spheres of Pd-Si-M (M = Ag, Cu or Au) [Che69]. It has been found that the composition $Pd_{77.5}Cu_6Si_{16.5}$ can be cast into the glassy state with a diameter of 0.5 mm. Furthermore, the high resistance to crystallization of the investigated alloy ($\Delta T_x^5$ = 40 K) made possible the first detailed research on the crystallization behavior of MGs. However, the vision about the synthesis of an amorphous alloy with a dimension exceeding 10 mm came true several years later [Kui84]. By processing the $Pd_{40}Ni_{40}P_{20}$ melt in a boron oxide flux, a 10 mm-diameter-ingot was achieved. The mile step has been made. The age of Bulk Metallic Glasses (BMGs) had been started.

---

[5] $\Delta T_x = T_x – T_g$, the supercooled liquid region, i.e. the temperature difference between the crystallization temperature $T_x$ and the glass transition temperature $T_g$.

# Introduction

A great contribution to the advancement of the alloy compositions able to give bulk metallic glasses has been done by the Japanese research group headed by A. Inoue. Their systematic search for bulk glass formation in multi-component alloy systems succeeded in the discovery of numerous glassy materials. The studies on ternary and quaternary La- [Ino89, Ino90a], Mg- [Ino91] and Zr-based alloys [Ino90b, Zha91] revealed their exceptional GFA. For instance, in the case of Zr-Al-Ni-Cu glasses, the critical casting thickness achievable ranges up to 16 mm [Ino93a]. In particular, for the $Zr_{65}Al_{7.5}Ni_{10}Cu_{17.5}$ alloy an extremely large supercooled liquid region $\Delta T_x$ of 127 K was noticed [Zha91].

*Supercooled liquid region*     – difference between crystallization temperature $T_x$ and glass transition temperature $T_g$ ($\Delta T_x = T_x - T_g$).

Following Inoue's work, in 1993 Peker and Johnson at Caltech developed the $Zr_{41.2}Ti_{13.8}Cu_{12.5}Ni_{10.0}Be_{22.5}$ BMG, commonly referred to as Vitreloy1. By employing classical metallurgical casting methods (cooling rates $< 10$ $Ks^{-1}$), rod-shaped specimens up to 14 mm in diameter were fabricated [Pek93]. The key idea used to design the alloys with a good glass-forming ability was based on a specific element(s) selection. It was assumed that the enhancement of the thermal stability of $\Delta T_x$ may be obtained by choosing the constituent components with a significant difference in the atomic size ratio leading to an efficient packing density of the amorphous phase [Zha91, Ino93b, Pek93]. Soon after, a great expansion of the Be-comprising glassy alloys was observed. It has been recognized that such materials can be cast as rods with thicknesses ranging from 5 to 10 cm [Joh99]. Up to date, many complex alloy systems based on e.g. Zr [Gil97, Küh00, Löf00, Eck01], Ti [Fuj06, Cal07, Zha07], Cu [Fuj06, Zha07], Ni [Liu07, Li08], Fe [She99, Ino04a, Ino04b, Pon04, Sto05a, Sto08], Pd [Ino96, Ino97], La [Tan03], Pt [Sch04] and Mg [Kim90, Par05, Zha07], that retain a glassy structure in bulk form through conventional casting, have been generated. This, in turn, has caused a significant increase of the engineering importance for glassy metallic alloys.

# Introduction

## Fe-based bulk metallic glasses – *the subject of the interest*

Among BMG systems discovered so far, Fe-based glass formers play a special role. They are well known for their outstanding properties, such as high yield and fracture strength, high hardness, good corrosion resistance as well as excellent soft magnetic properties. Compared to other glass-forming systems, e.g. Zr- and Ti-based compositions, Fe-based glassy alloys show a superior fracture strength. It has been reported that their strength values can be in the range of 2.8 – 4.0 GPa [Ino04a, Ino04b, She05, Sto05a, Gu07], whereas the Zr- and Ti-based glasses show lower fracture strength of about 2 GPa [Eck07a, Cal07]. This unique combination of engineering features makes Fe-based BMGs a very attractive candidate for future structural and functional applications [Ino01, Pon03, Ino04b, Lu04]. Since the first synthesis of a ferrous amorphous material in Fe-(Al,Ga)-metalloid system in 1995 [Ino95], a range of new Fe-based glassy alloys has been manufactured [She99, Ino04b, Lu04, Pon04, Sto08]. In contrast to earlier compositions, recently reported ferrous BMGs can be processed into amorphous rods of more than 1 cm diameter [Pon04, Lu04, She05]. By tuning the chemistry of the Fe-based glassy alloys (rare earth element additions: Y, Er or Tm) a substantial enhancement of their GFA was noticed. The largest critical size ($\varnothing$ = 16 mm) has been achieved for the multi-component $Fe_{41}Co_7Cr_{15}Mo_{14}C_{15}B_6Y_2$ alloy system [She05].

A great impact on the development of ferrous BMGs has been given by Ponnambalam and co-workers [Pon03, Pon04]. The studies carried out by the Virginia group resulted in the invention of the so-called bulk amorphous steels (BASs). Such a "new generation of steels" was found to exhibit a failure strength exceeding twice that assessed for their high-strength crystalline counterparts. Along with their excellent mechanical behavior, interesting physical and magnetic properties as well as a high thermal stability were observed for these amorphous steels [Pon04, Lu04].

Unfortunately, although the strength of ferrous glassy alloys is very high, their widespread application as structural components is strongly inhibited by a very low level of macroscopic plasticity and the absence of strain-hardening. Consequently, upon loading such materials undergo work-softening, which results in a localization of plastic deformation into shear bands. Therefore, if the operating stress exceeds the elastic limit,

the MGs fail spontaneously on one or a few dominant shear bands without appreciable strain [Ino04a]. To circumvent the limited ductility of the BMGs, the idea of designing two-phase composites has been proposed and realized [Hay00]. It has been recognized that the formation of a heterogeneous microstructure composed of a glassy matrix with second phase dispersions leads to a drastic enhancement of the compressive strain without an appreciable drop in strength. By altering the compositions of Zr-, Ti-, and Co-based glassy alloys, novel in-situ cast composite materials were developed [Hay00, Küh02, Das03a, Das03b, He03a, Eck07b, Wan06]. In addition, the formation of a new ductile Fe-Ni-Zr-Cr-Si-B composite-type BMG was recently reported by Lee *et al.* [Lee06]. It was proven that the plasticity of such an alloy system improves *"…when only a slight amount of a few nano-sized crystals are isolated and homogeneously dispersed in the amorphous matrix.*" Following the above-given hints, the purpose of this work was to develop BMG Fe-based composite materials with highly enhanced ductility. The studied materials were derived from the monolithic $Fe_{65.5}Cr_4Mo_4Ga_4P_{12}C_5B_{5.5}$ glassy alloy [She99, Sto05a]. The major emphasis was placed on understanding the interplay between selected chemical compositions, their influence on the evolution of the as-cast microstructure and, finally, on the mechanical response of the examined specimens.

Owing to the variety of structures explored in these studies – *from crystals to non-crystalline structures* as well as *from monolithic materials to complex systems*, some fundamental information on the nature of glassy and crystalline states will be given. Furthermore, the consequences of the microstructural changes – *deformation behavior of conventional ordered metallic alloys versus disordered metallic glasses* will be illustrated (chapter 2 "**Theoretical principles**"). The aspects regarding the alloy selection as well as the detailed description of the experimental techniques employed during the research work are outlined in chapter 3 "**Materials – *processing and characterization***". The systematic search for new high-strength and ductile Fe-based composite alloys derived from the $Fe_{65.5}Cr_4Mo_4Ga_4P_{12}C_5B_{5.5}$ BMG is widely discussed in chapter 4 entitled "**Results and discussion**". The brief summary of the carried out research along with some comments concerning future directions of the studies on the fabrication of the MG-derivative complex structures with superior mechanical properties are given in chapter 5 "**Concluding remarks and future trends**".

# CHAPTER 2

## Theoretical principles –       *from crystals to non-crystalline structures*

This chapter provides some basic principles concerning the "old" crystalline metallic materials and their newly developed glassy counterparts. Especially, a set of conditions that must be satisfied to achieve particular states will be discussed. In addition, the transformation from monolithic amorphous alloys to glass matrix composites containing crystalline phase dispersions – **composite strategy** – will be shortly reviewed. Moreover, due to the well known fact that the structure affects the properties of the material, a comparison between the deformation behavior of metallic glasses and that of their crystalline counterparts will be conducted. Finally, considering a complex microstructure (BMG-matrix composite), its superiority for enhancing strength, plasticity, and toughness will be illustrated.

### 2.1 Metallic materials in crystalline and in glassy state

According to the theory of liquids, a liquid may solidify in two ways: either discontinuously to a crystalline solid or continuously to an amorphous solid or glass [Tur61]. The main feature, which distinguishes them from one another, is their atomic-scale structure. The essential differences in the atomic arrangement in a particular state are displayed in Figure 2.1.1.

In a crystalline solid (Figure 2.1.1a), the atomic positions repeat in space in a regular array. This characteristic structural property of crystals is called long-range order (LRO) or transitional periodicity. In contrast, as indicated in Figure 2.1.1b, in glassy solids such a three-dimensional periodicity is absent. However, a closer insight into the solid structure reveals that both solid states, crystalline and amorphous, exhibit the so-called short-range (atomic-scale) order (SRO). Its existence is a consequence of the chemical bonding between atoms, which is responsible for holding the solid together [Cot55, Ask03].
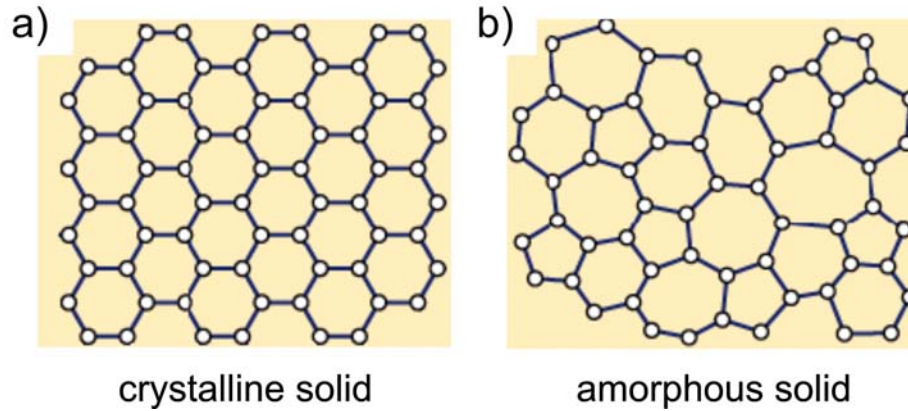
**Figure 2.1.1.**    Atomic arrangement in a) a crystal and b) an amorphous solid [Kit05].

- Description of the crystalline state

In the crystalline state the atoms (or groups of atoms or "motives") are arranged in a pattern that repeats periodically in three dimensions to an infinite extent [Ell90]. According to the above-given definition, an imperfect crystal can simply be one which is finite and ends at surfaces, or one which contains one or more defects. It is well known, that most crystalline materials possess a variety of crystallographic defects, e.g. vacancies of interstitial foreign atoms, dislocations, grain boundaries, etc. The origin of these imperfections can be manifold: deformation of the solid, rapid cooling from high temperatures or high-energy radiation (X-rays or neutrons) striking the crystal. Situated at single points (e.g. vacancies, interstitials, impurities), along lines (e.g. dislocations), or on entire surfaces (grain boundaries, anti phase boundaries), such defects strongly affect the mechanical, electrical as well as optical properties of a crystal (Woll05, New05).

The comprehensive discussion of the aspects associated with the interplay between the material's microstructure and its mechanical response will be a subject of section 2.2. However, before the s*tructure – mechanical behavior relationships* will be discussed, the particulars of the atomic arrangement occurring in conventional crystalline materials as well as the formation of a glassy state will be presented.

*Periodic crystal structure*

The crystal structure can be represented by its *unit cell*, which is a tiny box composed of one or more motives – spatial arrangement of atoms. By setting one unit cell on another, the crystal pattern can be built up. All corners of such a framework of unit cells construct a point *lattice* in the point space (Figure 2.1.2a) [Ste05].



a)                              b)                              c)
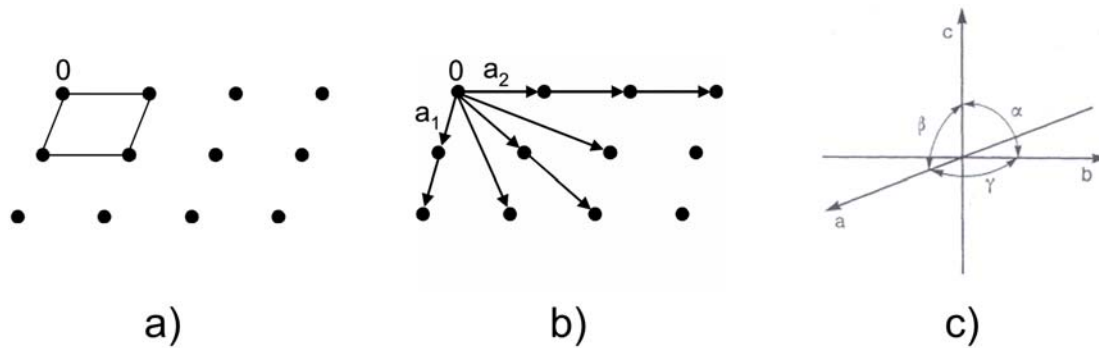
**Figure 2.1.2.**   Illustration of the point lattice with one unit cell (a) and the vector lattice (b) [Ste05]. The unit cell can be defined by using a parallelepiped with lengths *a*, *b*, *c* and angles between the sides given by *α*, *β*, *γ* (c) [Kit05, Ste05].

By decorating these lattice points with groups of atoms, a lattice array of atom groups can be formed. Furthermore, by changing to vector space and considering the lattice points as endpoints of vectors resulting from the origin of the coordinate system, a *vector lattice r* can be obtained (Figure 2.1.2b). The relationship between a lattice vector and a basis ($a_1 \dots a_m$) is given by the following expression [Ste05]:

$$r = n_1 a_1 + \dots + n_m a_m \, ,$$   (2.1)

with $m = 3$ for regular crystals.

As displayed in Figure 2.1.2c, each unit cell is characterized by the length of the cell edges (indicated as *a*, *b*, *c* in Figure 2.1.2c) and the angles between them ($\alpha$, the angle between *b* and *c*; $\beta$, the angle between *a* and *c*; $\gamma$, the angle between *a* and *b* [Kit05, Ste05]). The positions of the atoms inside the unit cell are defined by the set of atomic positions ($x_i$, $y_i$, $z_i$) determined from a given lattice point. The unit cell, which does not comprise any lattice points in the interior, is called primitive. The volume of all eventual primitive unit cells of a given lattice is the same.



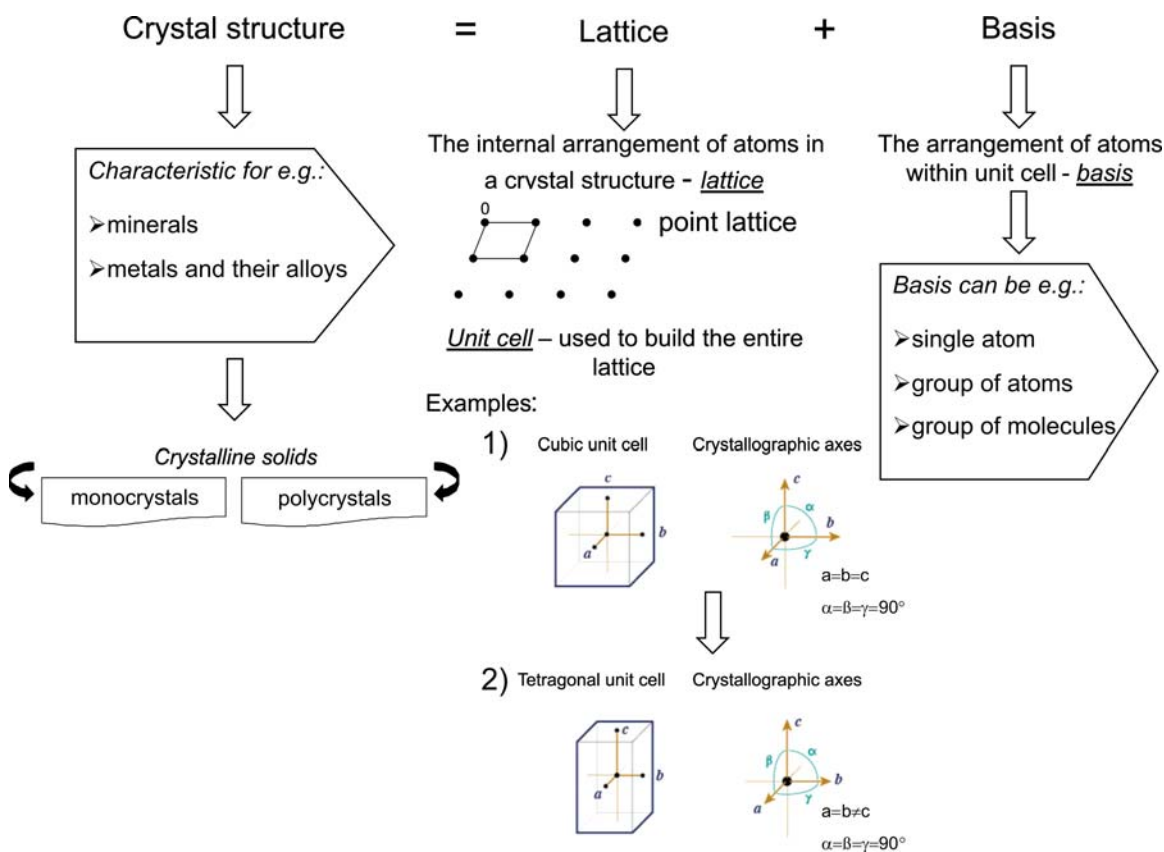**Figure 2.1.3.** "Schematic" definition of a crystalline structure [Kit05, Ste05].

A sketch summarizing some basics on the crystalline structure is presented in Figure 2.1.3. The ways how atoms and molecules are arranged within the unit cell and how unit cells repeat within a crystal are ruled by the inherent crystal symmetry [Ask03, Kit05, Ste05]. Under certain symmetry operations an atomic configuration of a given

crystal remains unchanged. In principal, there are three types of symmetry operations in crystallography. A symmetrical object can be transformed into itself via: rotational symmetry, mirror symmetry or translational symmetry. In addition to the above symmetry operations, the so-called compound symmetry which is a combination of translation and rotational/mirror symmetries can be distinguished. A full classification of a crystal is obtained when all of these inherent symmetries of the crystal are identified [Kit05, Ste05].

According to the morphologically derived seven crystallographic-axes systems, seven basic point lattices (*seven crystal systems*) can be constructed [Ste05]:

> ➢ triclinic,
>
> ➢ monoclinic,
>
> ➢ orthorhombic,
>
> ➢ tetragonal,
>
> ➢ trigonal (or rhombohedral),
>
> ➢ hexagonal,
>
> ➢ cubic.

However, when the crystal systems are combined with the so-called centering translation, which lead to additional lattice points in the interior of the primitive unit cells, the *Bravais lattices* can be considered. In 3-D space, there are 14 unique Bravais lattices, which are distinct from one another in the translational symmetry they contain. All crystalline materials recognized so far (excluding quasicrystals) fit in one of these arrangements [Kit05, Ste05]. Visual representations of *the seven crystal systems* together with the corresponding *Bravais lattices* are shown in Figure 2.1.4. Further on, according to the symmetry of a crystalline structure, all regular crystals can be classified as belonging to one of 230 crystallographic space-groups [Ste05].

It was expected that all the knowledge regarding crystal symmetry had been already gained…nothing more misleading. The sensational discovery of quasicrystals (QCs) exhibiting fivefold symmetry by Shechtman *et al.* (1984) began a new part in the history of crystallography [She84]. The formation of QCs was first observed in a rapidly quenched Al-Mn alloy [She84]. Until now, manifold binary, ternary and multi-component metallic systems with "icosahedral" symmetry were reported [Kös96, Sai03,

Küh05, Scu06a]. The revealed five-fold symmetry is fully precluded by the classical theory of crystal symmetry from occurring in perfect single crystals in which translational periodicity exists [Ell90].
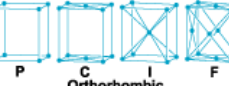
| Bravais lattice cells | Axes and interaxial angles | Examples |
|---|---|---|
| Cubic P  Cubic I  Cubic F | Three axes at right angles; all equal: $a = b = c; \alpha = \beta = \gamma = 90°$ | Copper (Cu), silver (Ag), sodium chloride (NaCl) |
| Tetragonal P  Tetragonal I | Three axes at right angles; two equal: $a = b \neq c; \alpha = \beta = \gamma = 90°$ | White tin (Sn), rutile ($TiO_2$), β-spodumene ($LiAlSi_2O_6$) |
| P  C  I  F Orthorhombic | Three axes at right angles; all unequal: $a \neq b \neq c; \alpha = \beta = \gamma = 90°$ | Gallium (Ga), perovskite ($CaTiO_3$) |
| Monoclinic P  Monoclinic C | Three axes, one pair not at right angles, of any lengths: $a \neq b \neq c; \alpha = \gamma = 90° \neq \beta$ | Gypsum ($CaSO_4 \cdot 2H_2O$) |
| Triclinic P | Three axes not at right angles, of any lengths: $a \neq b \neq c; \alpha \neq \beta \neq \gamma \neq 90°$ | Potassium chromate ($K_2CrO_7$) |
| Trigonal R (rhombohedral) | Rhombohedral: three axes equally inclined, not at right angles; all equal: $a = b = c; \alpha = \beta = \gamma \neq 90°$ | Calcite ($CaCO_3$), arsenic (As), bismuth (Bi) |
| Trigonal and hexagonal C (or P) | Hexagonal: three equal axes coplanar at 120°, fourth axis at right angles to these: $a_1 = a_2 = a_3 \neq c;$ $\alpha = \beta = 90°, \gamma = 120°$ | Zinc (Zn), cadmium (Cd), quartz ($SiO_2$) [P] |

**Figure 2.1.4.**   Fourteen 3-dimensional Bravais lattice types, classified by crystal system [Kit05, Ste05].

*The liquid-crystal transition*

The current section will be devoted to answering the question: *what are the essential requirements for the crystalline state formation*? However, owing to the problem complexity, only some selected issues concerning the mechanics of crystallization will be introduced.

Metallic materials present in our daily life are mainly fabricated by solidification techniques. As mentioned previously, the transition from liquid to solid can either proceed in a discontinuous mode (*crystallization*) or in a continuous mode (*glass transition*) [Tur61]. While metallic amorphous solids constitute a relatively new class of

alloys, the traditional crystalline metallic materials (e.g. steels, cast irons, bronzes) are known since centuries.

The process of the formation of solid crystals from a homogeneous solution or melt is called *crystallization* [Ask03]. It is essentially a solid–liquid separation, in which mass transfer of a solute from the liquid solution to a pure solid crystalline phase occurs. The particular stages of the liquid–solid (L–S) phase transformation are outlined in Figure 2.1.5.

In principle, the crystallization process consists of two major events, *nucleation* and *crystal growth*. By definition, nucleation refers to the formation of nanometer-sized clusters composed of solute atoms/molecules dispersed in the melt (solvent). From the thermodynamic and kinetic viewpoint, only clusters, which reach a critical size (with radii exceeding the radius $r*$ of the critical nucleus), are predicted to grow continuously [Rag75, Ask03]. Whether a given cluster (embryo) will become a nucleus or will redissolve, depends on the operating conditions (e.g. temperature, supersaturation). At this stage of crystallization, the arrangement of atoms in an ordered mode that defines the solid phase (see Figure 2.1.5) takes place.
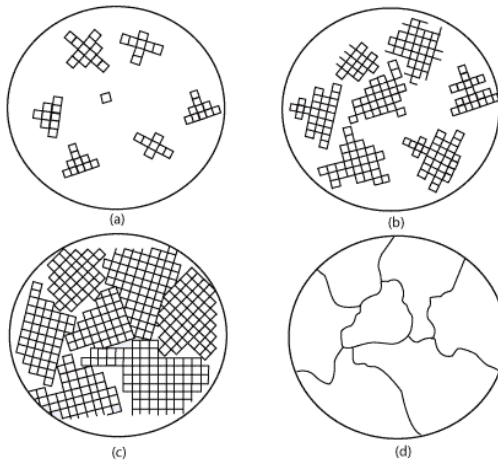


**Figure 2.1.5.**  Schematic illustration of the crystallization process: a) nucleation of crystals, b) crystal growth, c) irregular grains form as crystals grow together, d) grain boundaries as seen in a microscope [Ask03].

Basically, the process of nucleation can occur randomly (homogeneous nucleation) or non-randomly (heterogeneous nucleation) [Rag75, Ask03]. In the former case the probability of nucleation at any given site is identical to that at any other site within the assembly. The later case refers to a situation, in which the probability of crystal nucleation at certain preferred sites in the assembly is much larger than at other sites [Rag75]. For instance, the L–S transformation can have either random character or, as indicated in Figure 2.1.6, occurs at preferential sites, e.g. inclusions of solid foreign particles, walls of the container, catalysts. In the solid state, the nucleation process is usually heterogeneous (nucleation at grain boundaries, grain edges and corners, dislocations, etc.).
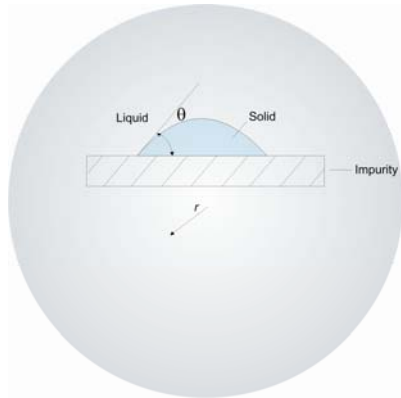


**Figure 2.1.6.** Heterogeneous nucleation in a liquid. The nucleus forms at impurities [Ask03].

Once the stable nucleus is formed, the second stage of crystallization, the so-called crystal growth begins. Due to the fact that the entire crystallization phenomenon is strongly governed by thermodynamic and kinetic factors, for a nucleus to grow and to form the equilibrium crystalline phase, the activation energy for atomic jumping across the interface is required. Thorough considerations on the thermodynamics and kinetics associated with the liquid–solid state phase transformation will be given in the next section. However, the problem will be described in terms of *the glassy state formation*. In other words, the main criteria for the suppression of the crystallization process upon cooling from the melt will be presented. The schematic illustration of the possible phase transitions occurring upon solidification: liquid→crystal and liquid→glass are exemplified in Figure 2.1.7 [Sco83]. The displayed time-temperature-transformation (TTT) diagram corresponds to the start and the finish of the above-mentioned transitions.

The glassy state can be achieved when the liquid is cooled at a rate suited to bypass the nucleation and growth of the α-crystalline phase (the cooling curve indicated as "line a" does not pass through the nose of the liquid→α-crystal transformation area and the end product of the solidification process becomes a glass). By subsequent heating of the glassy phase to the crystallization temperature $T_x$ with the defined heating rate $v$ the glass→crystal phase transition takes place [Kös80, Sco83].

Apart from the above-given approach, the crystallization of the amorphous state can also be achieved by conducting an isothermal heat treatment at a temperature $T < T_x$. The time to reach crystallization (indicated as $t_x$) strongly depends on the temperature and can vary from seconds to hours [Sco83].


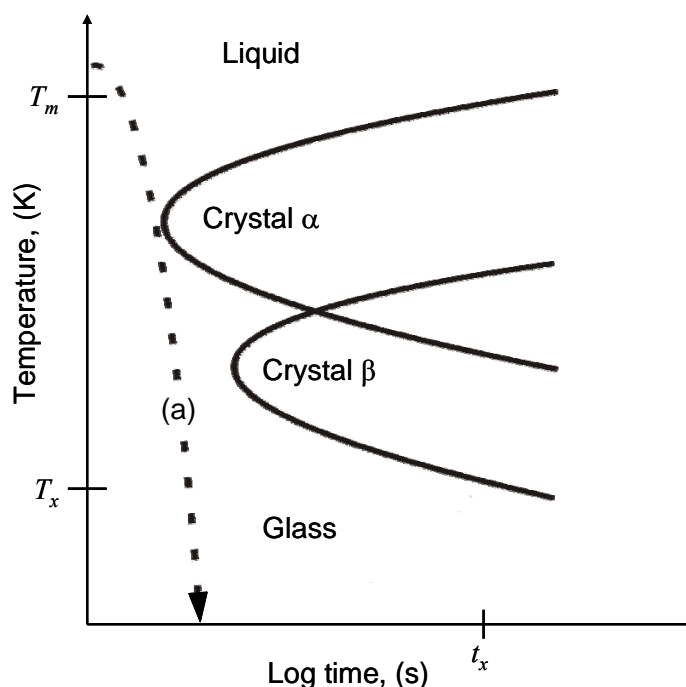
**Figure 2.1.7.** TTT diagram showing possible phase transitions occurring upon cooling: (a) rapid quenching resulting in a glassy state formation [Sco83].

Many compounds possess the ability to crystallize with various crystal structures. This phenomenon is called polymorphism. Each polymorph is in fact a different thermodynamic solid state and crystal polymorphs of the same compound manifest

different physical properties, such as dissolution rate, shape (angles between facets and facet growth rates), melting point, etc. For this reason, polymorphism is of principal importance in industrial manufacture of crystalline products [Ask03].

- Metallic glass – *nature of the glassy state and its formation*

From a variety of substances able to be cooled to the glassy state, metals and their compounds will be a subject of the following section. According to structural features of glasses [Tur69, Ell90] they can be considered as *amorphous solids characterized by a more or less well-defined chemical and topological short-range order (SRO) restricted to a few atomic distances* [Ell90, Ask03, Mir07].

In contrast to the already presented crystalline solids, which manifest a structural order persisting over at least tens or hundreds of atomic distances, the amorphous (literally, "*without form*") materials lack such a three-dimensional periodicity. To study the structures of glassy materials, X-ray, electron or neutron diffraction techniques are used. While long-range order gives rise to sharp Bragg peaks, a diffraction pattern for an amorphous solid consists of typical diffusive halos. Based on the structural information obtained from diffraction studies, a pair distribution function (PDF) can be determined [Ell90]. As schematically illustrated in Figure 2.1.8, PDF describes the probability of finding a second atom at a given distance $r$ from an average atom in the material.

Although, at a first glance, it can be appreciated that the structures of glassy materials are rather "uninteresting"- compared to the vast variety of periodic crystalline structures, the recent progress in characterization methods has revealed that such amorphous materials are much richer in their "structural appearance" than it was commonly thought. But an accurate, detailed description of the atomic configuration in glasses is not a trivial task and requires a comparison between the experimental PDF with those calculated from structural models proposed for metallic glasses – not discussed here [Sco62, Ega83, Mir04].
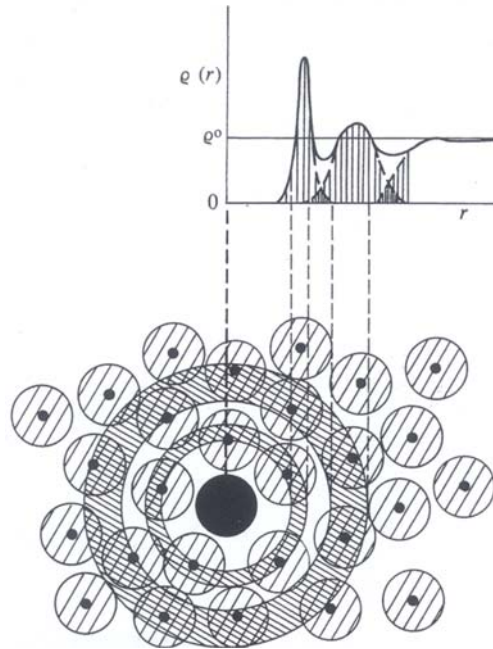
**Figure 2.1.8.**   Sketch illustrating an amorphous structure and the corresponding density distribution function $\rho(r)$ [Ell90].

In order to form and subsequently retain a glassy state certain conditions must be fulfilled. Considering thermodynamic and kinetic aspects, substances are more stable in the crystalline than in the amorphous state. Thus, to achieve a glass, a crystallization process has to be bypassed [Tur69, Bat07]. As exemplified in Figure 2.1.9, upon cooling of a liquid alloy, at a certain temperature $T_m$ (melting temperature) the melt undergoes a phase transition, which results in the formation of a crystalline solid. With progressing drop of temperature, a system will follow the solidus curve. However, according to the free volume theory [Tur61], when a cooling rate applied to a molten alloy is sufficiently high (highly undercooled liquid), the nucleation and/or growth of crystals can be avoided down to the so-called glass transition temperature $T_g$ and as a consequence, Gibbs free energy $G$ follows the liquidus curve. At $T_g$, the liquid alloy "freezes" to a rigid solid. The value of the free energy corresponding to such a "frozen" system is lower with respect to the liquid state, but greater when compared to the crystalline solid - stable equilibrium state. From the thermodynamic viewpoint, above $T_g$, a glass behaves as an undercooled liquid and is metastable.

To sum up the above considerations on the thermodynamic features of a glass, it can be concluded that *a glass is obtained when a cooled liquid solidifies without crystallization, which is coupled with the phenomena of the glass transition* [Ell90, Gre07].
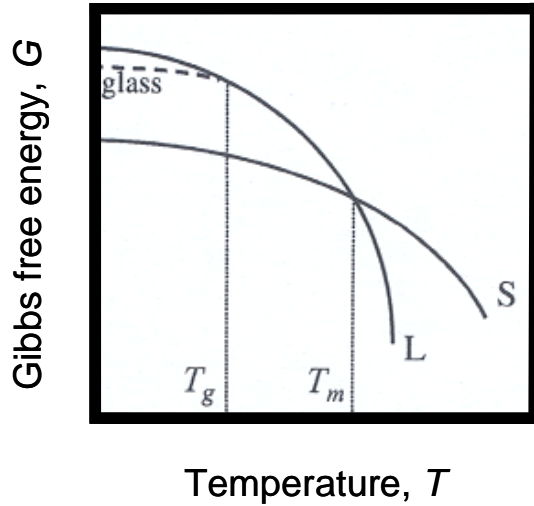


**Figure 2.1.9.** Schematic free energy $G$ diagram for a system as a function of the temperature $T$. L and S refer to liquidus and solidus curves.

However, the glass formation can also be achieved by a solid-state reaction (e.g. mechanical alloying of powder particles) without passing through the liquid state [Sch94, Fec95]. Such a crystal-to-glass transformation is observed under a number of different experimental requirements when a reached energy level is high enough and kinetic factors prevent the establishment of equilibrium. It has been demonstrated that in some cases the same glassy state can be achieved approaching it from the liquid or the solid state. Furthermore, in both instances, the stability of the undercooled liquid as well as of the non-equilibrium solid phase against glass formation is restricted by an isentropic condition [Fec95].

It should be remarked that all the alloys presented in the current thesis (see chapter 3 and chapter 4) were fabricated by the rapid solidification technique. Therefore, the underlying thermodynamic and kinetic principles concerning the glass transition phenomenon will be discussed in terms of the glassy alloys prepared by quenching from the melt.

"Knowledge of the equilibrium state under a given set of factors is the starting point in the description of any phenomenon or process [Pel05]".

It is well known that for equilibrium in a system of a given number of particles/atoms at a given temperature $T$ and pressure $p$, it is necessary that the Gibbs free energy $G$ is at its minimum [Sch81]. The Gibbs energy can be described by an expression of the form [Pel05]:

$$G = H - TS ,\qquad\qquad(2.2)$$

where $H$ = enthalpy, $S$ = entropy, and $T$ = temperature.

As mentioned before, a prerequisite for glass formation is the prevention of nucleation and crystal growth as a liquid is cooled below the melting point [Tur69, Owe85]. However, due to the fact that the Gibbs free energy $G$ of the undercooled melt is greater than that of the corresponding crystal [Cai08] – see Figure 2.1.9, there is a natural tendency of crystallization in the undercooled liquid. The difference in the Gibbs free energy $\Delta G$ between the supercooled liquid and the solid state provides the driving force for the nucleation process [Bus07], which proceeds through the formation of a small crystal from the melt that is capable of continued growth. Obviously, $\Delta G$ is a crucial factor influencing the creation of the crystal nucleus and nucleation rates as well as the crystal nucleus growth and growth rates.

From the thermodynamic point of view, the establishment of a solid/liquid interface is associated with a relatively large excess of energy. Hence, although the solid phase (S) is characterized by a lower $G$ than the liquid phase (L) below the melting point $T_m$, a nucleus is not necessarily stable [Ask03]. Consequently, the change in the free energy corresponding to the L–S phase transformation must include not only the change in $G$ between liquid and crystal but also $G$ of the solid/liquid interface. For each temperature below $T_m$, a crystal can be in equilibrium with a liquid when its radius of curvature has a certain value, which is known as the critical radius $r^*$. With increasing

undercooling $\Delta T$ the critical radius decreases. According to Hollomon and Turnbull [Hol53] nucleation occurs when the undercooling is such that there are sufficient nuclei with a radius greater than $r^*$.

$\Delta G$ of the formation of a spherical solid nucleus of radius $r$ within a liquid of a pure material is given by [Tur69, Bil96, Ask03]

$$\Delta G = -\Delta G_v + \Delta G_i = -\frac{4}{3}\pi r^3 \Delta g_v + 4\pi r^2 \gamma , \qquad (2.3)$$

where $\Delta G_v$ is the change in the Gibbs free energy on solidification associated with the volume and $\Delta G_i$ is the Gibbs free energy associated with the interface, $\gamma$ is the solid/liquid interfacial free energy and $\Delta g_v$ is the difference in Gibbs free energy per unit volume.

The variation of the Gibbs free energy of the embryo as a function of its radius and undercooling $\Delta T$ is shown in Figure 2.1.10.
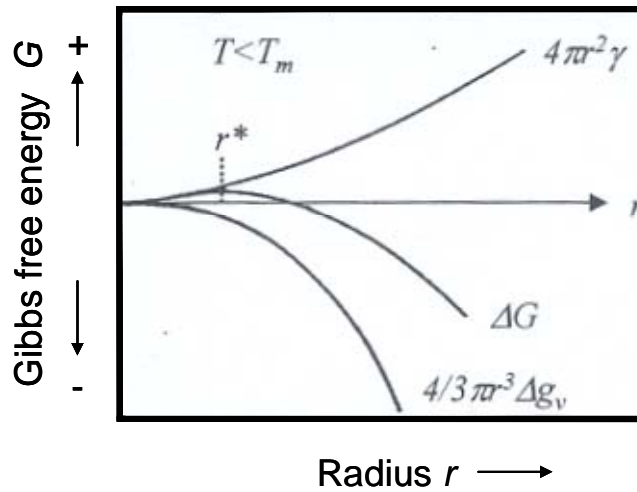


**Figure 2.1.10.**    Free energy change $\Delta G$ accompanying the formation of a spherical particle of a new phase as a function of radius, $r$.

Below the equilibrium temperature the sign of $\Delta G_v$ is negative because of the metastable nature of liquid. In contrast, $\Delta G_i$ is positive. For large values of $r$, the cubic dependence of $\Delta G_v$ dominates over $\Delta G_i$ and $\Delta G$ passes through a maximum at the critical

radius, $r^*$. When a thermal fluctuation causes an embryo[6] to become greater than $r^*$, growth will occur as a result of the descent of the total free energy [Bil96, Ask03].

The critical radius, $r^*$ is defined by the condition $\dfrac{d(\Delta G)}{dr} = 0$ which, gives

$$r^* = \frac{2\gamma(T)}{\Delta g_v(T)}.$$ 
(2.4)

For homogeneous nucleation, the critical energy of activation for an embryo of radius $r^*$ is equal to

$$\Delta G^* = \frac{16}{3}\pi\frac{\gamma^3}{(\Delta g_v)^2}.$$ 
(2.5)

In the case of heterogeneous nucleation, which occurs on energetically favorable catalytic surfaces, e.g. impurities, the formation of a stable, critical nucleus may appear at a much smaller undercooling. Compared to $\Delta G^*$ (Eq. 2.5) the thermodynamic barrier to heterogeneous nucleation $\Delta G^*_{het}$ is reduced by a factor $f(\theta)$, the so-called wetting function, to

$$\Delta G^*_{het} = \Delta G^* f(\theta),$$ 
(2.6)

where

$$f(\theta) = \frac{(2+\cos\theta)(1-\cos\theta)^2}{4}.$$ 
(2.7)

The contact angle $\theta$ between the nucleus and the substrate can alter from 180° (non-wetting) to 0° (perfect wetting) [Fec95]. When $\theta = 180°$, the solid does not interact

---

[6] The solid is an embryo, if its radius is less than the critical radius, and is a nucleus, if its radius is greater than the critical radius [Ask03].

with the substrate, $f(\theta) = 1$ and homogeneous nucleation appears. For $\theta = 0°$, the solid "wets" the substrate, $f(\theta) = 0$, and the value of the critical energy of activation is 0. As a consequence, the solidification process can begin instantly when the liquid cools to the freezing point [Bil96].

As it has already been mentioned, in order to obtain a glass, crystallization must be avoided…so *what requirements must be satisfied by the crystal nucleation rate and the cooling rate if crystallization should be impeded?* According to Turnbull, for melts free of heterogeneities [Tur69], the actual number $\delta n$ of crystal nuclei, which appear isothermally in a volume $v_l$, of the liquid phase in time $\delta t$, is described by the following relation:

$$\delta n = I v_1 \delta t,$$  (2.8)

where $I$ refers to the nucleation frequency/(volume×time). In instance of liquids characterized by a low viscosity the crystal grow rate is so large that the cooling rate will be restricted by the recalescence after a single nucleus has appeared. Under these conditions the nucleation process would have to be completely suppressed for crystallization to be prevented. It indicates that the value of $n$ would have to be less than 1 [Tur69], where

$$n = v_1 \int_0^t I dt$$  (2.9)

$t$ is the time in which cooling occurs, $I$ is a function of temperature, and the variation of $v_l$ with temperature is neglected. From the expression above, it can be seen, that the chances of forming a stable solid nucleus will be low for:

➢ small nucleation rates and,

➢ fast cooling rates.

Furthermore, from Eq. 2.10, it is apparent that the crystal nucleation rate is a product of the thermodynamic term, which depends on the probability of a fluctuation to

overcome the nucleation barrier, and a kinetic term, which depends on atomic diffusion (or viscosity) [Löf03]:

$$I = \frac{K}{\eta(T)} \exp\left[-\frac{\Delta G^*}{kT}\right],$$ (2.10)

where $\eta(T)$ is the viscosity of the undercooled liquid, the parameter $K$ is a proportionality constant, $k$ is the Boltzmann constant and $\Delta G^*$ is the activation energy – see Eq. 2.5. Considering now the formation of spherical nuclei, the homogeneous nucleation rate can be written as [Tur69]

$$I = \frac{K}{\eta(T)} \exp\left[-\frac{16}{3}\pi \frac{\alpha^3 \beta}{T_r(\Delta T_r)^2}\right],$$ (2.11)

where $T_r = \dfrac{T}{T_m}$ refers to the reduced temperature and $\Delta T_r = \dfrac{T_m - T}{T_m}$ accounts for the degree of undercooling. Comparing Eq. 2.11 with the previous one, the presence of the dimensionless parameters $\alpha$ and $\beta$ can be noticed. While the first one corresponds to the solid/liquid interfacial energy $\gamma$ the second is related to the entropy of fusion $\Delta S_m$. The values of log $I$ as a function of the reduced temperature $T_r$ calculated from various assignments of $\alpha\beta^{1/3}$ are plotted in Figure 2.1.11. To obtain an upper bound for $I$, $\eta$ was set equal to $10^{-2}$ poise (a common value for liquid metals), independent of $T$. $K$ was taken equal to $10^{23}$ Nm [Tur69]. At small undercooling ($T_r \sim 1$), $I$ is negligible. An increase of $\Delta T_r$ results in an increase of the crystal nucleation rate. Thereby, $I$ passes through a broad maximum at around $T_r = 0.3$, which does not depend on the $\alpha\beta^{1/3}$ value, and falls to zero at 0 K. The liquid substances for which $\alpha\beta^{1/3}$ can achieve values greater than 0.9, would practically not exhibit homogeneous nucleation at any cooling rate. In strong contrast, for fluids with small $\alpha\beta^{1/3}$ cooled even with the fastest obtainable rates, it should be practically impossible to avoid crystallization.

**Figure 2.1.11.** Variation of the logarithm of the rate (in $cm^{-3}s^{-1}$) of homogeneous nucleation of crystals $I$ in an undercooled liquid as a function of the reduced temperature $T_r$ for various values of $\alpha\beta^{1/3}$ [Tur69].

Considering the effect of the viscosity $\eta$ on the crystal nucleation rate $I$ - Figure 2.1.12 shows the variation of log $I$ with reduced temperature $T_r$. $\alpha\beta^{1/3}$ was set equal to 0.5. Since the value of $\alpha\beta^{1/3}$ is fixed, the viscosity becomes a dominant factor governing $I$. The liquid shear viscosity $\eta$ is approximated by:

$$\eta = 10^{-3.3} \exp\left[\frac{3.34}{T_r - T_{rg}}\right],\tag{2.12}$$

where $T_{rg} = \dfrac{T_g}{T_m}$ is the reduced glass transition temperature.



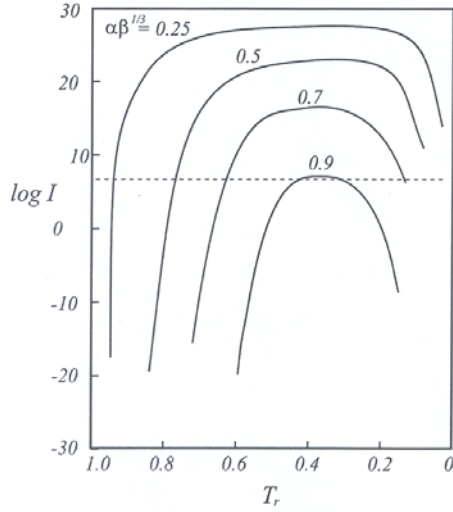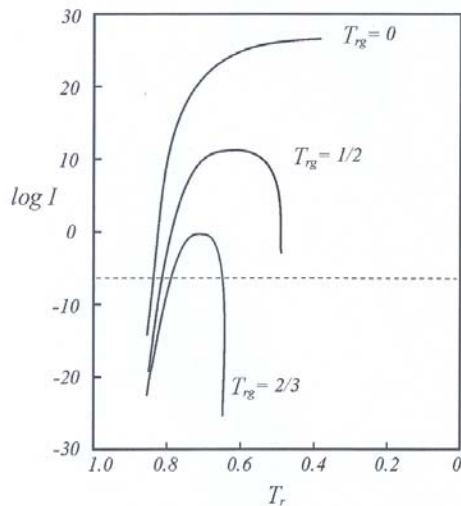**Figure 2.1.12.** Variation of the logarithm of the rate (in $cm^{-3}s^{-1}$) of homogeneous nucleation of crystals $I$ calculated from Eq. 2.11 as a function of the reduced temperature $T_r$. The calculations were performed for $\alpha\beta^{1/3}$ set to 1/2. The values of viscosity $\eta$ were obtained from the Fulcher equation [Tur69].

24

As explained by Turnbull *et al.* the glass-forming tendency of the undercooled liquid should increase with $T_{rg}$. A closer look at Figure 2.1.12 reveals that, with increasing reduced glass transition temperature, the peak in the $I$-$T_r$ relation becomes lower, sharper and is shifted towards higher values of $T_r$. When $T_{rg} = 2/3$, liquids would only crystallize within a narrow range of temperature and then just slowly. Thus, such substances can be considered as good glass-formers. Contrary, in the case of liquids with $T_{rg} = 1/2$, the homogeneous nucleation would only be suppressed if they are rapidly quenched in relatively small volumes. Finally, the value of $T_{rg}$ required to achieve the glassy state at a given cooling rate will be lower the higher is $\alpha\beta^{1/3}$ [Tur69].

### *Glass-forming ability*

In order to analyze and predict the glass-forming ability (GFA) of metallic alloy systems, several methods were invented up to date. In principal, GFA can be expressed in terms of the critical cooling rate $R_c$, which is necessary to turn a melt into a glass. The critical cooling rate $R_c$ is defined as the minimum rate at which an alloy must be quenched from its liquid state to achieve the amorphous structure. While the early glassy alloys reported required extremely high cooling rates for glass formation ($R_c > 10^5$ Ks$^{-1}$) [Cah93, Ino00], the recently developed alloys are characterized by much lower critical cooling rates [Ino97, Zha99, Ino00]. In comparison with the foregoing generation of metallic glasses (thicknesses restricted to less than $\approx 50$ μm) "modern" bulk glassy alloys can be cast into rods with diameters in the 1 - 2.5 cm range [Gre07] – see Figure 2.1.13.
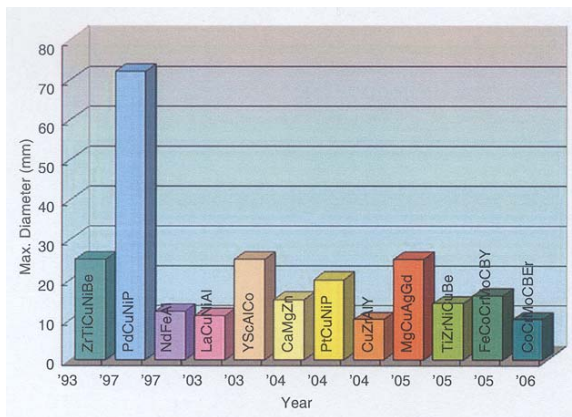


**Figure 2.1.13.** Maximum rod diameter obtained for bulk metallic glasses developed in various alloy systems. In addition, the year of their discovery is given [Gre07].

The critical cooling rate can be linked to the reduced glass transition temperature

$T_{rg} = \dfrac{T_g}{T_m}$ where $T_m$ refers to the liquidus temperature $T_{liq}$, and to the interval of a

supercooled liquid defined by the difference between the glass transition temperature $T_g$

and the crystallization temperature $T_x$, $\Delta T_x = T_x - T_g$ [Ino00]. The values of $T_{rg}$ and $\Delta T_x$

can be evaluated from the DSC curves. The correlation between the critical cooling rate

($R_c$), the maximum sample thickness for glass formation ($t_{max}$) and the reduced glass

transition temperature ($T_{rg}$) has been exemplified in Figure 2.1.14 [Ino00].
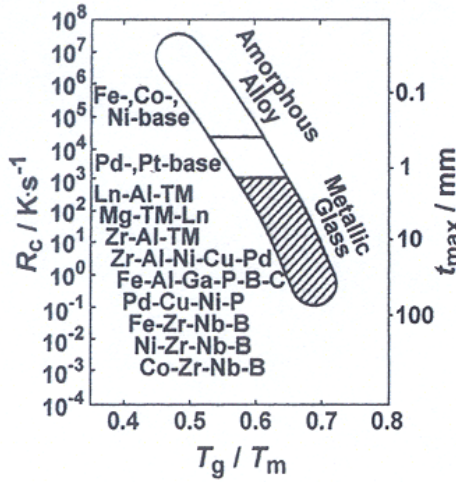


**Figure 2.1.14.**

Correlation between $R_c$, $t_{max}$ and $T_{rg}$ for bulk amorphous alloys. Additionally, the data of the common glassy alloys, which require high cooling rates for amorphous phase formation, are displayed [Ino00].
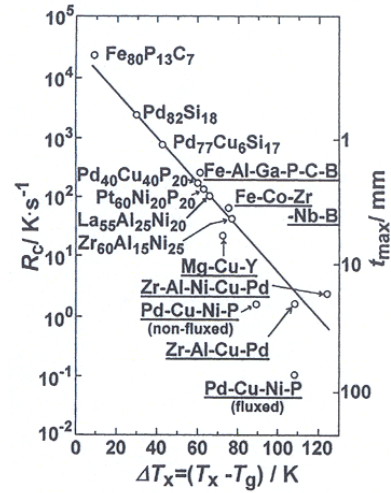
**Figure 2.1.15.**

Correlation between $R_c$, $t_{max}$ and $\Delta T_x$ for bulk metallic glasses [Ino00].

Among the bulk metallic glasses discovered so far, the $Pd_{40}Cu_{30}Ni_{10}P_{20}$ glassy

alloy exhibits the lowest critical cooling rate ($R_c \approx 0.10$ Ks$^{-1}$). The corresponding $t_{max}$

reaches values as large as 100 mm [Ino97]. Figure 2.1.15 illustrates the variations in $R_c$

and $t_{max}$, when the parameter $\Delta T_x$ is taken into account. Up to date, the highest value of the undercooled liquid region exceeding 100 K was reported for a number of MGs in the Zr-Al-Ni-Cu and Pd-Cu-Ni-P alloy systems [Ino00]. The greater is $\Delta T_x$ the better thermal stability is demonstrated by the glassy state.

As mentioned in the previous chapter the materials used in this study were derived from the Fe-(Cr-Mo-Ga)-(P,C,B) glass-forming composition. Such an alloy system is known for its rather high glass-forming tendency. The critical cooling rate $R_c$ required to turn the molten Fe-(Cr-Mo-Ga)-(P,C,B) alloy into a glass is of the order of $10^2$ - $10^3$ Ks$^{-1}$. The measured values of the reduced glass transition temperature $T_{rg}$ and the supercooled liquid region $\Delta T_x$ are about 0.6 and 60 K, respectively. These characteristics enable to fabricate an amorphous alloy in bulk form. However, compared to good glass-formers such as Zr- and Pd-based alloys, the maximum obtainable thickness is confined to a few millimeters [She99, Sto02, Han07].

Based on the above-presented data, the following conclusions can be drawn:

➢ $R_c$ decreases with an increase of $T_{rg}$ and $\Delta T_x$ and, hence

➢ a large GFA can be attributed to large values of $T_{rg}$ and $\Delta T_x$.

The next extremely important factor contributing to the glass-forming ability of a material is its chemical composition. Inoue *et al.* [Ino93b, Ino00] explained that in order to optimize the GFA of a given alloy three empirical rules should be satisfied:

➢ the selected system must consist of more than three elements,

➢ a significant difference in atomic size ratios above 12 % among the three dominant constituents is required,

➢ heats of mixing among the three main constituent elements should be negative.

In other words, for achieving a high GFA, a *multi-component alloy system with optimum packing and bonding state* must be chosen.

Summarizing the above considerations on the parameters affecting the glass-forming tendency, it can be argued that the homogeneous nucleation rate of a crystalline phase drops with an increase of the interfacial energy between liquid/solid phases and with the viscosity $\eta$ (to be discussed next). Likewise, the growth rate is also dominated by the viscosity. Furthermore, the large values of $T_{rg}$ and $\Delta T_x$ suggest that $\eta$ increases steeply with decreasing temperature and an increase in the packing friction. By increasing

the number of constituent elements with different atomic sizes as well as large negative heats of mixing, more efficient atomic packing and bonding states are achieved. This, in turn, leads to an increase of the difficulty of redistributing the constituents over a long-range scale (barrier for the crystallization). As a consequence, a significant improvement of the GFA is noticed [Ino93b, Li07].

*On the glass transition*

The occurrence of the glass transition is the distinctive feature of glassy solids fabricated via freezing of the liquid phase [Bat07]. A glass transition takes place at the so-called glass transition temperature $T_g$. However, $T_g$ is not an accurately defined temperature but corresponds to the range of temperatures over which such a transition occurs. The value of $T_g$ depends on the cooling rate and subsequently on the thermal history of the alloy [Owe85]. Besides the position of $T_g$, the width of the transformation region also depends on the applied cooling rate. It has been noticed that lowering the rate of cooling sharpens the glass transition [Jäc86]. A glass transition phenomenon is manifested by a change in first order extensive thermodynamic variables, such as volume ($V$), enthalpy ($H$) or entropy ($S$) during heating or cooling [Owe85, Fec95]. Consequently, second order thermodynamic properties like specific heat capacity ($C_p$) and thermal expansivity ($\alpha$) exhibit marked discontinuities at the glass transition.

Figure 2.1.16 illustrates the temperature dependence of the enthalpy and heat capacity of the liquid at constant pressure [Deb01]. Upon cooling of a glass-forming alloy system, the enthalpy does not manifest a discontinuity at $T_m$, as it would occur in the case of crystallization. Instead, a continuous linear *H-T* relationship is observed. However, as $T_g$ is reached and the system departs from the equilibrium state, the temperature dependence of the enthalpy decreases discontinuously. As a consequence, the heat capacity $C_p = \dfrac{\partial H}{\partial T}$ decreases abruptly [Deb01] with a pronounced maximum at $T_g$, reflecting the fewer degrees of freedom resulting from the freezing of the structure [Dav83]. At temperatures below $T_g$, the slope of *H* for the glassy phase is similar as that for the crystal. It implies that the heat capacity of the glass has typical solid-like values.

Considering the temperature dependence of the entropy of a liquid, it has been attempted to define an "ideal glass transition" by extrapolation to infinitely slow cooling. It has been speculated that this ideal glass transition can be considered to be a thermodynamic phase transformation [And79]. Such a speculation was stimulated by two experimental findings. According to Kauzmann [Kau48], for alloy systems with a good GFA the excess entropy $\Delta S$ of the supercooled liquid in metastable equilibrium relative to the same crystalline material extrapolates to zero at the so-called Kauzmann temperature $T_K$. Surprisingly, $T_K$ ($\Delta S = S_{liquid} - S_{solid} = 0$) is close to the glass transition temperature [Jäc86]. Since it seems paradoxical that the entropy of the supercooled liquid should have a lower value than that of the crystal below the Kauzmann temperature, an occurrence of the glass-like transition may be expected around $T_K$ [Jäc86].
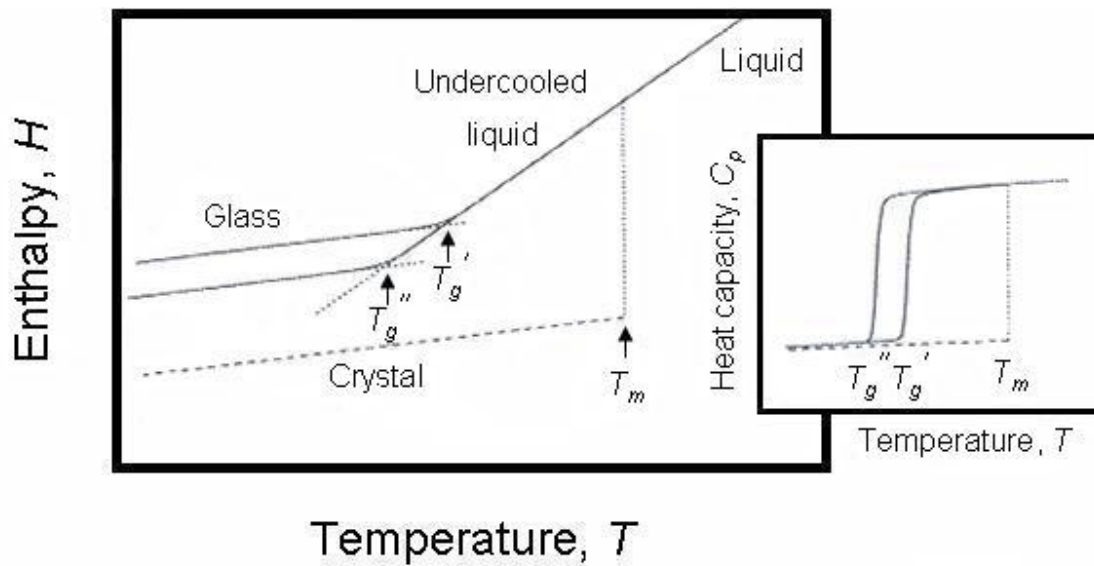


**Figure 2.1.16.**    Temperature dependence of the enthalpy $H$ of a liquid; $p$ = constant. A fast cooling rate produces a glass transition at $T_g'$, while a slower cooling rate results in a glass transition at $T_g''$. The inset of the figure displays the $C_p$-$T$ relationship.

The other approach to detect the glass transition is based on the free-volume model for viscous flow [Coh59, Tur61, Tur70]. In the framework of this model the glassy

structure has been proposed as approximating to an assemblage of dense-packed hard spheres. The volume in which each sphere can move and oscillate without an energy change is defined as the free volume $v_f$. According to the model, the atomic diffusion proceeds through the jumps of the atoms into voids, which exceed a critical value $v^*$ and which result from the redistribution of the free volume $v_f$. Obviously, the smaller $v_f$, the more sluggish is any structural rearrangement. Hence, the occurrence of the glass transition phenomenon upon cooling can be attributed to the decrease of the free volume below the critical value and to the consequent drop of the atomic mobility to a level where the liquid-like configurational changes are no more allowed. At temperatures below $T_g$, free volume is frozen-in. Consequently, if the applied cooling rate is high, the resulting glassy phase has a lower density compared to a more slowly quenched one. In other words, this glassy phase is characterized by a greater free volume.

Finally, the principles of the glass transition can be represented by the temperature dependence of the viscosity $\eta$ of the glass former. The viscosity values for typical liquids (e.g. water, alcohol) at room temperature are of the order of $10^{-2}$ Pa·s [Tur69, Bus07]. Upon cooling, a rapid discontinuous increase of $\eta$ is observed at $T_m$ if the liquid phase crystallizes. In contrast, the viscosities of glass-forming substances increase slowly and continuously with falling temperature close to $T_m$, reflecting an increase of the resistance of the undercooled liquid to flow [Del04]. The equilibrium viscosity data measured in a supercooled regime can be described well by the Vogel-Fulcher-Tammann (VFT) formula [Vog22, Ful25, Tam26]

$$\eta = \eta_0 \cdot \exp\left[\frac{B}{T - T_0}\right],$$
(2.13)

where $\eta_0$ and $B$ are temperature-independent constants and $T_0$ is the VFT temperature. When the value of $T_0$ is equal to 0 the above equation assumes the Arrhenius form [Tur69, Deb01]. The transition from the liquid state to the rigid glass occurs within a quite narrow temperature interval above $T_0$. The approach of the glass transition is manifested by a dramatic increase of the viscosity [Jäc86]. In general, the glass-transition

temperature $T_g$ is defined as the temperature at which the value of $\eta$ reaches $10^{12}$ Pa·s [Deb01, Bat07].

As shown in Figure 2.1.17 glasses can be either strong (high GFA) or fragile (low GFA). Such a classification has been proposed for the first time by Angell [Ang91]. According to Angell the VFT relation can be reformulated to:

$$\eta = \eta_0 \cdot \exp\left[\frac{D^* T_0}{T - T_0}\right],$$ (2.14)

where the parameter $D^* = \dfrac{B}{T_0}$ is a measure of the kinetic fragility of the liquid [Bus07].

The viscosity of the "strong" glass-forming substances behaves in a nearly Arrhenius fashion, while the "fragile" liquids exhibit distinct deviations from an Arrhenius-like behavior. For the most fragile substances, the value of $D^*$ is on the order of 2. In contrast, for the strongest glass formers, $D^*$ reaches 100 (e.g. $SiO_2$ and $GeO_2$) [Bus07, Del04].



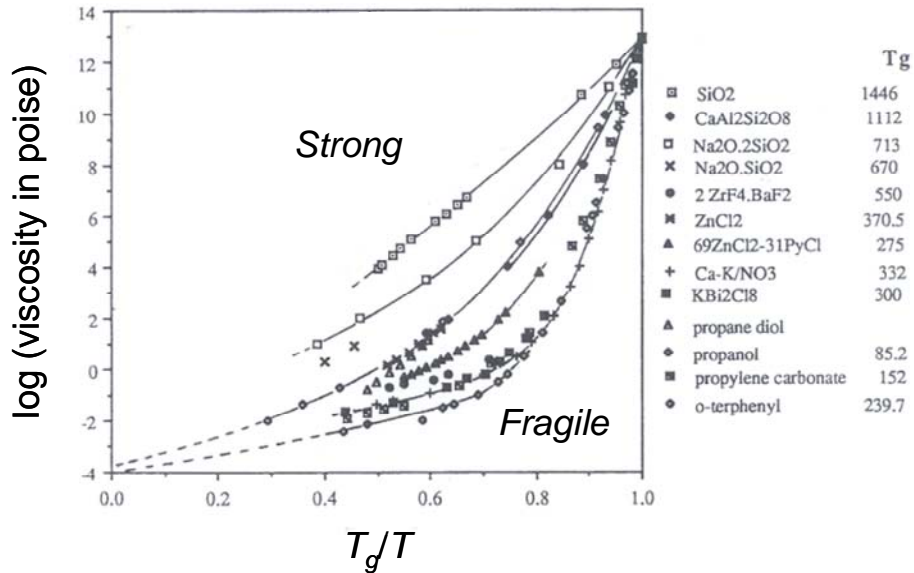| | | Tg |
|---|---|---|
| ⊞ | SiO2 | 1446 |
| ◆ | CaAl2Si2O8 | 1112 |
| ▫ | Na2O.2SiO2 | 713 |
| ✕ | Na2O.SiO2 | 670 |
| ● | 2 ZrF4.BaF2 | 550 |
| ✖ | ZnCl2 | 370.5 |
| ▲ | 69ZnCl2-31PyCl | 275 |
| + | Ca-K/NO3 | 332 |
| ■ | KBi2Cl8 | 300 |
| ▲ | propane diol | |
| ◆ | propanol | 85.2 |
| ■ | propylene carbonate | 152 |
| ◉ | o-terphenyl | 239.7 |

**Figure 2.1.17.**   Angell plot comparing the $\eta$-$T$ relationship for different types of glass-forming liquids. A linear Arrhenius-like behavior is observed for strong glasses [Ang91].

- Metallic glass matrix composites

As already mentioned in "**Introduction**", although the mechanical strength of bulk glassy alloys is very high, the corresponding macroscopic plasticity is strongly limited [Eck07b, Li07]. In order to enhance the plastic strain of BMGs, the concept of fabricating glass matrix composites has recently been developed [Hay00, He03a, Cal03, Lee05, Eck07a, Eck07b]. It has been found that the dispersion of a second-phase with a different length scale in a metallic glass matrix is beneficial to improve the strength-plasticity balance. Therefore, apart from the search for new monolithic amorphous materials, the production of complex bulk glassy alloys is of great interest [Li07].

In principle, BMG composite microstructures can be obtained by:

➢ mechanical alloying (MA) and consolidation [Eck97],

➢ solidification [Ino93a, Pek93], or

➢ partial devitrification of the glassy phase by either annealing [Sai99, Xin99] or severe plastic deformation/high pressure torsion [Bou05, Wil06].

Moreover, according to the processing history, BMG composites can be classified in two groups: *ex-situ* and *in-situ* formed composites [Eck07b] – see Figure 2.1.18.
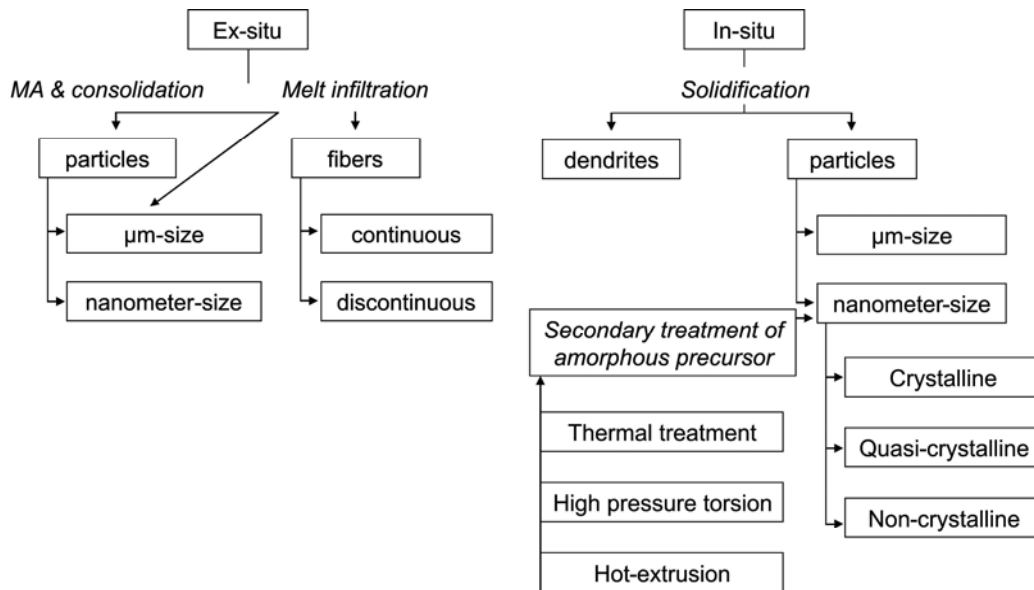


**Figure 2.1.18.**   Various processing routes and evolution of bulk BMG composites with different length scales of the second phase dispersion [Eck07b].

Due to the fact that the Fe-based complex alloys developed by the author (and co-workers) were directly obtained from their melts upon solidification processing, the present section will be mainly focused on the *in-situ* formed composites. In this approach, the original composition of the metallic glass is modified toward the composition of the primary precipitating (ductile) phase. Upon cooling, this ductile reinforced phase crystallizes first and shifts the composition of the remaining liquid toward the parent glass so that this liquid solidifies as a BMG matrix [Li07]. The resulting microstructure is composed of either micro- or nanometer-sized crystalline, quasi-crystalline (QC) or non-crystalline phases embedded in an amorphous matrix. Furthermore, the fabrication of the *in-situ* composites strongly depends on the chosen chemical composition as well as the cooling rate realized upon solidification [Ino96, Küh00, He03b]. The schematic illustration of the achievable microstructures of *in-situ* composite materials is presented in Figure 2.1.19.
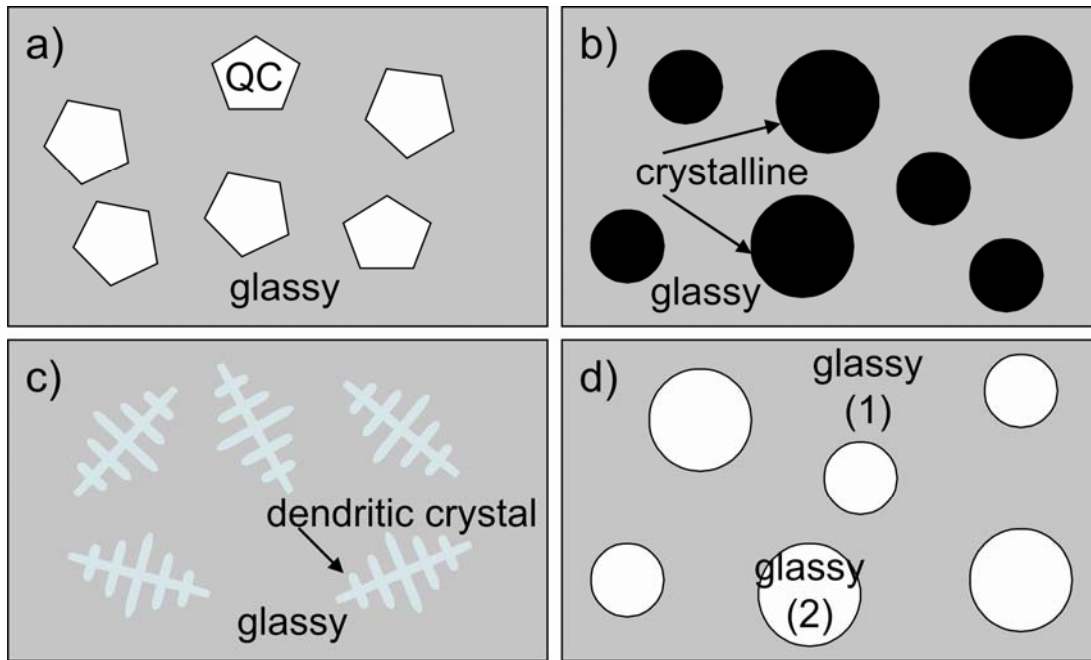


**Figure 2.1.19.**     Schematic illustration of microstructures of *in-situ* composites with different shape, size, and morphology of the second-phase dispersions: a) quasi-crystalline phase (QC), b) spherical nanometer-sized crystals, c) dendrites, and d) two glassy phases [Eck07b].

Quasicrystalline-*BMG composites*

Micro- and nanometer-sized quasicrystalline (QC)-reinforced bulk metallic glass composites have been synthesized in Zr- [Küh00] and Ti-based [Guo05] alloy systems in bulk form. By increasing the cooling rate, the formation of fully glassy specimens can be achieved for the above glass-forming alloys [Küh00, Guo05]. The detailed studies on the QC phase have revealed a strong effect of the oxygen dissolved in the molten alloy on the stability of the icosahedral arrangement [Eck98, Geb98]. Moreover, it has been proven that the presence of nano-QC dispersions in a glassy matrix [Eck98, Geb98] is beneficial for the enhancement of the room-temperature plastic strain. Indeed, the obtained mechanical characteristics for the selected Zr- and Ti-based BMG composites are significantly improved compared to their monolithic counterparts.

*Crystalline-BMG composites*

A great impact on the development of the crystalline particle-reinforced BMG composites had a work of Hays *et al.* [Hay00], who reported the fabrication of an as-cast composite structure consisting of ductile b.c.c. β-Zr(Ti) dendrites in a glassy matrix. The resulting two-phase microstructure has been achieved by tuning the Vit-1 composition of the Zr-Ti-Nb-Cu-Ni-Be alloy. The carried out RT compression tests revealed that such a composite is able to sustain up to 5-6% plastic deformation [Hay00]. A similar microstructure has also been observed by Kühn *et al.* [Küh02] and Eckert *et al.* [Eck02] for multicomponent Zr-Nb-Cu-Ni-Al glasses. In this case, b.c.c. β-Zr(Nb) dendrites were found to be a reinforcing phase.

Up to date, a variety of *in-situ* BMG-matrix composites were successfully synthesized. Apart from Zr-based glassy alloys, the composite structure formation has also been achieved for a $Ti_{50}Cu_{23}Ni_{20}Sn_7$ alloy [He03b]: glassy matrix (GM) + hexagonal close-packed (h.c.p.) α-Ti phase, a $(Cu_{0.6}Zr_{0.25}Ti_{0.15})_{93}Nb_7$ alloy [Bia04]: glassy matrix (GM) + Nb-enriched dendrites or $(Cu_{0.50}Hf_{0.35}Ti_{0.10}Ag_{0.05})_{100-x}Ta_x$ ($0 \le x \le 12$ at.%) BMG [Bia05] containing Ta-rich dendrites distributed in a glassy matrix. In all these cases, the morphology of the precipitated phase is dendritic [Eck07a, Eck07b]. Taking advantage of

the hints provided by Hays *et al.*, novel complex nanostructures have recently been prepared in Ti- [He03a] and Zr-based [Das03a, Das03b, Scu06b] alloys. Such materials are characterized by a bimodal grain size distribution and are composed of b.c.c. Ti(Ta/Nb,Sn) [He03a], Zr(Nb) [Das03a, Das03b] or $\alpha$-h.c.p. Zr(Ni) [Scu06b] dendrites dispersed in a nanostructured matrix phase.

Recently, new massive nano/(ultrafine)-grained materials have been fabricated by the sequential combination of different non-equilibrium processing pathways [Wil06, Wil07]. For instance, the homogenous $Al_{88}Y_7Fe_5$ nanostructured bulk alloy can be obtained through the combination of severe plastic deformation and initial vitrification based on rapid melt quenching [Wil06]. Such nanometer- (or ultrafine) scale materials manifest a superb mechanical strength. The achievable values of strength to failure are remarkably improved compared to conventional coarse-grained alloys [Per98, Din05, Wil05]. Recently Park *et al.* [Par08] showed that the creation of nano/ultrafine eutectic Fe-Nb-(Al) composites containing constituents with various length scales can bestow a simultaneous improvement of strength and ductility through controlling the plastic and failure instabilities upon the deformation process. The presence of a micron-sized primary dendritic phase ($\alpha$-Fe or $Fe_2Nb$) in an ultrafine-scale eutectic matrix leads to a material with excellent fracture strength ($\sigma_f = 1.4 - 1.8$ GPa) combined with a reasonably good plasticity ($\varepsilon_f = 6.5 - 13\%$) [Par08]. The above-presented approach to produce complex materials with a well-optimized property combination might be an alternative for the monolithic Fe-based glassy alloys. Although such materials manifest an extremely high strength, the corresponding ductility is disappointingly low.

According to Figure 2.1.19, the shape of the precipitated phase can either be dendritic (already discussed examples) or spherical. For instance, the formation of such amorphous matrix composites reinforced with round-shaped particles has been reported for $(Zr_{0.7}Ni_{0.1}Cu_{0.2})_{82}Al_{10}Ta_8$ [Fan02] and $(Cu_{0.6}Zr_{0.3}Ti_{0.1})_{95}Ta_5$ [Lee05] alloys by adding a proper amount of Ta to the glass-forming alloy composition. Upon solidification, the matrix undergoes a glass transition to produce a glassy phase, whereas the micron-sized particles of a precipitated Ta(Zr/Ti)-rich [Fan02, Lee05] solid solution are distributed in the glass matrix. The resulting complex materials not only exhibit high strength, but also

have dramatically enhanced plastic strain to failure in uniaxial compression relative to single-phase BMGs.

Summarizing, the preparation of the above-presented *in-situ* composite microstructures demands a proper selection of the alloy composition, a correctly adjusted cooling rate and/or controlled heat treatment in order to control the size, the morphology and the volume fraction of the second phase dispersions [Eck07a, Eck07b].

## 2.2 Structure – mechanical behavior relationships

- Comparison of conventional crystalline materials with metallic glasses

Generally, the mechanical response of materials can be described largely in terms of the materials properties that govern plastic deformation and fracture [Mug93]. Considering reversibility and time-dependence, the mechanical behavior of a material can be categorized into the following groups: *the elastic response* – instantaneous and reversible, *the anelastic response* – reversible and time-dependent and ultimately *the plastic response*, which is irreversible and time-dependent [Spa83].

It is known that the plastic response occurs by shear. The *theoretical shear stress* $\tau_{th}$ ($\tau_{th} \approx \dfrac{G}{2\pi}$, where $G$ is the shear modulus) is defined as the upper limit of the shear resistance of a given material and refers to the shear deformation of a perfect crystal. However, the "real" defect-containing crystalline materials yield plastically at considerably lower shear yield stresses $\tau_y$ (or tensile yield stresses $\sigma_y$). The observed discrepancy between the theoretical shear stress and the experimentally determined one results from dislocation glide, which takes place upon loading [Mug93]. Due to the various possible strengthening mechanisms existing in conventional crystalline materials e.g. strain hardening, solid-solution strengthening, the yield strength or the flow stress of ductile materials can be greatly improved.

In contrast to crystalline metallic alloys, glassy materials are dislocation-free. The absence of lattice dislocations and slip systems leads to a high elastic deformation of more than 2% prior to yielding (while for the crystalline alloys $\varepsilon_y = 0.2\%$). The

remarkably high ratio of $\dfrac{\sigma_y^2}{E}$ and the good values of the index $\dfrac{\sigma_y^2}{\rho E}$ (where $\sigma_y$, $\rho$ and $E$ are yield strength, mass density and Young's modulus, respectively) enable MGs to occupy a unique position in the Ashby's plot of strength ($\sigma_y$) versus elasticity ($E$) as illustrated in Figure 2.2.1 [Ash06, Gre07].
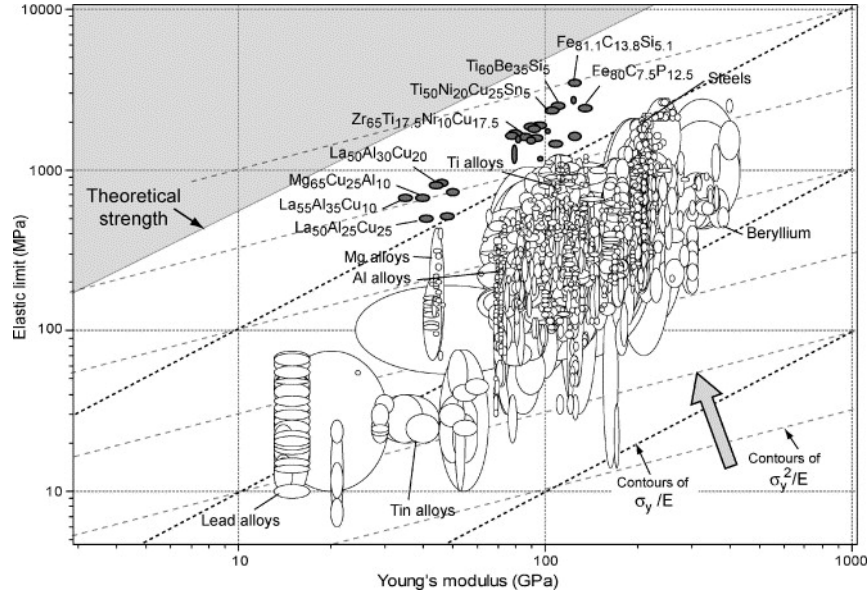


**Figure 2.2.1.** Elastic limit (strength, $\sigma_y$) and Young's modulus ($E$) for metallic glasses compared with conventional metals, alloys and metal-matrix composites [Ash06].

The above-mentioned mechanical features are superior compared to any other engineering material exposed on the Ashby's diagram. The extensive studies of the mechanical behavior of glassy alloys reveal their excellent RT compressive fracture strengths ($\sigma_f$), approaching the theoretical values. For instance, the $\sigma_f$ reported for the Co- [Ino03a, Fan09], Fe- [Ino04a, She05, Cha09], Ni- [Qia08], Zr- [Tar09] and Cu-based [Lee06, Dua08] glass-forming systems are: ~ 5 GPa, ~ 4 GPa, ~ 3 GPa and ~ 2 GPa, respectively. Moreover, the hardness and the strength of bulk glass formers are correlated [Ino01, Ino02] with Young's modulus and other characteristic features of BMGs

[Che75]. For example, for the hardest alloys, an increase of $T_g$ from 700 K to more than 900 K causes an impressive increase of $\sigma_f$ from less than 2 GPa to more than 5 GPa.

On the other hand, the lack of crystallinity and the associated lack of microstructural features such as grain and phase boundaries, lattice dislocations (no hardening mechanisms present) result in a very low macroscopic plasticity of the monolithic glassy alloys [Eck07b, Yav07]. While crystal dislocations enable changes in the atomic neighborhood at low energies or stresses, the local rearrangement of atoms in metallic glasses requires relatively high energies or high stresses involved [Sch07]. In general, MGs tend to suffer from work-softening and extreme localization of plastic flow into narrow shear bands (minimum thickness ∼ 10 nm). In most cases, unconstrained deformation modes such as tension or compression typically produce a catastrophic failure once the yield stress is achieved (plastic strain ∼ 1%) [Yav07]. However, while the vast majority of BMGs fail in a brittle manner, some surprisingly sustain a large plastic deformation in compression or bending. So far, such a phenomenon has been observed for Pt- [Sch04], Cu- [Das05, Ino05, Das06], Pd- [Yao06], Ti- [Men05] and Zr-based [Haj07] glass formers. The excellent plastic strain as reported for those alloy systems (in some instances exceeding 50%) arises from a multiple shear band formation. Therefore, the guiding principle in improving the plasticity of MGs is to facilitate the formation of multiple shear bands so that the strain is not concentrated in one or few shear bands that can wreak havoc, not least by evolving into cracks [Gre07]. It is obvious that the thorough understanding of shear band emission and operation is of great importance in further advancing our knowledge regarding the deformation mechanisms in amorphous solids [Eck07b, Li07, Yav07].

In order to describe the mechanism of plastic flow of glassy alloys, several concepts have been proposed up to date. According to the pioneering work of Spaepen [Spa77], the viscosity of shear bands drops upon deformation due to the generation of excess free volume or flow defects, which, in turn, decrease the density of the glass and its resistance to deformation. Based on the concept introduced by Spaepen, the deformation process of MGs can be explained in terms of competing free volume creation and annihilation. An applied shear stress $\tau$ helps to reduce the activation free energy barrier so that the number of "forward" atomic jumps exceeds the number of

"backward" jumps, allowing macroscopic flow to occur [Das03c]. A two-dimensional schematic of the atomistic deformation mechanism developed for amorphous metals by Spaepen is illustrated in Figure 2.2.2 [Spa77].
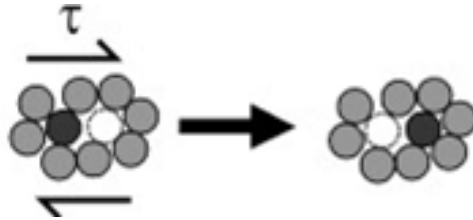


**Figure 2.2.2.**   Two-dimensional schematic of the atomistic deformation mechanism proposed for metallic glasses, including local discrete atomic jumps [Spa77].

The alternative "bubble-raft" model describing the deformation of MGs has been developed by Argon [Arg79, Arg82]. He suggested that a local rearrangement of atoms in deforming metallic glasses takes place by a shear transformation process which controls the kinetics of the macroplastic flow of glassy alloys. The shear transformation of a cluster of atoms in a disordered matter is composed of diffuse shear and concentrated (sharp) shear – see Figures 2.2.3a-c.
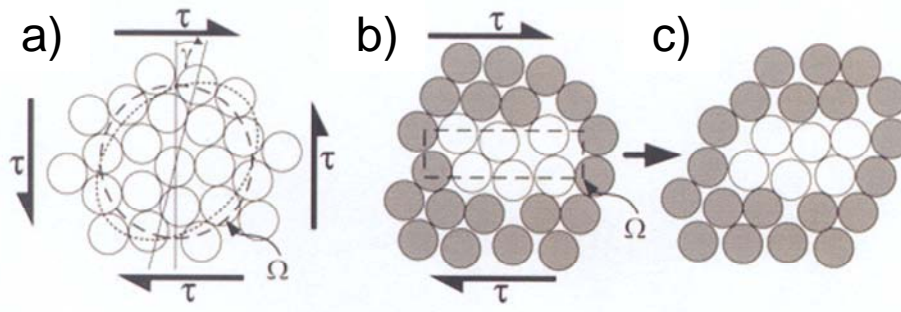


**Figure 2.2.3.**   Shear transformation process of atomic clusters through (a) diffuse shear, (b,c) two stages of concentrated shear [Arg82].

The activation volume, which undergoes the shear transformation has been indicated as $\Omega$, whereas $\gamma$ refers to as the shear strain. Generally, the homogeneous deformation, which mainly occurs at elevated temperatures, proceeds through diffuse shear, while concentrated shear favors an inhomogeneous deformation [Das03c].

Based on molecular-dynamic simulations of 2-D, two-component non-crystalline systems, Falk and Langer [Fal98] developed a new theory of low-temperature shear deformation in amorphous solids, the so-called "shear-transformation-zone" (STZ) model, which predicts that sufficiently soft non-crystalline solids are linearly unstable against forming periodic arrays of microstructural shear bands upon plastic flow [Lan01]. According to Steif and Spaepen [Ste82], the spontaneous strain localization as observed for deformed metallic glasses demands the local work-hardening coefficient $h = \partial\tau/\partial\gamma$ to be $\leq 0$. In the following concept, is has been suggested that deformation leads to a short-range-order (SRO) damage [Pol72, Pam74a], which, in turn, reduces the resistance of the material to subsequent flow. Finally, Gilman [Gil73] and Morris [Mor79] proposed a theory, which explains the strain as a consequence of the movement of dislocation-like defects (Volterra dislocations).

However, despite recent progress, much remains to be understood about the fundamentals and mechanisms of deformation and fracture of non-crystalline materials [Yav07].

*Few words more about plasticity of MGs*

Ductility, as opposed to brittleness, is the ability of a material to undergo plastic deformation before it fails [Rie93]. Due to the fact that plastic flow tends to lower stress peaks at notches and cracks as well as to smoothen the stress distribution, ductility is a remarkably desirable material feature. It is usually a quite complicate task to obtain high strength and good ductility simultaneously [Rie93]. Of course, the principle purpose of alloy design is to provide materials with an optimum combination of strength-plasticity properties for a given application.

While, in the case of crystalline metallic alloys the subject entitled "plasticity improvement" has been studied since long time, the factors contributing to the intrinsic

ductility of their newly developed glassy counterparts are far from being fully recognized. Up to date, the significant macroscopic plasticity as reported for selected BMGs has been explained to result from:

> ➢ a large Poisson ratio ν [Che75, Sch04, Lew05],
>
> ➢ nanocrystallization during deformation [Haj06, Haj07],
>
> ➢ liquid-liquid phase separation [Yao06, Kim06],
>
> ➢ the presence of a distinct short- or medium-range order [Das05],
>
> ➢ the development of glassy martensite in supercooled martensitic alloys [Das07].

For instance, the formation of nanocrystals in shear bands upon compressive loading has been reported by Hajlaoui *et al.* [Haj06, Haj07] for Zr-Al-Ni-Pd and Cu-Zr BMGs. The observed nanocrstallization phenomenon was elucidated as being due to an increase of the free volume [Yav05] and a large local temperature rise accompanying the intense concentrated shear at large shear offsets [Yav07]. It has been suggested that a heating can lead to the growth of nanocrystals which, as a consequence, act as obstacles for shear bands and crack propagation [Haj06, Haj07].


- Superior mechanical properties of metallic glass composites

The desire to improve the ductility of glassy alloys has naturally led to an exploration of materials composed of a glassy matrix with one or more discontinuous crystalline phases (see section *metallic glass matrix composites*) [Sch07]. As previously indicated, the main purpose of making a composite is to promote initiation of multiple shear bands (homogeneous distribution of the macroscopic plastic strain) as well as to hinder shear band emission (in order to decrease the shear strain on any single band and thereby delay catastrophic fracture) [Sch07]. The transfer of an externally applied load between a glassy matrix and reinforcements is a rather complex issue and the mechanisms may alter with the length-scale of the second phase. Additionally, the toughness of the composite strongly depends on the bonding between the matrix and the reinforcements [Das03c]. For instance, for ductile second phase particles embedded in a brittle matrix, a tightly bonded particle causes closure traction to the progressing crack.

The plastic deformation of the particle results in an increase of the toughness of the composite and, as a consequence, the toughness of the composite rises [Krs81].
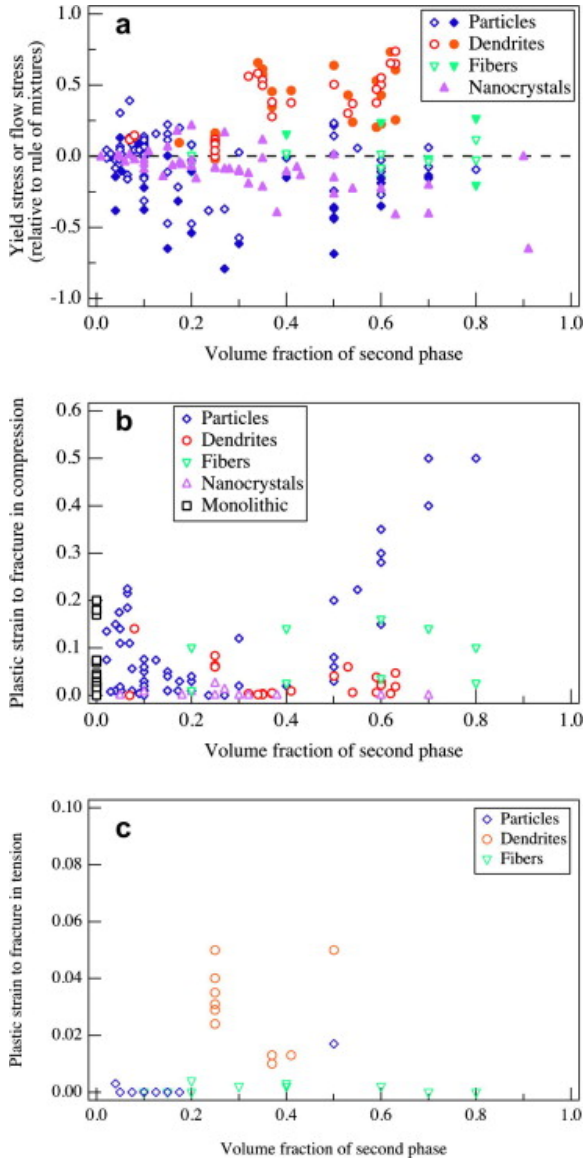


**Figure 2.2.4.** A broad analysis of a) flow stress and strain to failure in b) compression and c) tension, as the function of the volume fraction of the crystalline phase for the glassy matrix [Sch07].

The data on the mechanical response of the selected BMG-matrix composites are displayed in Figures 2.2.4a-c [Sch07]. As shown in Figure 2.2.4a, at low volume fractions of the crystalline phase ($V_f < 0.3$) the value of the yield and flow stresses of all types of composites are distributed around the rule-of-mixture line. It implies that the presence of the second phase does not cause essential changes in the macroscopic

response of the glassy matrix (with the exception, as it would be discussed next, that the plastic deformation to fracture may be greatly improved). At higher volume fractions ($V_f > 0.3$) the mechanical behavior of the BMG composite is strongly affected by the size and morphology of the reinforcing phase [Eck07b, Sch07]. While the data for larger particles and fiber reinforcements are still mainly located around the rule-of-mixture value, the data for *in-situ* composites containing a dendritic phase lie above it and the data for the nanocrystalline BMG composites are mostly below [Sch07]. Based on these findings, it can be concluded that dendritic phase dispersions are relatively more efficient for retarding macroscopic plastic flow of the matrix phase than any of the others (e.g. particles, nanocrystals) [Sch07].

In general, among all BMG-composite systems developed to date, composites containing ductile dendrites exhibit the optimum combination of high strength and large ductility [Bia05, Li07]. Under mechanical stress (compression, tension or bending) such materials manifest an improved plastic strain to failure [Hay00, Küh02, He03b, Ma03, Lee04, Bia05]. Based on the broad experimental studies performed (fractography, transmission electron microscopy, etc.) the plastic deformation of the micron-sized ductile phase reinforced *in-situ* BMG composites can be described as follows: in a first stage the ductile crystalline compound undergoes yielding and helps to transfer the slip to the surrounding amorphous matrix. Most probably, due to the strong interface between the constituent phases, the stress transfer leads to an early yielding of the composite. Shortly after the yielding of the amorphous matrix locally, the shear band nucleation occurs. Once the shear bands are formed, they start to propagate within the glassy matrix until they are stopped by second phase dispersions [Pek01]. As illustrated in Figure 2.2.5, the presence of the dendritic microstructure constitutes an effective barrier to shear front propagation. Before propagating very far, the newly generated shear bands are likely to intersect a dendrite arm [Sch07]. The shear band slip transfer between the glassy matrix and the crystalline reinforcement requires the formation of dislocations at the interface to the crystalline phase [Len90].
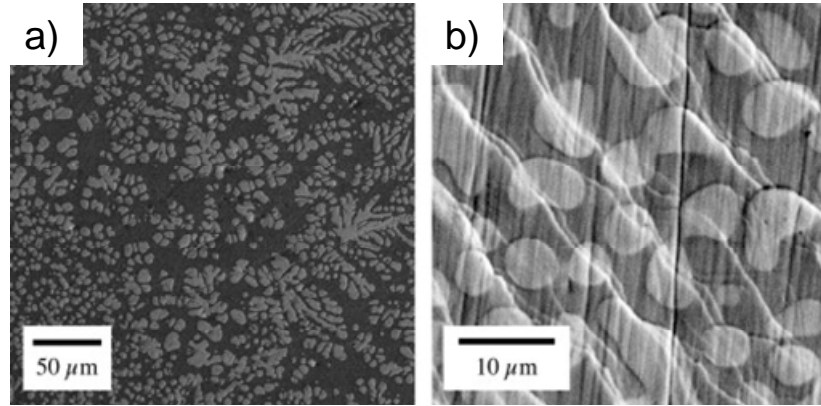
**Figure 2.2.5.**   SEM images showing the microstructure of an *in-situ* dendrite-reinforced Zr-based composite with a glass matrix [Hay00]. Image b) distinctly presents the shear band pattern array affected by the crystalline dendrites.

A considerable improvement of the ductility for Cu-based BMGs containing a small amount of dendritic phase has been reported by Bian *et al*. [Bia05]. A similar effect has also been observed for Ti-based nanostructure-matrix/b.c.c. dendrite composites [He03a]. The fractographic analysis clearly revealed that the shear band propagation is inhibited by the larger second phase. During the deformation process, the crystalline phase undergoes strain-hardening, while a localized deformation takes place in the glassy matrix. However, the presence of a second ductile phase does not always promote plasticity in a metallic glass matrix composite. The prerequisite for a significant plastic deformation of such a composite microstructure is an efficient interplay between the length-scale of the shear band and the dendrite arm spacing [Lee04, Sch07]. The systematic research on a La-Al-(Cu,Ni) BMG-dendrite composite has shown that the shear band spacing varies from 5 to 20 µm [Lee04]. At a low volume fraction of the dendritic phase ($V_f < 35\%$), the inter-dendritic spacing is on the order of 10 - 40 µm and dendrites do not obstruct shear band propagation, and thus do not contribute to an improved macroscopic ductility. However, when the reinforcement volume fraction exceeds a critical value near 40%, the inter-dendritic spacing is about 2 to 8 µm (slightly smaller than the shear band spacing). Hence, the dendrites dispersed in an amorphous matrix act as a network, which restricts shear banding to relatively isolated regions and,

as a consequence, the localized shear-off through the entire specimen is delayed [Das03c, Lee04].

# CHAPTER 3

# Materials – *processing and characterization*

In the present chapter the information on the materials selection, preparation procedures and experimental methods used to explore the structure and the mechanical behavior of the studied alloys will be provided.

## 3.1 Material selection – *from monolithic Fe-(Cr,Mo,Ga)-(P,C,B) BMG to Fe-based crystalline complex materials*

In order to explain the strategy for the material selection used in this study, we should go back to 1999, when T. D. Shen and R. B. Schwarz reported for the first time on the fabrication and magnetic behavior of Fe-(Cr,Mo,Ga)-(P,C,B) alloys [She99]. Such an alloy system has been designed according to the five empirical rules, which have been described by the authors [She99]. It was observed that an alloy, which meets these rules, possesses a deep eutectic with a low melting temperature. It can result in a high reduced glass-transition temperature $T_g/T_m$ and a large supercooled liquid region $\Delta T_x$ [Ino00]. In other words, to prepare a metallic glass by fast undercooling of melts, the above-mentioned requirements must be fulfilled. An important tool employed in the search for compositions likely to yield new bulk glassy alloys is the phase diagram. Figure 3.1.1 shows the Fe-B binary phase diagram with the marked composition $Fe_{80}B_{20}$, which is known to form a metallic glass at cooling rates on the order of $10^6$ $Ks^{-1}$. This material was selected by Shen and Schwarz as the basic composition and modified subsequently according to their criterions by the addition of metallic and metalloid constituents [She99].

Based on the work discussed above as well as on later studies performed by Stoica *et al.* [Sto02, Sto04, Sto05a], the composition $Fe_{65.5}Cr_4Mo_4Ga_4P_{12}C_5B_{5.5}$ has been chosen as the starting material. According to Stoica [Sto02, Sto05a] such bulk metallic glass-forming alloy shows good soft magnetic properties together with an excellent mechanical strength. However, the principal drawback, which severely limits its wider application as a structural material is its poor ductility at room temperature. To overcome

this problem a series of Fe-based alloys (their nominal compositions are summarized in Table 3.1.1) derived from the multi-component $Fe_{65.5}Cr_4Mo_4Ga_4P_{12}C_5B_{5.5}$ glassy alloy were investigated in detail. Emphasis was given to understand the correlation between the chemical composition, the microstructure and the mechanical response of the compressed material. The basic composition was modified by the substitution/addition of the selected elements.
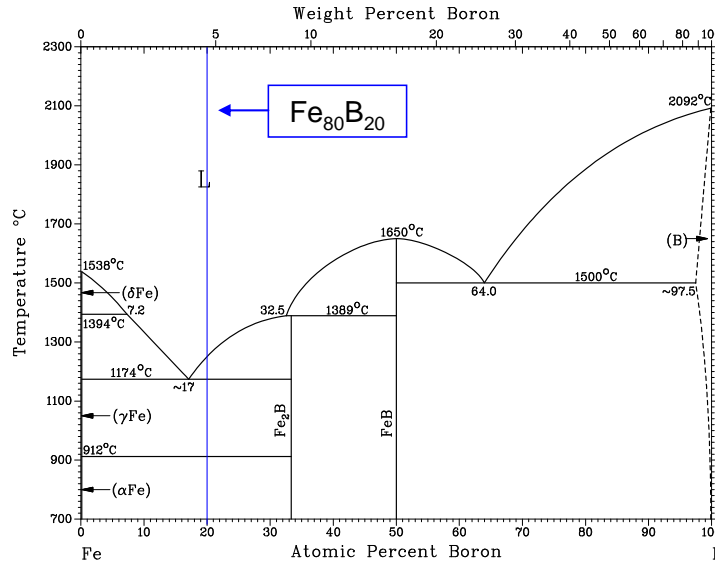


**Figure 3.1.1.** Phase diagram of the binary Fe-B system with the marked composition $Fe_{80}B_{20}$ [Mas92].

From a variety of the studied alloys (Figure 3.1.2), the Fe-Cr-Mo-Ga-Si, Fe-Cr-Mo-Ga-C and Fe-Cr-Mo-C alloy systems will be presented in this work. The way, which brought the author to the above-mentioned materials started from the binary $Fe_{94.2}Cr_{5.8}$ alloy. In the next steps, ternary $Fe_{89.1}Cr_{5.45}Mo_{5.45}$ and quaternary $Fe_{84.4}Cr_{5.2}Mo_{5.2}Ga_{5.2}$ compositions have been examined. It was expected that a detailed insight into these alloy systems will provide guiding principles for the better understanding of our multi-component base material. Armed with this knowledge, the capability of plastic deformation in the examined alloy system was verified. It was noticed that the glass-forming ability (GFA) of the investigated Fe-based systems (binary, ternary and quaternary) is not sufficient to obtain a glassy structure as a result of copper mold casting.

All the studied compositions possess crystalline nature. Subsequently performed mechanical tests revealed an amazing capacity for compression deformation in such materials. The observed very high plasticity was a promising starting-point for the further investigations. On the other hand, as it was mentioned before, the tested alloys were fully crystalline. Trying to achieve a partially amorphous material (glass-matrix composite with crystalline phase dispersions), the chemical composition has further been modified. These attempts result in the formation of a series of the Fe-based complex materials with high strength and large ductility. While the values of $\sigma_f$ are comparable with those reported for the monolithic $Fe_{65.5}Cr_4Mo_4Ga_4P_{12}C_5B_{5.5}$ BMG, the values of $\varepsilon_f$ are greatly improved for the studied cast samples. So the lack of amorphicity in the case of the derived compositions did not lead to a drop in the mechanical strength of the material. Moreover, the formation of the specific crystalline complex microstructure was of benefit for the plasticity of the investigated alloys.

**Table 3.1.1.**  Chemical composition [at.%] of the studied alloys with corresponding preparation conditions.

| Sample | Nominal composition [at. %] | Crucible material used |
|---|---|---|
| A1 | | $Al_2O_3$ |
| A2 | $Fe_{81.2}Cr_{5.2}Mo_{5.2}Ga_{5.2}Si_{3.2}$ | glassy carbon |
| B1 | | $Al_2O_3$ |
| B2 | $Fe_{78.0}Cr_{5.2}Mo_{5.2}Ga_{5.2}Si_{6.4}$ | glassy carbon |
| C | $(Fe_{84.4}Cr_{5.2}Mo_{5.2}Ga_{5.2})_{91}C_9$ | $Al_2O_3$ |
| D | $(Fe_{84.4}Cr_{5.2}Mo_{5.2}Ga_{5.2})_{83}C_{17}$ | $Al_2O_3$ |
| E | $(Fe_{89.0}Cr_{5.5}Mo_{5.5})_{91}C_9$ | $Al_2O_3$ |
| F | $(Fe_{89.0}Cr_{5.5}Mo_{5.5})_{83}C_{17}$ | $Al_2O_3$ |

**$Fe_{65.5}Cr_4Mo_4Ga_4P_{12}C_5B_{5.5}$ BMG [Sto05a]**

*starting material*

## Compositional and processing modifications

**1.**

$Fe_{94.2}\mathbf{Cr}_{5.8}$

$Fe_{89.1}\mathbf{Cr}_{5.45}Mo_{5.45}$

$Fe_{84.4}\mathbf{Cr}_{5.2}Mo_{5.2}Ga_{5.2}$

**2.**

$Fe_{94.2}\mathbf{Mn}_{5.8}$

$Fe_{89.1}\mathbf{Mn}_{5.45}Mo_{5.45}$

$Fe_{84.4}\mathbf{Mn}_{5.2}Mo_{5.2}Ga_{5.2}$

**3.**

$Fe_{79.2}\mathbf{Cr}_{10.4}Mo_{5.2}Ga_{5.2}$

$Fe_{79.2}Cr_{5.2}\mathbf{Mo}_{10.4}Ga_{5.2}$

$Fe_{79.2}Cr_{5.2}Mo_{5.2}\mathbf{Ga}_{10.4}$

**4.**

$Fe_{81.2}Cr_{5.2}Mo_{5.2}Ga_{5.2}\mathbf{Si}_{3.2}$ ⎫    $Al_2O_3$

$Fe_{78.0}Cr_{5.2}Mo_{5.2}Ga_{5.2}\mathbf{Si}_{6.4}$ ⎭ Glassy carbon

**5.**

*9 experiments*

$Fe_{84.4}Cr_{5.2}Mo_{5.2}Ga_{5.2}$ ⟨   $Al_2O_3$     1300 °C

          $SiO_2$      1400 °C

          GC       1500 °C

*Effect of carbon*          *Effect of gallium*

**6.**

$(Fe_{84.4}Cr_{5.2}Mo_{5.2}Ga_{5.2})_{100-x}\mathbf{C}_x$

x = 9,17 at.%

**7.**

$(Fe_{89.0}Cr_{5.5}Mo_{5.5})_{100-x}\mathbf{C}_x$

x = 9,17 at.%

~~Ga~~

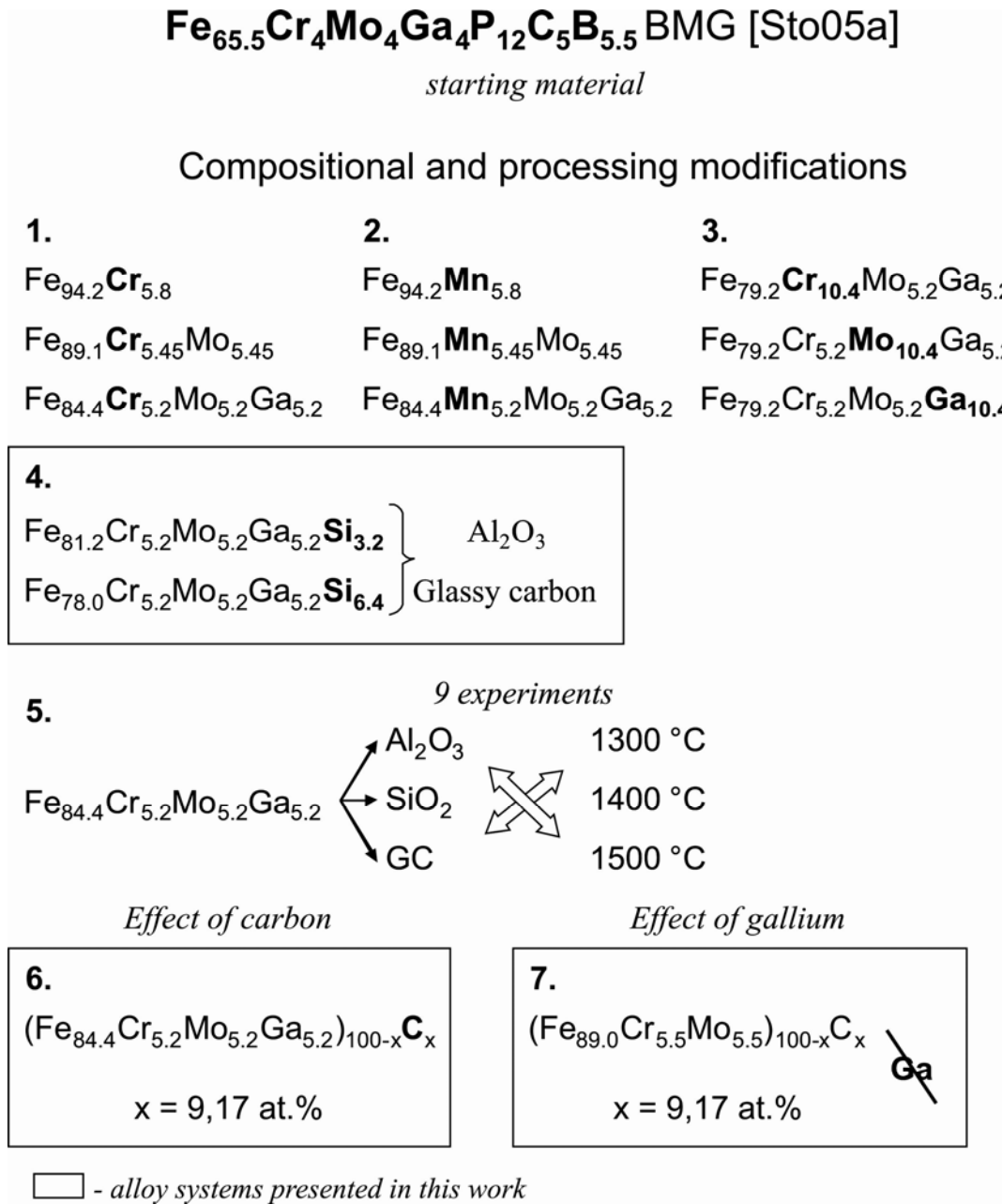☐ - *alloy systems presented in this work*

**Figure 3.1.2.** Fe-based alloy systems derived from the monolithic BMG [Sto05a].

Since the invention of the so-called "amorphous steels" [Pon03, Lu04], which exhibit fracture strengths exceeding twice that measured for conventional high-strength steels, the Fe-based composites presented here, constitute an interesting link between the "old" and the "new" generation of steels. By applying fabrication conditions typically employed for the preparation of bulk glassy alloys, the formation of the specific structure

composed of the standard phases existing in steels (austenite, martensite, carbides – see Figure 3.1.3) has been observed. As it will be shown in chapter 4 "**Results and discussion**", such a complex microstructure leads to a material with an excellent compressive behavior.
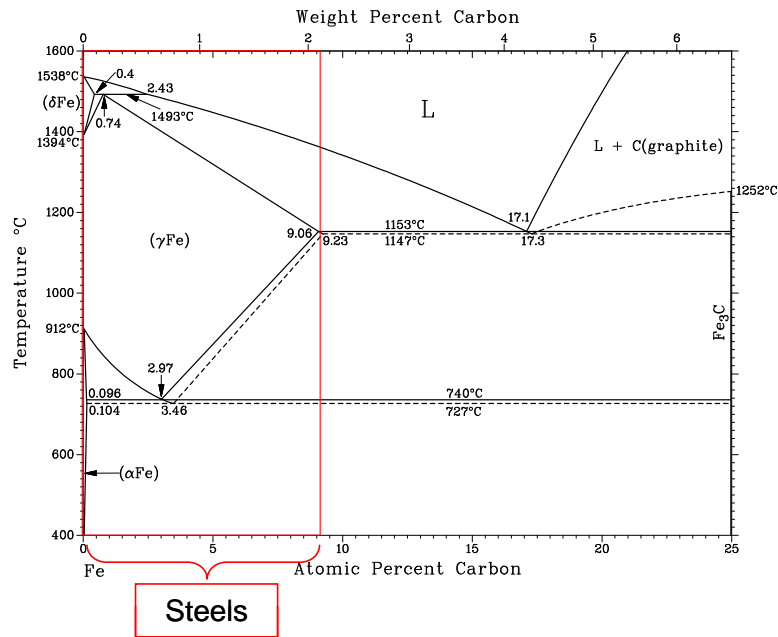


**Figure 3.1.3.** Phase diagram of the Fe-C system. The steel portion of the Fe-C phase alloy diagram covers the range between 0 and 2.08 wt.% C – as denoted by the red rectangle [Mas92].

- Master alloys – *arc and induction melting*

In a first step master alloys were prepared by melting of a mixture of high purity elements (99.9%) under a titanium-gettered argon atmosphere. The ingots were obtained either through an arc- or an induction-melting process. However, for the individual alloy systems the preparation of the master ingots proceeded in a slightly different manner. In the case of the compositions containing silicon, lumps of 50 g were produced by arc-melting. For the alloys with C addition arc-melted $Fe_{84.4}Cr_{5.2}Mo_{5.2}Ga_{5.2}$ ingots were crushed into small pieces and then re-melted with an appropriate portion of carbon (9 and

17 at.%) in an induction-casting device. The master alloys with nominal composition of $(Fe_{89.0}Cr_{5.5}Mo_{5.5})_{100-x}C_x$ with x = 9 and 17 at.% were fabricated by induction-melting. To ensure the compositional homogeneity the as-prepared ingots were repeatedly re-melted. In final, in order to remove any possible surface oxide layers, the master alloys were mechanically polished. All the apparatuses used to produce the master alloys are presented in Figures 3.1.4a-c.
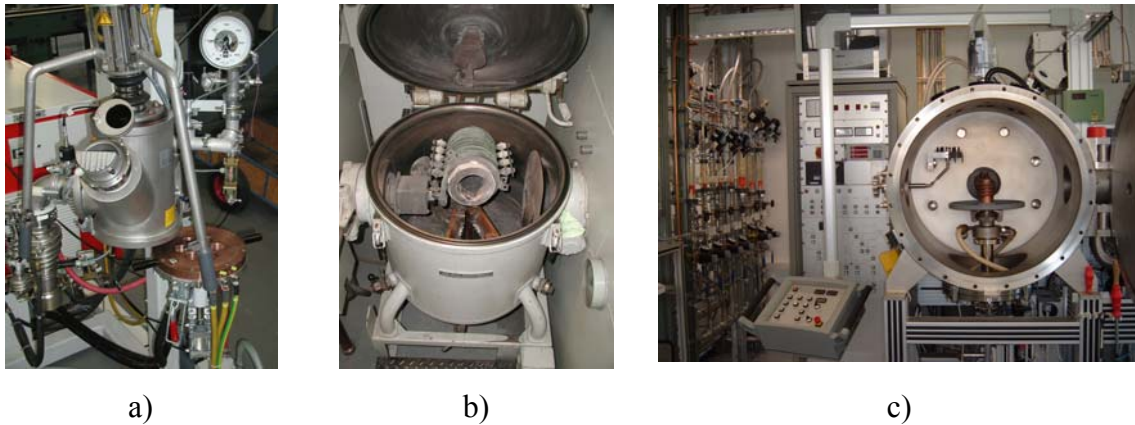


a)                                b)                                c)

**Figure 3.1.4.**    Devices employed to fabricate master alloys of the studied Fe-based materials: a) arc melter, b) induction furnace, c) cold crucible facility (IFW Dresden performance).

- Cylindrical rod – *centrifugal casting*

    The next step was dedicated to produce rod-shaped specimens (see Figure 3.1.5b). Cylinders with a length of 70 mm and a diameter of 3 mm were prepared by the centrifugal casting technique. The experimental set-up is presented in Figure 3.1.5a.

    In centrifugal casting, a permanent mold is rotated about its axis at high speed (500 rpm – centrifugal speed applied) as the molten metal is poured. In comparison with other melting processes, such a technique is time- and cost-saving. In addition, due to the

eddy currents, which are produced in the melt, the obtained melts are more homogeneous (the eddy currents effect a good mixing of the molten metals).
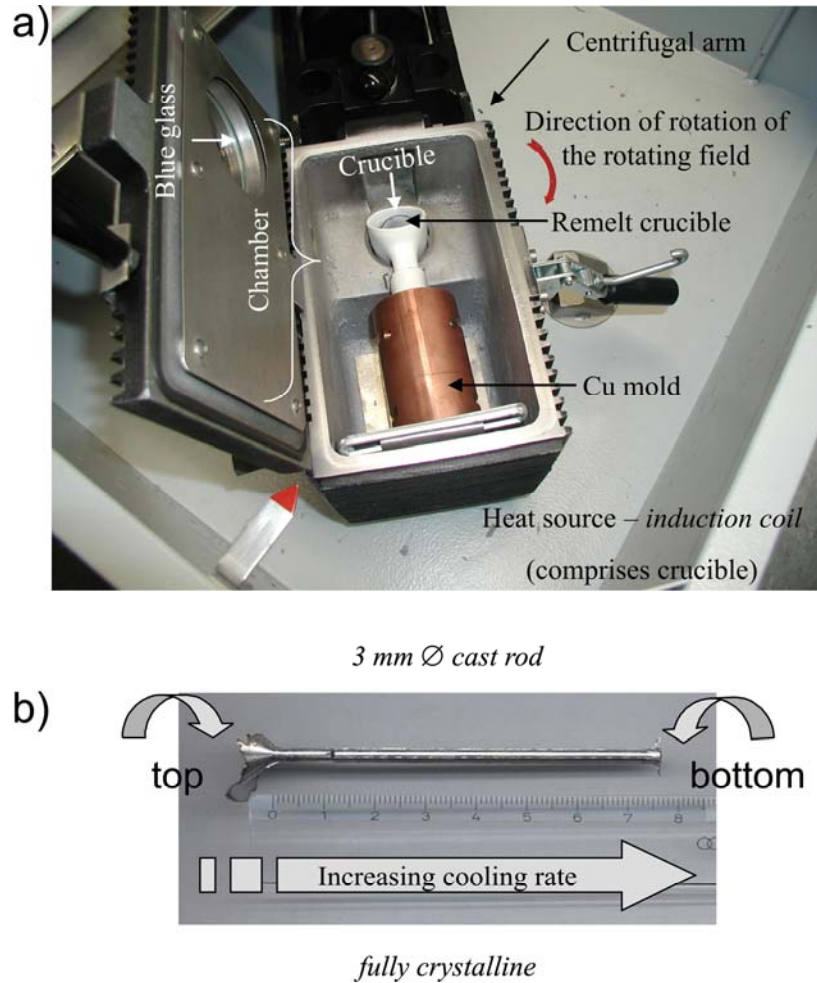


**Figure 3.1.5.**  a) – centrifugal casting facility (LINN HIGH THERM GmbH) and
b) – product of casting - *bulk cylindrical rod*.

The above-shown casting machine consists of the following components: centrifugal chamber in which the centrifugal arm and the induction coil are located. The arm accommodates the crucibles and the copper mold. A smooth run is reached due to an adjustable counter weight, which is fitted to the arm. In the case of all casting processes, the copper mold with an internal cylindrical channel of 3 mm diameter was used. The induction coil (the so-called heat source) comprises the crucibles. The high-frequency

generator (approximately 1.2 MHz) can deliver a power up to 3.3 kW. The melting can be monitored either by a blue glass, which is integrated in the cover or by an infrared-spectral pyrometer. When the alloy is molten, the coil is lowered and the casting process can be started. To avoid undesired chemical reactions with atmospheric oxygen, the closed centrifugal arm is evacuated (to $10^{-4}$ – $10^{-5}$ mbar) and subsequently fed with protective-gas (99.9% pure Ar).

For the melting process, two types of crucible material were used, a glassy carbon and a ceramic ($Al_2O_3$) crucible. However, the glassy carbon crucible has been utilized only in the case of Si-containing alloys. The strong affinity between iron and carbon (the elemental component of the crucible) in conjunction with the process conditions (high temperatures required for the melting) resulted in the formation of a complex microstructure composed of phases such as martensite and carbides. In order to avoid this phenomenon, the ensuing experiments have been carried out by using a ceramic ($Al_2O_3$) crucible. On the other hand, it has been recognized that the C "addition" strongly affects the mechanical properties of the deformed Fe-Cr-Mo-Ga-Si rods. The presence of carbon in this microstructure leads to a composite material with an excellent compressive behavior. Based on these findings, in the subsequent steps, the C-containing compositions have been prepared and widely investigated.

## 3.2 Chemical analysis

To control the purity of the master alloys (especially the oxygen content) as well as the composition deviation due to an evaporation of selected constituents upon the melting operation, a detailed chemical analysis has been carried out by the Chemical Analysis Group of the IFW Dresden (special thanks to Prof. J. Acker and Dr. W. Gruner).

The oxygen contamination level as well as the carbon concentration were evaluated by carrier gas-hot extraction in a helium atmosphere using a LECO USA TC-436 DR and in a reactive oxygen atmosphere using a LECO USA CS 244, respectively.

The procedure for the oxygen determination consists of melting and heating the specimens to temperatures of about 2500 ºC in a resistively heated furnace using graphite crucibles. At this state, due to the chemical reaction between the oxygen trapped in the molten sample and the carbon atoms, which diffuse from the graphite crucible into the

melt (formation of carbon monoxide), the oxygen level in the neighborhood of the crucible wall is decreased. In a next step, the carbon monoxide is extracted and carried away from the reaction area by a continuous helium gas flow. To determine the CO content, the gas mixture is carefully investigated by infrared radiation absorption. The carrier gas-hot extraction is the most popular technique for oxygen analysis. The total error of this method is about $\pm\, 0.01$ at.%.

The carbon content was estimated by a combustion method. The samples were melted and subsequently heated to high temperature (700 to 2700 °C) in a continuous flux of oxygen. Under such conditions, the carbon atoms, which are present in a molten alloy, undergo oxidation and, as a consequence, carbon dioxide is formed. The released $CO_2$ is then transported by the oxygen gas flow to be analyzed and quantified by infrared absorption.

The oxygen content analysis has been realized for the master alloys of all the studied Fe-based compositions (the oxygen content was found to be between 0.002 and 0.010 wt.%). The carbon determination has firstly been performed only for the master ingots of the C-containing alloys. However, due to an unexpected phase formation as observed for the selected as-cast Fe-Cr-Mo-Ga-Si rods, a carbon determination has additionally been carried out for the Si-containing specimens. The conducted analysis revealed that, while the Fe-Cr-Mo-Ga-Si alloys were carbon-free in their initial state (arc-melted ingots), the high amount of this element has been detected for the as-cast state (rod samples). As it was mentioned before, the observed composition deviation resulted from the C diffusion from the crucible (glassy carbon) into the molten alloy, during the melting process. Obviously, the Fe-Cr-Mo-Ga-Si cylinders obtained by using the $Al_2O_3$ crucible, did not comprise any carbon.

To study the chemical composition, the spectrophotometric method was employed. The analysis has been performed by using a CARL ZEISS Specord M 500 Spectrophotometer. The elemental composition has been evaluated in the following way: the specimen was dissolved in acid and the solution was mixed with an excess of reagent, which forms a colored reaction product with the initial solution. The light absorption of the colored solution was determined using ultraviolet or visible radiation of a defined wavelength. The absorption is proportional to the concentration of the dissolved element.

**3.3 Structural characterization**

In this section, the experimental techniques providing an accurate description of the microstructure of the examined alloys together with the details on the sample fabrication will be presented.

- X-ray diffraction

To discern the phase formation, which occurs upon the solidification process, a standard X-ray diffraction (XRD) analysis was performed. The experiments have been conducted by using the following apparatuses: a PHILIPS PW 3020 Bragg-Brentano diffractometer and a PANalytical Diffractometer X'Pert MPD (operated by Mrs. A. Ostwaldt) equipped with a local sensitive detector (LSD). The X-ray diffraction in reflection configuration was carried out using Co-$K_\alpha$ radiation ($\lambda$ = 1.78897 Å, 40 kV, 40 mA). The diffractometers were equipped with a secondary graphite monochromator and a sample spinner.

The disc specimens (1 mm in height) used for the XRD measurements were cut from the rods using a Struers Accutom-5 Precision Saw. Two types of cutting discs have been employed: 45U CA and 456 CA. In a subsequent step, the surfaces of such slices were mechanically ground. As-prepared discs were then placed at a PVC sample holder (such material shows no crystalline reflection, only an amorphous peak between $2\theta$ = 10° and $2\theta$ = 20°). In most cases, the X-ray diffraction patterns were collected from a single slice of the investigated alloy (very few experiments have been done in a slightly different manner: instead of one slice, several slices have been placed on the specimen holder). In order to control the structural homogeneity of the as-cast cylinders, XRD patterns were recorded from the bottom, middle and upper part of the studied rods. Depending on the composition the diffracted intensities were measured from 30° to 100°, 40° to 100° and 40° to 110° ($2\theta$) in a step mode with a step-angle of 0.05° and typical counting times ranging from 6 to 7 s per step.

In addition, an XRD analysis was conducted for the as-deformed $(Fe_{84.4}Cr_{5.2}Mo_{5.2}Ga_{5.2})_{91}C_9$ and $(Fe_{84.4}Cr_{5.2}Mo_{5.2}Ga_{5.2})_{83}C_{17}$ alloys. It was expected that such alloys subjected to compressive deformation would undergo an *austenite* → *martensite* transformation (see chapter 4 "**Results and discussion**").

For phase determination, the X'Pert HighScore Plus software was employed. In the case of the multi-component alloys the analysis of the XRD patterns constitutes a real challenge. With the aid of the knowledge and the experience of Dr. N. Mattern, the phase identification of the studied composites was performed. Furthermore, for the Fe-Cr-Mo-Ga-C alloy system, the relative amount of each phase detected was determined by Rietveld Refinement Method [You93].

- Light optical microscopy

The first images revealing the microstructure of the tested Fe-based materials have been taken by a light microscope (Epiphot 300 NIKON). The applied objective magnification varied from 10 to 100x (additional magnification – 10x eyepiece).

**Table 3.3.1.** Metallographic etchants employed to expose the microstructure of the investigated specimens.

| Etchant | Composition | Concentration | Time |
|---|---|---|---|
| Vilella's Reagent | $C_3H_8O_3$ | 22.5 ml | Seconds |
| | $HNO_3$ | 7.5 ml | |
| | HCl 32% | 15 ml | |
| (after Struers) | Distilled water | 50 ml | Seconds |
| | $(NH_4)_2S_2O_8$ | 5 g | |
| | $K_2S_2O_5$ | 2 g | |
| Nital (2%; 3%; 5%) | $C_2H_2O$ | 98 ml; 97 ml; 95 ml | Seconds |
| | $HNO_3$ | 2 ml; 3 ml; 5 ml | |
| Beraha II | Distilled water | 800 ml | Seconds |
| | HCl 32% | 400 ml | |
| | $K_2S_2O_5$ | 1 g | |
| | $NH_4HF_2$ | 48 g | |

Although, the optical microscope is the oldest and the simplest among the microscopes developed so far, the sample fabrication employed was a complex procedure, which required the following steps: the slice with a size of about 3 mm diameter and 1 mm height sawed from the as-cast rod (previously used for XRD analysis) was mounted in a special conductive resin (PROBEMET) by using a Bühler Simplimet 3000 apparatus. As-prepared specimens were subsequently ground and polished (grinding/polishing equipment - Struers RotoPol Force-4 and RotoPol-31). In particular cases, the metallographic samples were additionally etched. The chemical compositions of the etchants used are given in Table 3.3.1.

- Scanning and transmission electron microscopy

To analyze in detail the morphologies and microstructures of the studied Fe-based composites in different stages of the investigation (ingots, as-cast cylinders, as-deformed samples), electron microscopy has been employed.

In a first step, the materials were studied by scanning electron microscopy (SEM) using a PHILIPS XL30 microscope equipped with a MICROSPEC WDX (IFW Dresden facility). The experiments were done with the help of Mrs. S. Pichl, who operated the device. The SEM observations were performed on the metallographic (OM) samples. Due to the complex nature of the examined alloys, the average composition of the particular phases was determined by wavelength- and energy-dispersive X-ray spectroscopy (WDX, EDX). Moreover, careful studies of the fracture surface as well as of the deformed cross-section of the tested alloys were conducted. Such experiments were essential for the understanding of the mechanical response of Fe-based complex materials presented in this work.

The evaluation of the as-prepared state of the samples was continued by transmission electron microscopy (TEM) using a JEOL 2000 FX analytical microscope (JEOL Company) with 200 kV acceleration voltage and an EDAX energy-dispersive spectrometer. In the case of the Fe-Cr-Mo-C alloy system, TEM observations were performed using a newly purchased Tecnai T20 microscope (FEI Company) operating at 200 kV acceleration voltage coupled with an OXFORD energy-dispersive detector. The

TEM images were taken under bright and dark conditions with direct assistance of Mrs. C. Mickel (IFW Dresden).

The transmission electron microscopy was mainly employed to explore fine interdendritic phases, which could not be resolved in the OM and SEM micrographs. To confirm EDX analysis results previously obtained (SEM investigations) the composition of the matrix as well as precipitates was additionally studied by TEM-EDX. Furthermore, for individual specimens, selected area nano-diffraction patterns were recorded.

The TEM samples were prepared by Mrs. H. Kempe and Mrs. G. Scheider. The applied fabrication route was as follows: thin slices from 3 mm $\varnothing$ cast rods were manually ground to a thickness of about 100 μm using 800 grit SiC paper. As-prepared specimens were subsequently mechanically dimpled (GATAN dimpler) in order to acquire a thickness of around 10 - 20 μm in the central area of the slice. Finally, the samples were polished by argon ion milling using a GATAN precision ion-polishing system (PIPS), operating at 4 - 5 kV, with an angle between 2° and 4º.

## 3.4 Thermal analysis

The crystallinity of the as-cast rods was additionally confirmed by differential scanning calorimetry (DSC) - *a thermoanalytical technique in which the difference in the amount of heat required to increase the temperature of a sample and reference are measured as a function of temperature* [Sha72].

The DSC measurements were performed using a computer-controlled NETZSCH DSC 404 apparatus under purified argon flow. As sketched in Figure 3.4.1 such a device contains two small pans (e.g. $Al_2O_3$), which sit on a small slab of a material with a calibrated heat resistance $K$. Generally, the temperature program for a DSC analysis is designed such that the sample holder temperature increases linearly as a function of time, i.e. the heating rate $\frac{dT}{dt} = \beta$ is kept.

Compared to a reference material, the flow of heat into the sample is greater because of its heat capacity $C_p$. Due to the dissimilarity in flow $\frac{dQ}{dt}$ between specimen

and reference, a temperature difference $\Delta T$ (measured by thermocouples) through the slab is observed. In principle, the heat capacity can be estimated from this signal:

$$\Delta T = \frac{dQ}{dt} = KC_p \beta \, \Delta T \text{ and thus } C_p = \frac{\Delta T}{K\beta}. \tag{3.1}$$

When the material undergoes a phase transition, e.g. from the solid to the liquid state – melting process (change in the heat capacity occurs), the baseline of the recorded DSC signal exhibits a step. From the DSC curve the enthalpy of transition can be calculated. This is done by integrating the peak corresponding to a melting. The onset of the peak refers to the melting temperature.
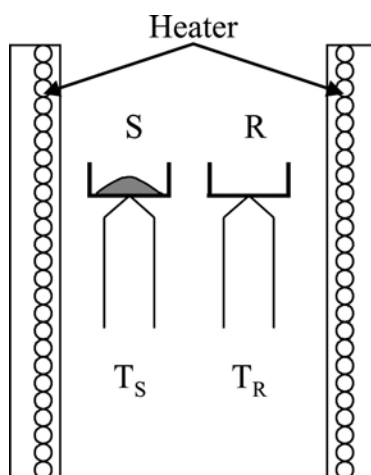


**Figure 3.4.1.**   Schematic representation of a heat flow DSC: S – sample crucible, R – reference crucible; $T_S$, $T_R$ – thermocouples.

For the DSC experiments, the $Al_2O_3$ crucibles were charged with 20 to 50 mg of the material. Constant-rate heating scans were carried out at 20 Kmin$^{-1}$. Depending on the composition, the samples were heated to 1300 – 1500 °C. Because of the crystalline nature of the examined Fe-based alloys, differential scanning calorimetry was mainly used to determine the melting points (ingot samples). Although all alloys are derived from a $Fe_{65.5}Cr_4Mo_4Ga_4P_{12}C_5B_{5.5}$ BMG, their glass-forming ability was not sufficient to

obtain an amorphous phase as a product of the casting process. A typical DSC plot for a $Fe_{65.5}Cr_4Mo_4Ga_4P_{12}C_5B_{5.5}$ glassy alloy has been shown in Figure 3.4.2 [Sto05b]. Such a curve displays: the glass transition $T_g$, followed by a crystallization event with onset $T_x$ at a higher temperature and finally an endothermic reaction corresponding to the melting of the material, where $T_{liq}$ is the onset of the liquidus temperature.
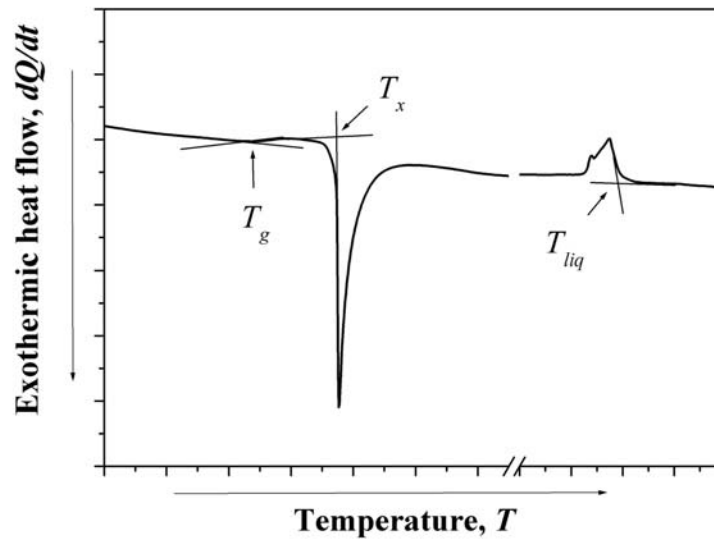


**Figure 3.4.2.**   Typical DSC trace for a $Fe_{65.5}Cr_4Mo_4Ga_4P_{12}C_5B_{5.5}$ BMG – *starting material*, demonstrating the appearance of common glass transition, crystallization and melting. $T_g$, $T_x$ and $T_{liq}$ correspond to the onsets of the respective events.

Furthermore, to investigate the thermal stability of the martensitic phase present in the microstructure of the as-cast $(Fe_{84.4}Cr_{5.2}Mo_{5.2}Ga_{5.2})_{91}C_9$ rod, DSC measurements were conducted. As it will be presented later (chapter 4 "**Results and discussion**") the obtained DSC plot shows two exothermic peaks. To analyze in detail the phase changes occurring upon heating, the alloy was annealed at temperatures above the end of the first (993 K) and the second (1053 K) exothermic DSC step. The microstructures of the as-annealed rods were subsequently examined by means of XRD and SEM.

## 3.5 Mechanical characterization

• Room temperature compression tests

As mentioned before (chapter 1 **"Introduction"**), the main emphasis in the present work was given to improve the plasticity of the studied Fe-based alloys, which were derived from the monolithic $Fe_{65.5}Cr_4Mo_4Ga_4P_{12}C_5B_{5.5}$ BMG (high-strength but extremely brittle material). To determine the deformation behavior of the developed composites, room temperature compression tests were carried out. The measurements have been performed (great thanks to Mr. H.-J. Klauß, IFW Dresden) using an electromechanical INSTRON 8562 testing device at a strain rate of $10^{-4}$ $s^{-1}$ The general mechanical response of the deformed metallic material is illustrated in Figure 3.5.1 [Got07]. The outlined *stress–strain curve* is a graphical representation of the relationship between stress $\sigma$, which is defined as force acting on the unit area over which the force is applied (see Eq. 4.1), and strain $\varepsilon$, derived from measuring the change in dimension per unit length - see Eq. 4.2 [Ask03].

$$\sigma = \frac{F}{A_0},$$ (4.1)

where $F$ = applied force, $A$ = initial cross-sectional area of the specimen and

$$\varepsilon = \frac{\Delta l}{l_0},$$ (4.2)

where $l_0$ = initial length of the specimen, $\Delta l$ = change of length after force is applied.

Eqs. 4.1 and 4.2 are related to *engineering values* of stress and strain. However, due to the fact that the area of the deformed sample continually changes, the so-called *true stress* and *true strain* are calculated in order to obtain precise results [Ask03].

$$\sigma = \frac{F}{A},$$ (4.3)

where $F$ = applied force, $A$ = actual area of the specimen and

$$\varepsilon = \ln\left(\frac{l}{l_0}\right),$$ (4.4)

where $l_0$ = initial length of the specimen, $l$ = final length.

The relation between the true $\sigma$-$\varepsilon$ diagram and the engineering $\sigma$-$\varepsilon$ diagram has been shown in the inset in Figure 3.5.1. All stress-strain curves plotted for the studied Fe-based composites (chapter 4 **"Results and discussion"**) correspond to true values. In other words, stress and strain are calculated based on the instantaneous dimensions of the sample.
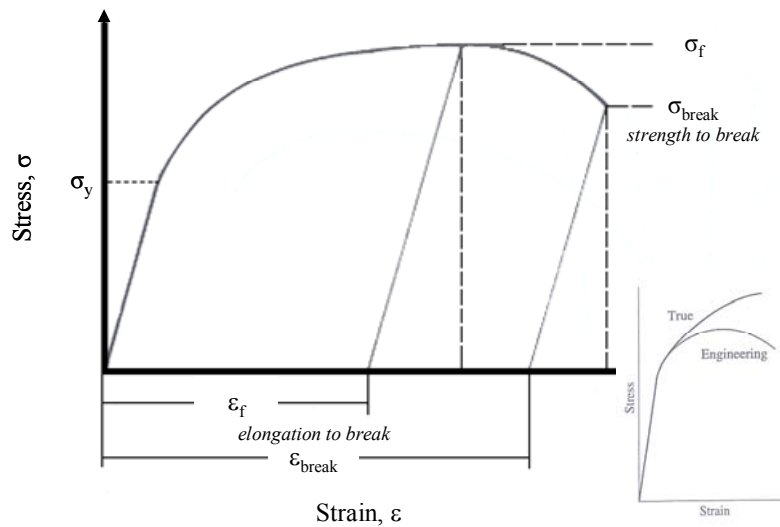


**Figure 3.5.1.** Typical stress-strain curve for a metallic material. In addition, the properties obtained from the mechanical test have been marked. Comparison between true and engineering $\sigma$-$\varepsilon$ diagrams is presented in the inset [Ask03, Got07].

Based on the obtained stress–strain diagrams the following mechanical characteristics were determined: yield strength ($\sigma_y$) – *the critical stress value needed to initiate plastic deformation*, strain at offset yield ($\varepsilon_y$), Young's modulus, ultimate (fracture) compression strain ($\varepsilon_f$) and ultimate (fracture) compression strength ($\sigma_f$). The linear region visible in Figure 3.5.1 corresponds to elastic deformation of a material. In this region a material follows Hooke's law:

$$\sigma = E \cdot \varepsilon \,, \tag{4.2}$$

where E refers to Young's modulus [Ask03].

Figure 3.5.2 depicts an as-cast cylinder. From such a rod, the compression test specimens with dimensions of 3 mm diameter × 6 mm length were prepared. Additionally, to investigate the mechanical properties of the selected pre-alloyed ingots (results not presented here), the compression test samples were prepared using the electro-erosive sawing technique. To avoid the effect of friction between the sample and the punches, the contact surfaces of the cylinders were ground and polished. At least two experiments were conducted for each rod to obtain an exact result.
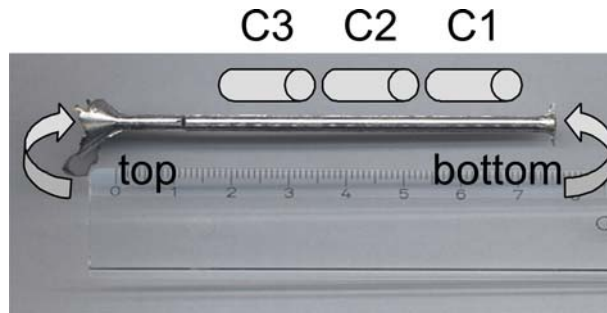


**Figure 3.5.2.** Schematic representation of the compression test specimens (cylinders C1, C2 and C3) cut from the bottom, the middle and the top of the 3 mm ∅ cast rod.

In order to inspect the fracture features, the microstructure as well as the fracture surface of the compressed specimens were then carefully studied by SEM (chapter 4 **"Results and discussion"**). These fractographic observations provided a framework to relate the mechanical behavior to the microstructure of the discerned Fe-based composites. Based on these findings, the new complex materials with superior mechanical properties compared to the fully glassy reference $Fe_{65.5}Cr_4Mo_4Ga_4P_{12}C_5B_{5.5}$ alloy were developed.

- Vickers hardness measurements

Because of the complexity of the studied materials, it was essential to determine the properties of the individual compounds. To provide the information on the mechanical behavior of the individual phases as well as of the whole alloys, microhardness measurements were done using a computer-controlled Struers Duramin 5 Vickers hardness tester (great thanks to Mrs. M. Gründlich for her assistance). The tests were carried out using a typical diamond indenter in the shape of a pyramid with a square base and an angle of 136° between opposite faces. The Vickers number (*HV*) was estimated according to:

$$HV = 0.189 \frac{F}{d^2},$$ 
(4.3)

where F is the applied load and d is the indentation diagonal.

Loads of 4.9 N and 9.8 N were applied for 10 s. As minimum 10 indents were conducted for each phase to obtain an accurate result. For the indentation experiments, already prepared metallographic (OM, SEM) specimens were employed.

*"…The knowledge and understanding of the relevant materials properties is the first step toward improving these properties and/or developing new materials with superior properties…"* [Mug93]

# CHAPTER 4

## Results and discussion - *searching for new high-strength and ductile materials*

Owing to the rapidity of technological progress, novel materials with a variety of unique properties are constantly required. One of the basic demands of present materials science and engineering is to develop new materials with an improved strength-plasticity balance. Considering conventional crystalline materials such an enhancement can be achieved by a **composite structure formation**. A suitable matrix can be just the basis upon which to optimize microstructure and properties through the second phase dispersion [Gre07].

*"…but what about the amorphous alloys?"*

From the earliest studies of glassy alloys, it was obvious that they possess a range of unique, interesting properties. Compared to common crystalline metallic materials BMGs show outstanding strength, elastic strain (~2%), and elastic energy storage. Unfortunately, the principal drawback, which severely hampers their wider application, is their little macroscopic plasticity at room temperature. Metallic glasses tend to suffer from work-softening and an extreme localization of plastic flow into shear bands [Eck07b, Gre07]. To overcome this problem, the concept of designing heterogeneous microstructures by combining a glassy matrix with second phase particles was developed [Eck07b]. It was recognized that composite strategies, successfully applied to crystalline alloys, can also be used for amorphous materials (i.e. Ti-, Zr-based). Subjected to mechanical stress, such BMG composites display a better performance than their monolithic counterparts [Eck07b]. Consequently, the goal of this work was to develop a Fe-based BMG composite material with enhanced plasticity.

This chapter presents studies on the development of new high-strength and ductile Fe-based complex alloys. The correlation between three major materials issues: processing → structure → mechanical properties will be a subject of the following chapter. The goal is to obtain a complex microstructure, which essentially consists of soft dendrites embedded in a hard matrix, leading to a material with excellent mechanical behavior.

## 4.1 The Fe-Cr-Mo-Ga-Si alloy system – *1ˢᵗ step*

The very first experiments have been performed for binary $Fe_{94.2}Cr_{5.8}$, ternary $Fe_{89.1}Cr_{5.45}Mo_{5.45}$ and quaternary $Fe_{84.4}Cr_{5.2}Mo_{5.2}Ga_{5.2}$ alloy compositions. The investigated alloys were derived from the $Fe_{65.5}Cr_4Mo_4Ga_4P_{12}C_5B_{5.5}$ BMG by substitution of the particular elements in order to ascertain the capability of plastic deformation. It was observed that the $Fe_{84.4}Cr_{5.2}Mo_{5.2}Ga_{5.2}$ as-cast sample displays a complex microstructure, while the binary and the ternary systems exhibit the formation of a single phase structure. As it was expected, subsequent compression tests showed considerable differences in the mechanical response of the studied compositions. The appearance of a composite microstructure has resulted in excellent mechanical properties – high strength connected with good ductility. In contrary, the single-phase rods manifested an amazing capacity for compressive deformation (fracture did not occur). Based on the promising mechanical characteristics as found for the Fe-Cr-Mo-Ga alloy, a new series of rods was fabricated. Surprisingly, the primary results have not been reproduced. To resolve the problem, careful studies on the chemistry of the master alloy and the as-prepared state by mass spectrometry were conducted. The detailed chemical analysis revealed the presence of a certain amount of silicon in the as-cast state. According to these findings, $Fe_{81.2}Cr_{5.2}Mo_{5.2}Ga_{5.2}Si_{3.2}$ (A) and $Fe_{78.0}Cr_{5.2}Mo_{5.2}Ga_{5.2}Si_{6.4}$ (B) alloys were prepared. It was assumed that silicon additions can play an important role for the composite structure formation as observed for the cast $Fe_{84.4}Cr_{5.2}Mo_{5.2}Ga_{5.2}$ specimen. To optimize the processing conditions, two types of crucible materials were applied: $Al_2O_3$ and glassy carbon. The microstructural investigations provided further surprising results. By using a glassy carbon crucible, a complex structure is formed. The series of samples cast by using a ceramic crucible demonstrated a single-phase formation. In recognition of all facts, it became clear that not silicon but carbon, which diffuses from the crucible into the molten alloy, is responsible for the complex structure, which occurs after casting. The carbon presence was firstly detected by wavelength dispersive X-ray spectroscopy (SEM-WDX). In order to determine its concentration chemical methods were subsequently employed. On the basis of the mentioned-above findings, it was recognized that in order to design a material with a desired microstructure, the process conditions must be precisely controlled.

- Effect of the processing route on phase formation

The XRD patterns for $Fe_{81.2}Cr_{5.2}Mo_{5.2}Ga_{5.2}Si_{3.2}$ (A) and $Fe_{78.0}Cr_{5.2}Mo_{5.2}Ga_{5.2}Si_{6.4}$ (B) as-cast cylinders are displayed in Figure 4.1.1. The obtained results clearly indicate that these multi-component alloys are fully crystalline. However, due to the miscellaneous manufacturing routes employed (different crucible materials used) significant dissimilarities in the microstructure of particular samples were noticed. For example, specimens (A1) and (B1) ($Al_2O_3$ crucible) manifest a single-phase structure, while the rods prepared by using a GC crucible are composed of a mixture of phases. The alloys (A1) and (B1) reveal the formation of a b.c.c. $\alpha$-Fe solid solution. The lattice parameter of $\alpha$-Fe calculated by means of the Bragg equation [Kit05]

$$2d\sin\theta = \lambda \rightarrow \frac{1}{d^2} = \frac{h^2 + k^2 + l^2}{a^2} \rightarrow a = \frac{\lambda\sqrt{\sum h_i^2}}{2\sin\theta} \qquad (4.1)$$

was: a = 0.2891 nm for sample (A1) and a = 0.2888 nm for sample (B1), respectively. Due to the constituents dissolved in the lattice, the estimated values are slightly higher in comparison with the lattice constant reported for b.c.c. $\alpha$-Fe (a = 0.2886). In the case of sample (A2) the dominant Bragg peaks can be assigned to a f.c.c. austenitic phase. Additional visible reflections correspond either to a hexagonal (hP3) $Mo_2C$ phase or a $MoSi_2$ phase. The microstructure of alloy (B2) is mainly composed of an austenite ($\gamma$-Fe) and a b.c.t. martensitic phase. Moreover, several weaker peaks belonging to one or more unknown crystalline phases are present.

Obviously, differences in the microstructure of the investigated samples ((A1) + (B1) and (A2) + (B2)) are due to C contamination. The carbon concentration of alloys (A2) and (B2) was evaluated to be 14.2 at.% (3.33 wt.%) and 7.0 at.% (1.54 wt.%), respectively.

The appearance of such an element in the structure of as-cast materials causes considerable changes in phase formation, and hence, as it will be shown, in the mechanical behavior of the examined Fe-based rods.
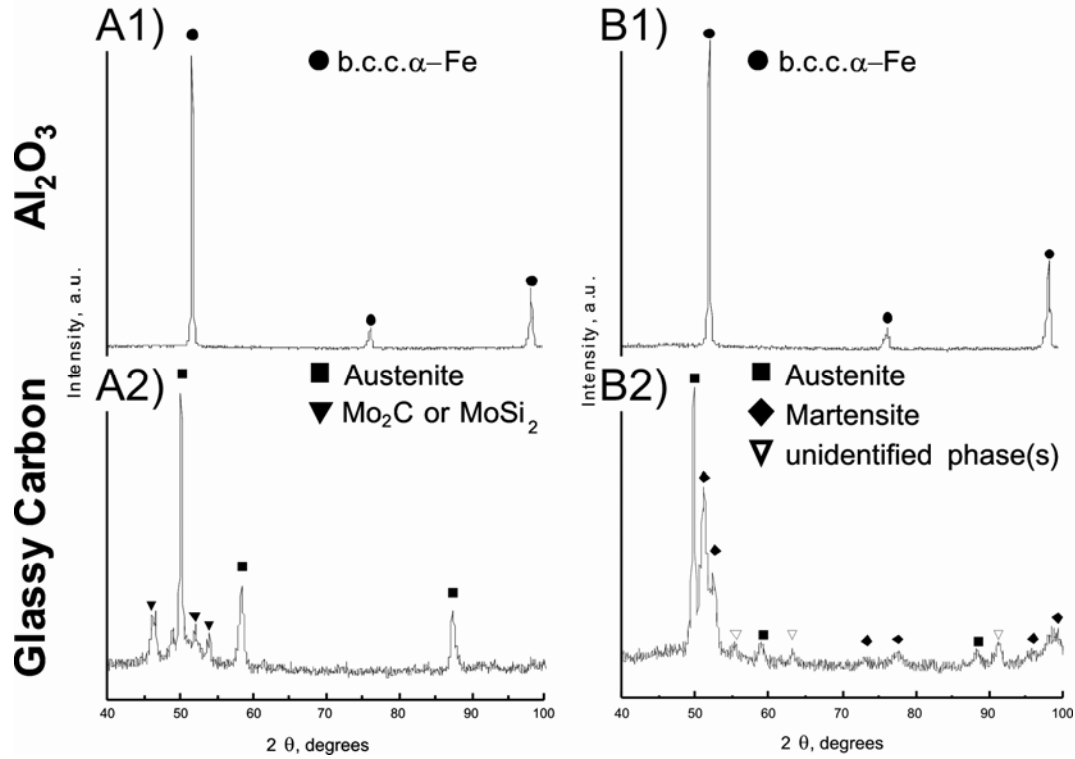
**Figure 4.1.1.** XRD patterns for as-cast alloy (A) $Fe_{81.2}Cr_{5.2}Mo_{5.2}Ga_{5.2}Si_{3.2}$ and alloy (B) $Fe_{78.0}Cr_{5.2}Mo_{5.2}Ga_{5.2}Si_{6.4}$ prepared by using two different crucible materials: $Al_2O_3$ ((A1) and (B1)) and glassy carbon ((A2) and (B2)). The obtained patterns demonstrate the strong relationship between the applied crucible and the resulting microstructure of the as-cast samples.

- Structural observation of bulk cast samples

The following section will present the structural observation results obtained for $Fe_{81.2}Cr_{5.2}Mo_{5.2}Ga_{5.2}Si_{3.2}$ (A) and $Fe_{78.0}Cr_{5.2}Mo_{5.2}Ga_{5.2}Si_{6.4}$ (B) bulk cast samples.

The first studies on the microstructure of master alloys and as-prepared specimens were done by optical microscopy (OM) (not presented here). However, to unequivocally identify the particular phases, a more detailed insight into the materials structure was gained by means of scanning and transmission electron microscopy (SEM, TEM).

The SEM micrographs in Figures 4.1.2a and b illustrate the spatial distribution, the size and the volume fraction of the phases in the center area of the examined cylinders.
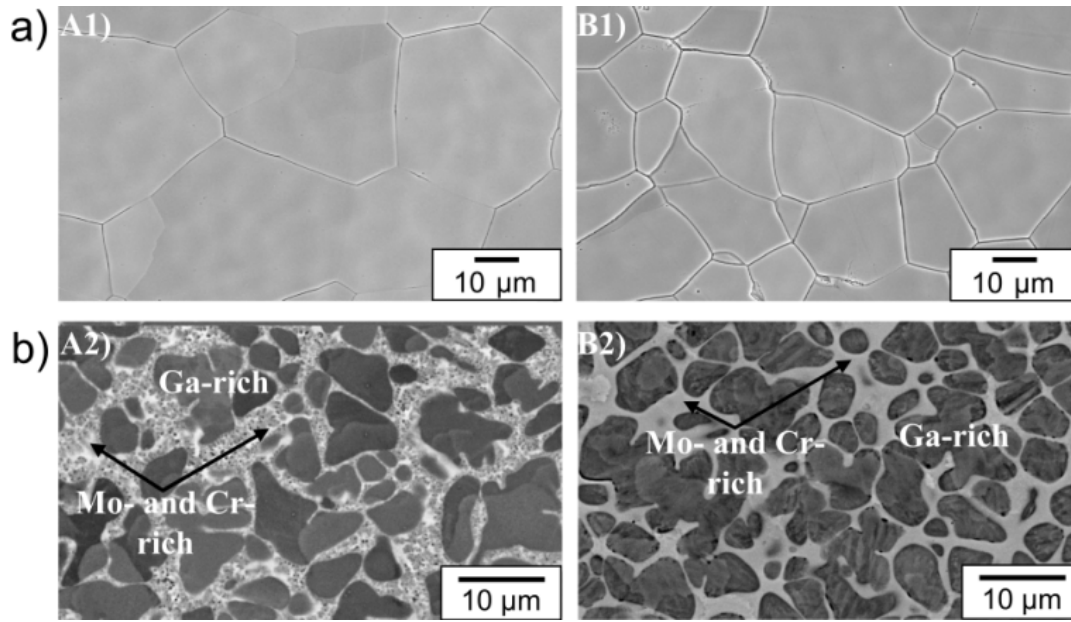
**Figure 4.1.2.**  SEM micrographs taken from the middle part of $Fe_{81.2}Cr_{5.2}Mo_{5.2}Ga_{5.2}Si_{3.2}$ ((A1), (A2)) and $Fe_{78.0}Cr_{5.2}Mo_{5.2}Ga_{5.2}Si_{6.4}$ ((B1), (B2)) bulk cast samples. Fig. 4.1.2a) displays the coarse-grained single-phase microstructure; b) presents the mixture of the micron-sized Ga-rich phase (dark dendrites) and the Mo- and Cr-rich matrix (bright areas).

The revealed microstructures clearly demonstrate noticeable dissimilarities in the phase formation for samples prepared under different conditions. As shown in Figure 4.1.2a alloys (A1) and (B1) possess a homogeneous structure composed of micron-sized b.c.c. $\alpha$-Fe phase (according to X-ray diffraction analysis). In contrast, samples (A2) and (B2) manifest the formation of a mixture of different phases. The main phase (dark grey) was identified to be f.c.c. $\gamma$-Fe. Based on the XRD measurements, the surrounding phase can either be assigned to Mo-carbide or $MoSi_2$ for alloy (A2), and a mixture of a martensite and some unidentified compound(s) for alloy (B2).

To discern the chemical composition of the individual areas as well as to corroborate the homogeneity of the as-cast samples (A1) and (B1), energy-dispersive X-ray analysis (EDX) was conducted. The EDX results are listed in Table 4.1.1.

**Table 4.1.1.**    EDX analysis results obtained for rod-shaped samples (A) and (B). The nominal compositions of the studied alloys are shown for comparison. This analytical method cannot be applied to light elements (for example C) estimation. In the case of the C-containing alloys (A2) and (B2) the EDX analysis was mainly employed to get an overview on the distribution of the individual alloy constituents.

|  | Elements, [at.%] | | | | |
|  | Fe | Cr | Mo | Ga | Si |
|---|---|---|---|---|---|
| **Alloy (A)** | **81.2** | **5.2** | **5.2** | **5.2** | **3.2** |
| A1 | 82.2 | 5.4 | 4.6 | 4.8 | 2.9 |
| A2 – *f.c.c. γ-Fe* | 83.9 | 3.3 | 1.8 | 7.6 | 3.4 |
| A2 – *matrix* | 77.2 | 6.7 | 8.6 | 3.4 | 4.2 |
| **Alloy (B)** | **78.0** | **5.2** | **5.2** | **5.2** | **6.4** |
| B1 | 79.7 | 5.6 | 4.2 | 4.4 | 6.1 |
| B2 – *f.c.c. γ-Fe* | 82.3 | 4.0 | 1.7 | 6.4 | 5.6 |
| B2 – *matrix* | 69.6 | 6.6 | 13.8 | 4.3 | 5.7 |

In conclusion, it was found that the composite-structured alloys ((A2), (B2)) are essentially composed of Ga-enriched particles dispersed in a Cr- and Mo-enriched matrix. Moreover, the average compositions evaluated for the single-phase specimens ((A1), (B1)) are in good agreement with the given nominal compositions. Additionally carried out wavelength-dispersive X-ray spectroscopy (WDX) (qualitative analysis) has confirmed the presence of carbon in the microstructure of alloys (A2) and (B2). Carbon is mainly situated in the matrix, which is enriched with chromium and molybdenum. Such elements are well known for their tendency to form carbides.

The microstructure of selected as-cast rods has also been observed by transmission electron microscopy. The microstructure features are presented in Figures 4.1.3a-c. For both samples (A2) and (B2), bright-field TEM images have affirmed the presence of crystalline, micron-sized particles in a parent phase. However, considering the individual alloys, certain differences in the shape and the morphology of the dendrites

were observed. In the case of the structure shown on the first image the precipitates were found to nucleate in a more ellipsoidal shape. For alloy (B2) the spherical precipitates containing a high number of twins are visible.
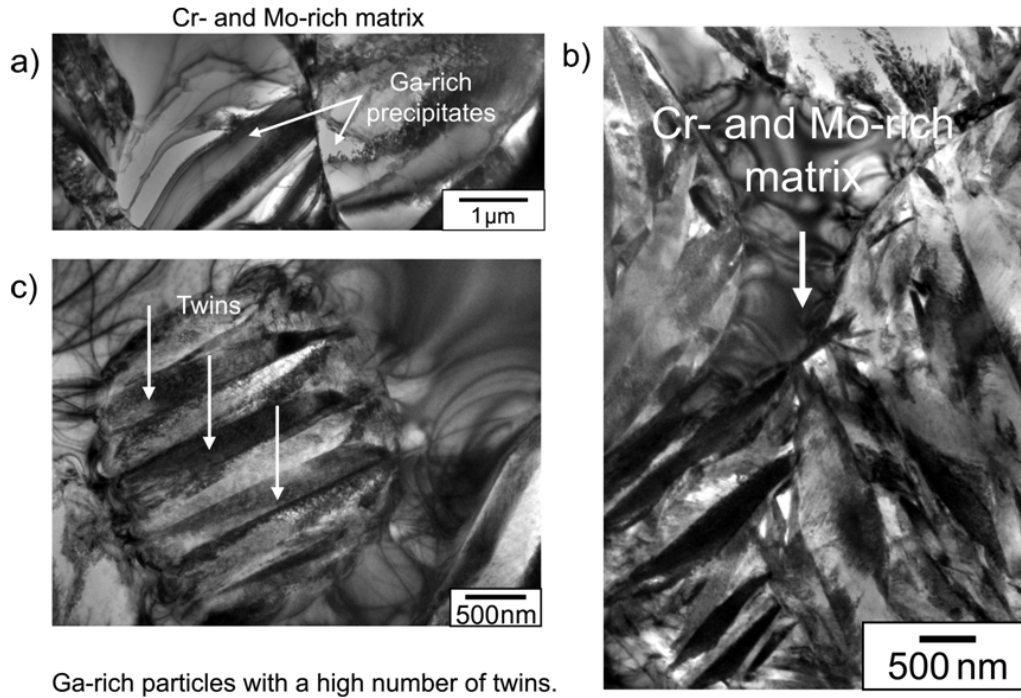


**Figure 4.1.3.** Bright-field TEM images showing microstructural features of as-cast alloys: (a) - $Fe_{81.2}Cr_{5.2}Mo_{5.2}Ga_{5.2}Si_{3.2}$ (A2) and (b,c) - $Fe_{78.0}Cr_{5.2}Mo_{5.2}Ga_{5.2}Si_{6.4}$ (B2).

Subsequently conducted EDX experiments have shown an enrichment in Ga in the f.c.c. γ-Fe phase and of Cr and Mo in the matrix.

- Mechanical investigations

Plastic deformability, especially the correlation between the structure and the mechanical response of the investigated Fe-Cr-Mo-Ga-Si alloy system is the focus of the present section. According to the structure characterization given-above, noticeable dissimilarities in the mechanical behavior of the compressed cylinders were revealed. Evidently, such differences are due to the "unplanned" compositional modifications (C

appearance), which result in a complex-structure formation. As it will be presented next, the composite materials (A2) and (B2) exhibit superior mechanical properties compared to their single-phase counterparts (carbon-free alloys (A1) and (B1)).

Although the examined multi-component complex alloys are fully crystalline (their GFA is not sufficient to reach the glassy state upon solidification), the strength values reported for them are comparable with those obtained for monolithic ferrous BMGs [Sto05a, Sto05b]. However, in contrast to the high-strength but brittle Fe-based amorphous alloys, the materials developed here display a large compressive plasticity.

To study the mechanical properties of the $Fe_{81.2}Cr_{5.2}Mo_{5.2}Ga_{5.2}Si_{3.2}$ (A) and $Fe_{78.0}Cr_{5.2}Mo_{5.2}Ga_{5.2}Si_{6.4}$ (B) as-cast alloys, room temperature compressive tests were carried out. The obtained true stress-strain curves for the compressed rods are exemplified in Figure 4.1.4. For comparison the results reported by Stoica *et al.* [Sto05b] for the $Fe_{65.5}Cr_4Mo_4Ga_4P_{12}C_5B_{5.5}$ bulk glassy alloy are additionally shown. Mechanical characteristics derived from the performed measurements are summarized in Table 4.1.2. The fracture behavior of the deformed compression specimens depends very much on the alloy microstructure. The samples possessing a complex structure exhibit a very high fracture strength of about $\sigma_f$ = 2.9 GPa (A2) and $\sigma_f$ = 3.2 GPa (B2). These values are similar to the fracture strength of the reference BMG, $\sigma_f$ = 3.27 GPa (2.5 mm diameter cylinder). Unfortunately, the corresponding yield stress decreases remarkably from $\sigma_y$ = 3.27 GPa (BMG) to $\sigma_y$ = 1.5 GPa for specimen (A2) and $\sigma_y$ = 1.4 GPa for specimen (B2), respectively.

On the other hand, compared to the as-cast $Fe_{65.5}Cr_4Mo_4Ga_4P_{12}C_5B_{5.5}$ rod, there is a significant increase in the plasticity for the investigated crystalline samples. While the reference material demonstrates almost no plastic deformation to failure ($\varepsilon_{pl}$ = 0.12%), the studied alloys (A2) and (B2) are able to sustain up to 12% and 5% pure plastic strain.

It has further been recognized that, in contrast to composite samples described above, the single-phase alloys (A1) and (B1) subjected to the compression loading manifest noticeably dissimilarities in a deformation mode. These alloys possess an amazing capacity for plastic deformation, $\varepsilon$ > 140% (fracture did not occur). Based on these findings it is concluded that the appearance of the specific complex microstructure leads to a material with very high compressive strength combined with a good ductility,

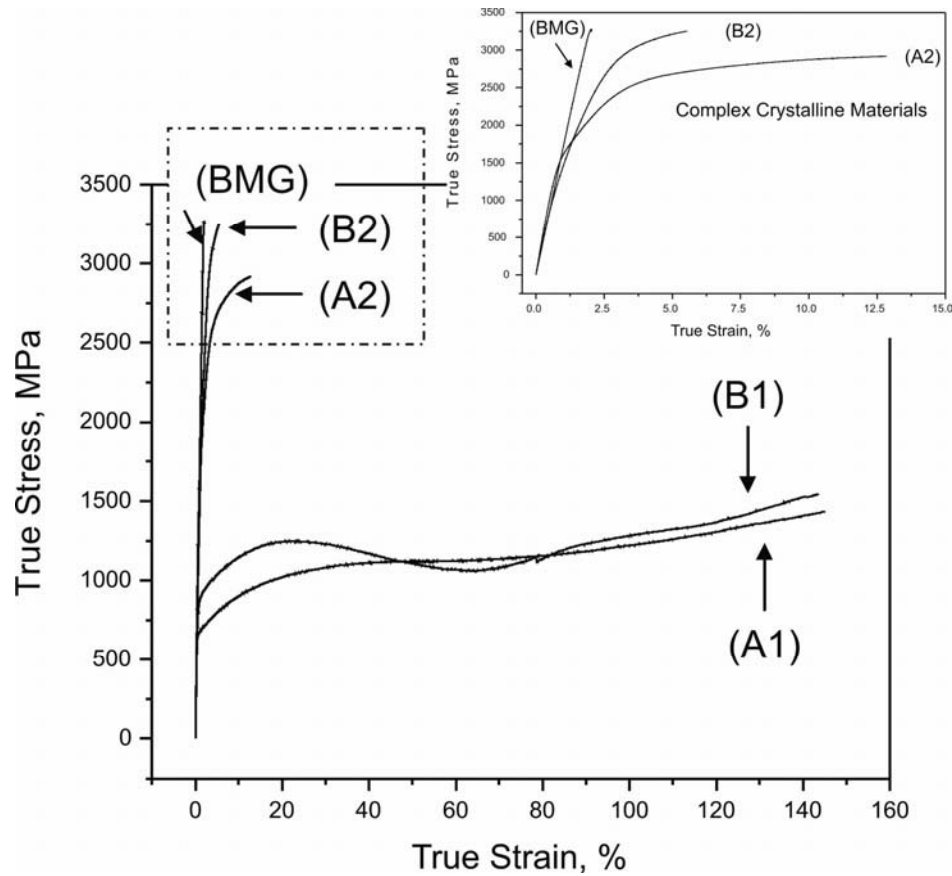whereas the formation of the single-phase microstructure results in an extremely high plasticity.



**Figure 4.1.4.**  Room temperature true stress-strain curves of $Fe_{81.2}Cr_{5.2}Mo_{5.2}Ga_{5.2}Si_{3.2}$ – (A1) ($Al_2O_3$); (A2) (GC), $Fe_{78.0}Cr_{5.2}Mo_{5.2}Ga_{5.2}Si_{6.4}$ – (B1) ($Al_2O_3$); (B2) (GC) and $Fe_{65.5}Cr_4Mo_4Ga_4P_{12}C_5B_{5.5}$ (BMG) alloys subjected to compressive deformation. The inset shows enlarged selected curves (marked by dashed line). Compared to the starting fully glassy composition, a significant improvement in compressive plastic strain for the Fe-based complex materials is observed. Furthermore, the strong relationship between the chemistry, the microstructure and the mechanical behavior for the studied alloys is demonstrated.

**Table 4.1.2.**   Results of room temperature compression tests for the as-cast samples (A1), (A2), (B1) and (B2): Young's modulus $E$, yield stress $\sigma_y$, yield strain $\varepsilon_y$, fracture stress $\sigma_f$, and fracture strain $\varepsilon_f$. The mechanical characteristics of the $Fe_{65.5}Cr_4Mo_4Ga_4P_{12}C_5B_{5.5}$ BMG are given for comparison [Sto05b].

| Alloy/ sample dimensions | True values | | | | |
|---|---|---|---|---|---|
| | $E$ [GPa] | $\sigma_y$ [MPa] | $\varepsilon_y$ [%] | $\sigma_f$ [MPa] | $\varepsilon_f$ [%] |
| (A1) / Ø 3 mm | 195 | 646 | - | - | > 140 |
| (A2) / Ø 3 mm | 212 | 1562 | 0.9 | 2920 | 13 |
| (B1) / Ø 3 mm | 190 | 640 | - | - | > 140 |
| (B2) / Ø 3 mm | 185 | 1409 | 0.9 | 3253 | 6.0 |
| (BMG) / Ø 2.5 mm | 170 | 3270 | 1.91 | 3270 | 2.03 |

To determine the properties of the particular phases hardness measurements were done for samples (A2) and (B2). According to WDX analysis, it was assumed that differences in the carbon concentration between the precipitated γ-Fe phase and the matrix phase(s) are reflected by their hardness. In essence, the investigated composites appear to consist of soft Ga-enriched dendrites (microhardness$_{A2,B2}$ ≈ 4.2 GPa) embedded in a hard Cr- and Mo-enriched matrix (microhardness$_{A2}$ ≈ 6.28 GPa and microhardness$_{B2}$ ≈ 9.61 GPa). Unluckily, there are no literature data on the hardness of the as-cast $Fe_{65.5}Cr_4Mo_4Ga_4P_{12}C_5B_{5.5}$ rod-shaped sample available. However, as reported by Stoica *et al.* [Sto05b] the Vickers hardness measured for the as-cast bar with the same overall composition is around 8 GPa, which agrees with values reported for the matrix of the (A2) and (B2) alloys.

To sum up the above-presented results, it is obvious that the coexistence of a ductile and a high-strength phase is responsible for the excellent mechanical properties.

- Influence of the microstructure on the deformation and fracture behavior

The fracture surface morphology of the compressed cylindrical rods (A2) and (B2) was carefully analyzed by scanning electron microscopy (SEM). Taken at different magnifications SEM micrographs are displayed in Figure 4.1.5. The upper images correspond to the $Fe_{81.2}Cr_{5.2}Mo_{5.2}Ga_{5.2}Si_{3.2}$ (A2) alloy; the lower present the fracture features of the deformed $Fe_{78.0}Cr_{5.2}Mo_{5.2}Ga_{5.2}Si_{6.4}$ (B2) sample. In both cases, the fracture surface appears to consist of a number of cracks and void-like "black dimples" (holes) – indicated by white arrows. However, in Figure 4.1.5c ((A2) and (B2)) the distinct differences in the morphology of the compressed rods (A2) and (B2) are visible. Considering the sample (A2), a large amount of γ-Fe dendrites on the fracture surface is observed. As denoted by white circles, some cracks propagating through the dendrites are noticed. On the other hand, when we look closer at the dendrites branches (inset in Figure 4.1.5c (A2)), one can see that their interior remains intact. Based on these findings, it is assumed that dispersed in a hard matrix, the soft Ga-rich particles of the austenitic phase act as obstacles, which hamper a flow deformation and, hence, cause pronounced strain-hardening. Regarding the BMGs, it has already been proved that introducing a ductile dendritic phase into the microstructure (composite structure formation: glass matrix with second phase precipitates) is pivotal for their plasticity [Hay00, Küh02, He03a].

The details on the morphology of the fracture surface of sample (B2) are demonstrated in Figure 4.1.5c (B2). The revealed morphology consists of two regions: I – which refers to the plane, smooth surface of the compressed rod and II – which shows the microstructure of the deformed sample. In contrast to the above-described results, the shape of the revealed phase is more spherical. The presence of cracks inside the precipitates has not been observed.
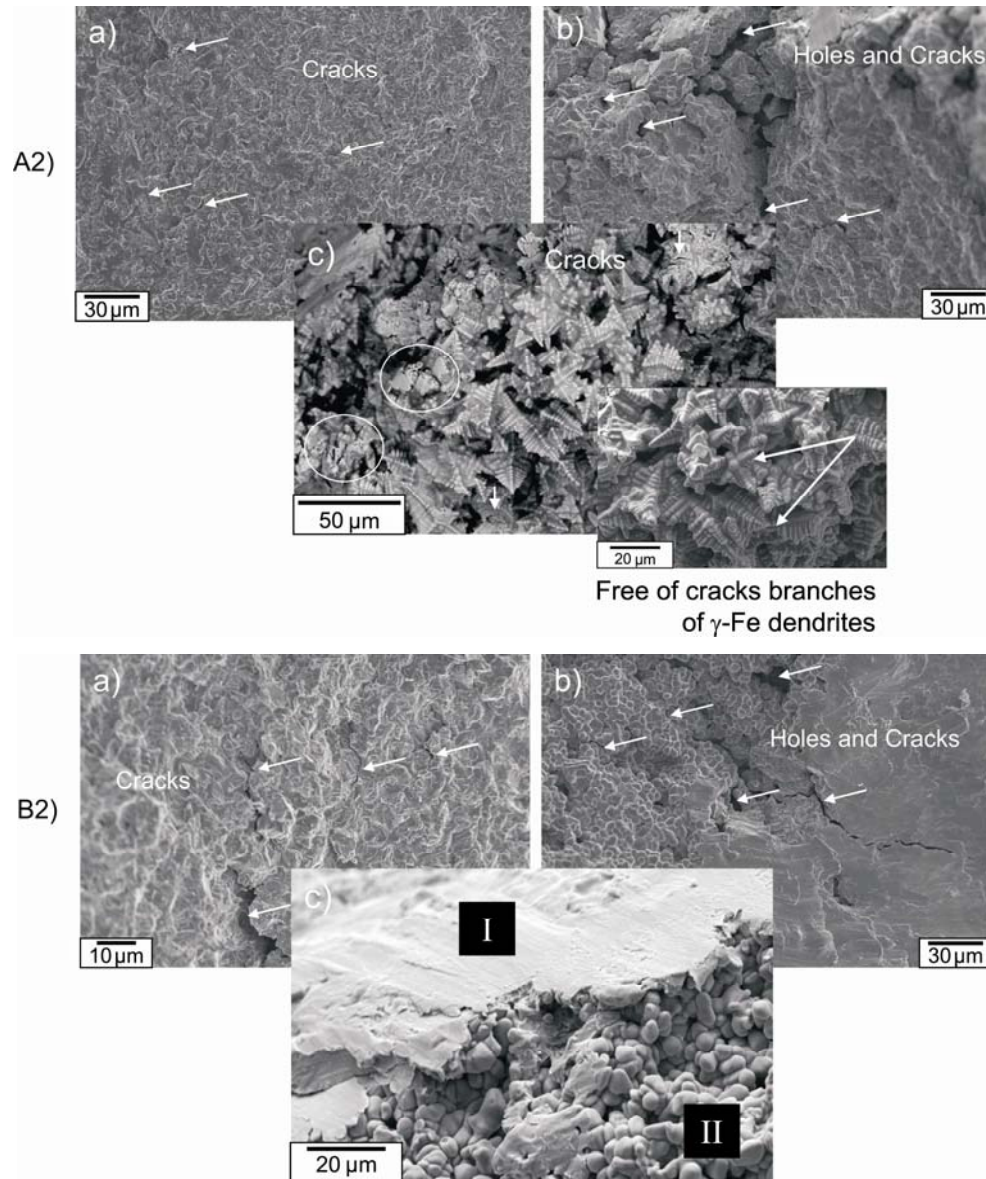
**Figure 4.1.5.** SEM (SE and BSE) micrographs showing fracture surface features of the compressed alloys: (A2) $Fe_{81.2}Cr_{5.2}Mo_{5.2}Ga_{5.2}Si_{3.2}$ – (a,b) overview of the fracture surface and (c) revealed $\gamma$-Fe dendrites. Inset: magnification of the interior of the dendrites. No cracks visible. (B2) $Fe_{78.0}Cr_{5.2}Mo_{5.2}Ga_{5.2}Si_{6.4}$ – (a,b) overview of the fracture surface with (c) regions of different morphologies. For both samples the occurrence of a high number of cracks and holes (white arrows) on the fracture morphology is observed.

As it was mentioned in a previous section the samples indicated as (A1) and (B1) with a single-phase structure (b.c.c. $\alpha$-Fe) manifest a great capacity for plastic deformation. Under an applied compressive load, such materials did not fail. Some examples of the as-deformed cylinders of the studied Fe-based materials exhibiting an extremely ductile behavior upon compression are given in Figures 4.1.6a-c. The displayed images refer to the following compositions: a) $Fe_{79.2}Cr_{10.4}Mo_{5.2}Ga_{5.2}$, b) $Fe_{79.2}Cr_{5.2}Mo_{10.4}Ga_{5.2}$ and c) $Fe_{79.2}Cr_{5.2}Mo_{5.2}Ga_{10.4}$, respectively.
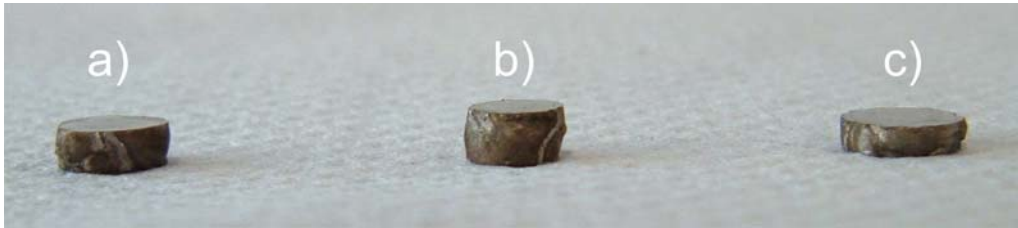


**Figure 4.1.6.** As-deformed cylindrical rods of single-phase alloys: a) $Fe_{79.2}Cr_{10.4}Mo_{5.2}Ga_{5.2}$, b) $Fe_{79.2}Cr_{5.2}Mo_{10.4}Ga_{5.2}$ and c) $Fe_{79.2}Cr_{5.2}Mo_{5.2}Ga_{10.4}$. For all compressed samples, fracture has not been achieved upon loading.

An illustration of the experimental results obtained for the studied alloy compositions (A) $Fe_{81.2}Cr_{5.2}Mo_{5.2}Ga_{5.2}Si_{3.2}$ and (B) $Fe_{78.0}Cr_{5.2}Mo_{5.2}Ga_{5.2}Si_{6.4}$ is shown in Figure 4.1.7. It was found that the microstructure as well as the resulting mechanical properties of the investigated materials very much depend on the applied casting conditions. In general, the new composite microstructure was synthesized due to carbon diffusion from the crucible into the molten alloy. The appearance of such an "impurity" in the microstructure of the examined compositions had a crucial influence on their mechanical response. Together with the structure evolution from a single-phase ((A1), (B1) – without carbon) to complex multi-phase materials ((A2), (B2) – carbon containing), an enhancement of the mechanical properties was observed. It is well known that the major application of metallic alloys as mechanically strong materials is due to their multi-phase structure. Considering the complexity of herein presented alloys (A2) and (B2) it is clear that the coexistence of ductile Ga-enriched dendrites, which restrict

the excessive deformation and, therefore, contribute to the plasticity, with a high-strength Cr- and Mo-enriched matrix leads to a material with an optimized compressive strength-strain balance.

Summarizing, the first attempts to fabricate a new Fe-based alloy with improved ductility, were based on the "*test/error method*". One of the most basic issues in materials science: controlling process conditions was neglected. Surprisingly, this mistake has enabled the discovery of novel materials with unique mechanical properties. Guided by the gained knowledge, two new nanostructured Fe-Cr-Mo-Ga-C composite materials with different carbon content were developed.

*"Anyone who has never made a mistake has never tried anything new"*

**Albert Einstein**
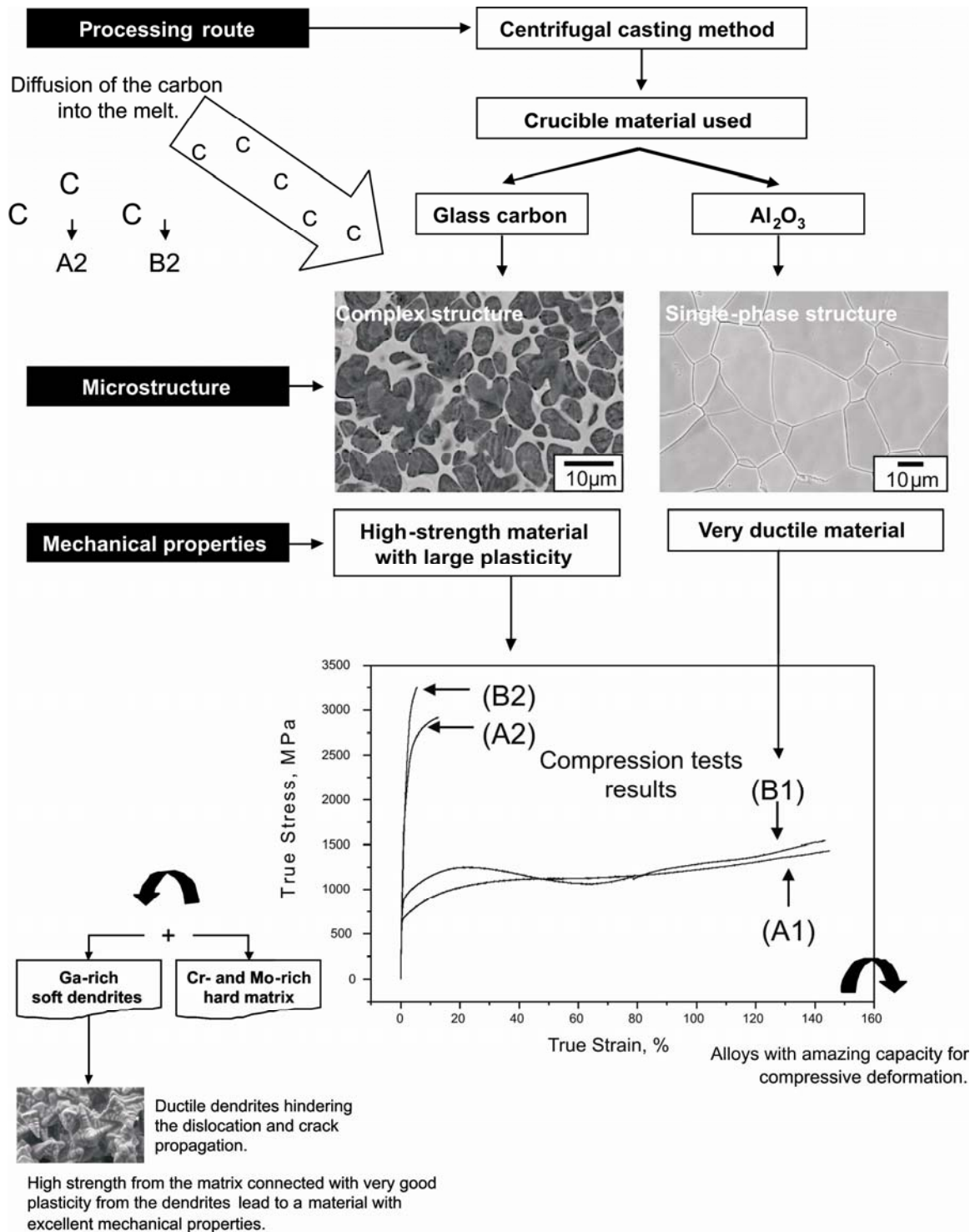
**Figure 4.1.7.** Correlation between casting conditions, microstructure and resulting mechanical properties for the investigated alloys.

## 4.2 The Fe-Cr-Mo-Ga-C alloy system – *2$^{nd}$ Step*

There were no doubts any more that in order to obtain a material with a desired complex microstructure the chemistry of our Fe-based system derived from a monolithic bulk metallic glass must be further modified. It was clear that carbon additions play a significant role in the alloy design strategy. According to this scenario, two C-containing alloy compositions $(Fe_{84.4}Cr_{5.2}Mo_{5.2}Ga_{5.2})_{91}C_9$ and $(Fe_{84.4}Cr_{5.2}Mo_{5.2}Ga_{5.2})_{83}C_{17}$ were prepared. The selected C concentrations (9 and 17 at.%) conform to contents estimated for the studied (A2) and (B2) specimens.

- Phase identification and microstructure observations

Figures 4.2.1a and b present XRD patterns obtained from the transverse cross section of the as-cast alloys (black curves) (C) $(Fe_{84.4}Cr_{5.2}Mo_{5.2}Ga_{5.2})_{91}C_9$ and (D) $(Fe_{84.4}Cr_{5.2}Mo_{5.2}Ga_{5.2})_{83}C_{17}$. The microstructure of alloy (C) is mainly composed of a f.c.c. austenitic phase (γ-Fe) and a b.c.t. martensitic phase. Besides the peaks of the austenite and martensite weak additional reflections corresponding to hexagonal (hP3) chromium/molybdenum carbide $(Cr,Mo)_2C$ are visible. It should be noted that the identified phases (austenite and martensite) are in good agreement with those observed for the as-cast $Fe_{78.0}Cr_{5.2}Mo_{5.2}Ga_{5.2}Si_{6.4}$ rod-shaped specimen (B2) with "extra" C addition (7 at.%). Furthermore, based on the XRD patterns, the volume fraction of the individual compounds was determined by a multi-phase Rietveld analysis [You93], assuming an identical chemistry of the particular structures. This gives 41 vol.% austenitic, 42 vol.% martensitic and 17 vol.% hexagonal carbide phase, respectively. Also for sample (D) the position of the maxima of the main diffraction peaks can be assigned to a f.c.c. austenitic γ-Fe phase. Contrary to alloy (C), further reflections indicate the formation of $Fe_3C$ (cementite) with orthorhombic crystal structure. There is no evidence of any other phases in this alloy. Comparing the XRD analysis performed for the $Fe_{81.2}Cr_{5.2}Mo_{5.2}Ga_{5.2}Si_{3.2}$ (A2) alloy (with "addition" of 14.2 at.% C), the formation of a f.c.c. γ-Fe phase was affirmed. However, the further peaks indexed in the XRD pattern (corresponding either to $Mo_2C$ or $MoSi_2$) do not match those of alloy (D) ($Fe_3C$ phase). Obviously, the revealed differences in the phase formation between samples (D) and (A2) are associated with the variation in

their overall composition. Additionally, volume fractions of 25 vol.% $Fe_3C$ and 75 vol.% f.c.c. γ-Fe were calculated by the Rietveld analysis for specimen (D).



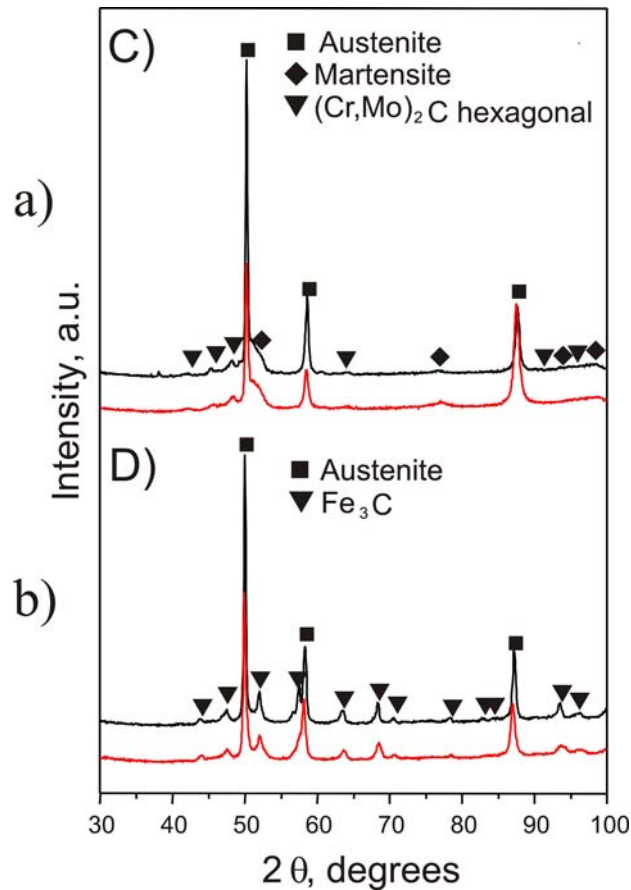**Figure 4.2.1.** XRD patterns of the as-cast (black curves) and deformed (red curves) cylindrical rods of the $(Fe_{84.4}Cr_{5.2}Mo_{5.2}Ga_{5.2})_{91}C_9$ (C) and $(Fe_{84.4}Cr_{5.2}Mo_{5.2}Ga_{5.2})_{83}C_{17}$ (D) alloys.

The complex microstructure of alloys (C) and (D) is shown in the SEM images in Figures 4.2.2a-d. Considering alloy (C), the coexistence of dark (austenite) and bright (matrix composed of martensite and carbide compound) phases is observed. Indeed, the primary impression of image a) which might appear is that such an alloy consists of only two phases with clearly different volume fractions. However, a higher magnification SEM micrograph (SE-mode) c) corroborates the occurrence of a third compound, which is set in the microstructure of the matrix. Electron diffraction patterns (not presented

here) obtained from the two main phases (austenite and martensite) support the f.c.c. and b.c.t. structure, respectively.

The insight into the structure of the as-cast sample (D) (see Figure 4.2.2d) provides detailed information on distribution, dimension and morphology of the individual compounds. The micron-sized $\gamma$-Fe particles are embedded in a mixture of $\gamma$-Fe and $Fe_3C$ phases. The matrix possesses a typical eutectic morphology. The small precipitates of the iron carbide (cementite) are placed at the boundaries of the austenite.
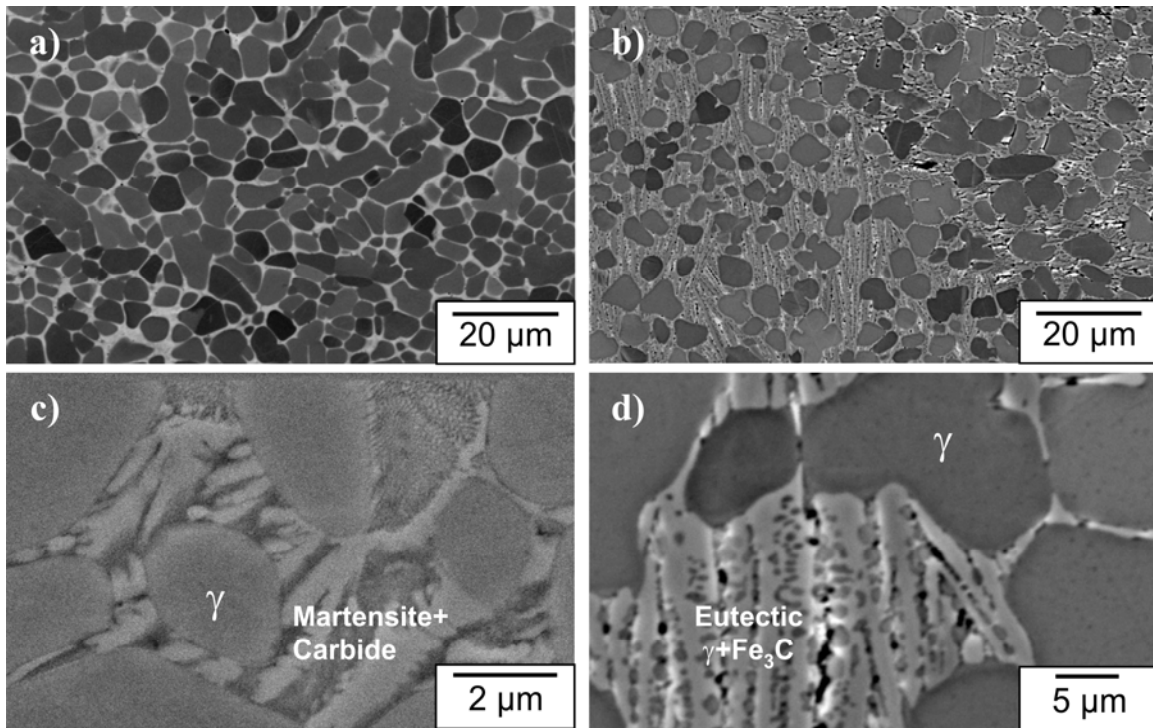


**Figure 4.2.2.**     SEM images of the as-cast alloys $(Fe_{84.4}Cr_{5.2}Mo_{5.2}Ga_{5.2})_{91}C_9$ (a,c) and $(Fe_{84.4}Cr_{5.2}Mo_{5.2}Ga_{5.2})_{83}C_{17}$ (b,d). The SEM (BSE mode) images (a,b) show the homogeneous distribution, the size and the morphology of the f.c.c. $\gamma$-Fe phase (dark gray phase). The SEM images (c,d) reveal the interdendritic phases: c) (SE-mode) the martensitic phase with $M_2C$ carbides and d) (BSE-mode) the interdendritic eutectic phases, $\gamma$-Fe and $Fe_3C$.

For both alloys, the dominant constituent f.c.c. $\gamma$-Fe phase exhibits a size ranging from 2 to 10 µm. Clearly, the dendritic precipitates become finer towards the edge of the cylinders. The finer microstructure, as revealed for the outermost regions, results from the higher heat transfer upon solidification – it is well known that the first contact of the melt with the Cu wall of the mold leads to higher cooling rates. The evolution of the microstructure of the examined samples (C) and (D) is illustrated below - Figures 4.2.3a and b.
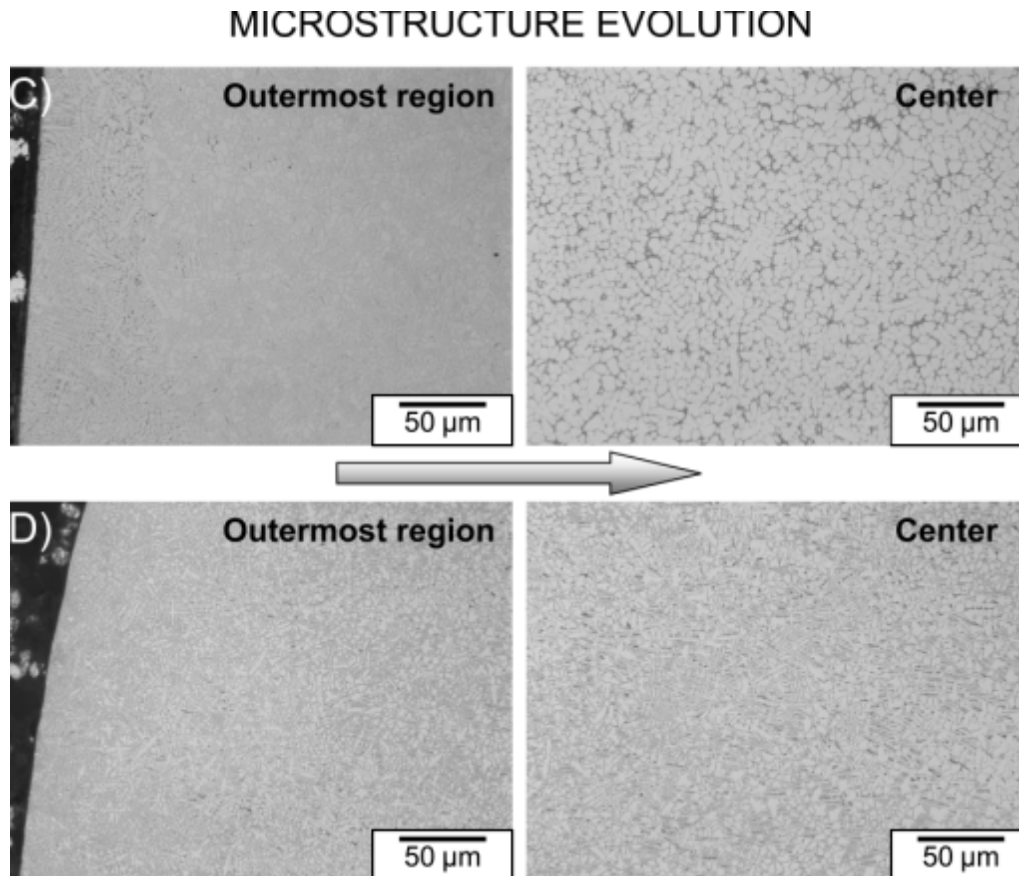


**Figure 4.2.3.** Optical micrographs of specimens (C) (images above) and (D) (images below) showing the changes in the structure morphology towards the center. For sample (C) the shape and the size of the f.c.c. dendritic phase in the center area become more spherical and bigger compared to the edge. Also alloy (D) manifests a slight coarsening of the microstructure towards the center.

The average composition of the revealed phases was estimated by energy dispersive X-ray spectroscopy (EDX). It has been found that the dendritic phase is enriched in Fe and Ga with respect to the nominal composition. Obviously, the dendritic phase is a γ-Fe(C,Ga) solid solution, whereas C stabilizes the f.c.c. structure of iron [Got07]. Both interdendritic phases (the martensite and naturally the carbides) show significantly higher Cr and Mo concentrations in comparison to the overall alloy composition. The average composition of the examined as-cast (C) and (D) rods determined from EDX and WDX analyses is summarized in Table 4.2.1.

**Table 4.2.1.** EDX and WDX analysis results of the different phases compared to the overall composition of alloys (C) and (D).

| | Alloying components, [at.%] | | | | |
|---|---|---|---|---|---|
| | Fe | Cr | Mo | Ga | C |
| Nominal composition: alloy (C) | **76.9** | **4.7** | **4.7** | **4.7** | **9.0** |
| γ−Austenite | 78.6 | 3.3. | 4.0 | 8.6 | 5.5 |
| Martensite | 77.7 | 8.6 | 6.6 | 1.6 | 5.5 |
| Carbide (Cr,Mo)$_2$C | 47.6 | 9.8 | 16.8 | 1.8 | 24.0 |
| Nominal composition: alloy (D) | **70.1** | **4.3** | **4.3** | **4.3** | **17.0** |
| γ−Austenite | 82.5 | 2.6 | 3.1 | 7.2 | 4.6 |
| Cementite Fe(Cr,Mo)$_3$C | 54.8 | 7.1 | 7.9 | 0.1 | 30.1 |

The final structural investigations were done by means of TEM. This technique was utilized to unequivocally resolve fine interdendritic phases dispersed in the matrix. Bright-field TEM images (Figures 4.2.4a and b) present the characteristics of the interdendritic phases of the studied Fe-based composites. For composition (C) (Figure 4.2.4a), the carbides are beads-shaped and placed at the interfaces of austenite and martensite. The size of the carbide precipitates is about 20 nm. The formation of the martensite is associated

with an increase of volume, due to the trapping of carbon atoms in one set of octahedral interstitial sites of the body-centered structure [Mas92]. Hence, the martensite is highly distorted and a high strain energy is connected with the martensitic structure. Also the interdendritic eutectic phases (austenite+cementite) of composition (D) show significant straining in the TEM image (Figure 4.2.4b) (see the white, grey and black bending lines caused by lattice distortion). The principal reason for the distortions is, similar to alloy (C), the lattice supersaturation with carbon atoms on interstitial sites.
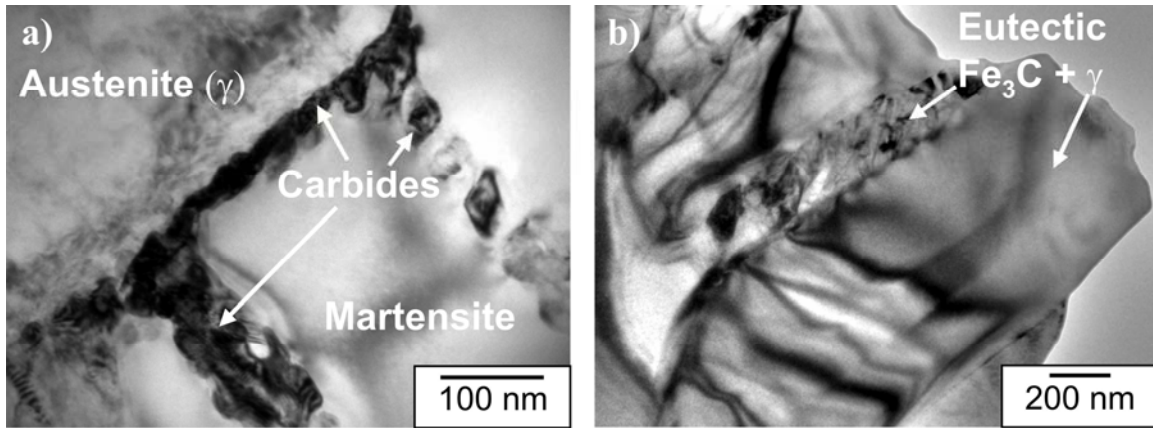


**Figure 4.2.4.**   Bright-field TEM images of as-cast alloys $(Fe_{84.4}Cr_{5.2}Mo_{5.2}Ga_{5.2})_{91}C_9$ a) and $(Fe_{84.4}Cr_{5.2}Mo_{5.2}Ga_{5.2})_{83}C_{17}$ b). For both alloys the high distortion of the interdendritic phases is shown, mainly caused by lattice supersaturation with carbon atoms.

- Solidification behavior of $(Fe_{84.4}Cr_{5.2}Mo_{5.2}Ga_{5.2})_{100-x}C_x$ alloys (x = 9,17 at.%)

A key challenge of this study was to understand the solidification behavior of the *in-situ* formed Fe-based composites (def. *in-situ* composite – composite fabricated directly from the melt by appropriate solidification or by a secondary treatment of amorphous precursors [Eck07b]). The possible explanation of the phase formation observed for the Fe-Cr-Mo-Ga-C alloy system is described below.

The three phases present in the $(Fe_{84.4}Cr_{5.2}Mo_{5.2}Ga_{5.2})_{91}C_9$ (C) alloy (austenite, martensite, carbides) are the typical phases existing in steels. Therefore, to consider the solidification mode of alloy (C), the Fe-C phase diagram (see chapter 3 **"Materials –**

**processing and characterization"**) and, additionally, the non-equilibrium diffusionless transformation mechanism of martensite, were employed as a tool to try to understand the phase formation of the $(Fe_{84.4}Cr_{5.2}Mo_{5.2}Ga_{5.2})_{91}C_9$ alloy. However, such phase configuration (round-shaped austenite in coexistence with martensite and relatively high amounts of carbides already in the not tempered state) is atypical for conventional steels. Usually, lath or plate martensite transforms from the parent austenite and, in case of a not complete martensitic transformation, residual austenite is retained between the laths or plates of martensite. Furthermore, the formation of carbides in Cr- and Mo-containing steels is generally induced by tempering at 500 to 700 °C, i.e. they do not form during solidification.

The potential stepwise phase formation during the solidification of alloy (C) is schematically displayed in Figure 4.2.5.
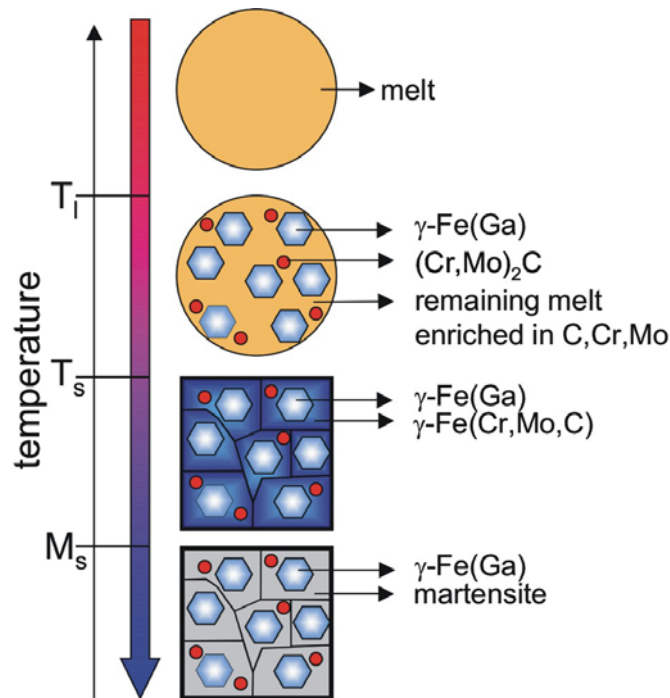


**Figure 4.2.5.** Schematic illustration of the phase transformation steps at specific temperatures (Liquidus temperature $T_l$, Solidus temperature $T_s$, starting temperature of martensitic transformation $M_s$) of the alloy $(Fe_{84.4}Cr_{5.2}Mo_{5.2}Ga_{5.2})_{91}C_9$ (C) during copper mold casting.

The primary formed austenite shows obviously a significantly different composition than the parent austenite, which shears into martensite by an athermal transformation process. The first phase, which precipitates from the melt is a f.c.c. phase with low C content, i.e. the remaining melt will be continuously enriched in C. Ga, Cr and Mo are substitutional alloying elements to Fe, but only Ga is completely dissolved in the primary γ-Fe solid solution. This is because Cr and Mo are very strong carbide forming elements whereas Ga obviously does not form phases with C (a Ga-C phase diagram is not available). It can be assumed that the formation of the γ-Fe(C,Ga) solid solution occurs simultaneously to the carbide formation. $(Cr,Mo)_2C$ with hexagonal structure was mainly found at the grain boundaries of the martensite. The strong affinity between Cr-C and Mo-C is certainly the reason that only the interdendritic phases (martensite and carbides) contain these elements in higher concentrations.

With progressing solidification the γ-Fe solid solution becomes more and more enriched in Cr and Mo besides the carbide formation. Thus on cooling from temperatures where the austenite is no longer stable and because Cr and Mo tend to stabilize the b.c.c. structure of iron, the fraction of the austenite that is locally enriched in Cr and Mo must transform into another phase. A diffusion-controlled mechanism is excluded by the rapid cooling. Therefore, these parts of the austenite transform into martensite, which is supersaturated in carbon.

The phases revealed by X-ray diffraction and electron microscopy for the $(Fe_{84.4}Cr_{5.2}Mo_{5.2}Ga_{5.2})_{83}C_{17}$ alloy (austenite, as well as interdendritic eutectic phases of austenite and cementite) are the typical phases of cast iron. The formation of cementite is, in contrast to martensite formation, diffusion-controlled and accompanied by a rearrangement of the iron atoms from the f.c.c. structure to the orthorhombic structure of the cementite. Similar to the observations made for alloy (C) the austenitic phase is enriched in Fe and Ga and depleted in Cr, Mo and C in comparison to the nominal alloy composition. The last three elements are found in much higher concentrations in the $(Fe,Cr,Mo)_3C$ phase (cementite). The solidification behavior and, hence, the microstructure of alloy (D) differ from those of alloy (C), due to its higher carbon content (17 at.%). The composition is near to the eutectic point of the Fe-C phase diagram, where austenite and cementite are in equilibrium. Consequently, the alloy solidifies at a lower temperature

compared to alloy (C) and the melting interval ($T_l$ to $T_s$) is significantly smaller. Obviously, these characteristics prevent the precipitation of high melting (Cr,Mo)-carbides. Primary austenite (Ga-rich γ-Fe solid solution) nucleates and grows into a dendritic array during the melting interval. When the eutectic concentration is reached, the excess C precipitates as the metastable $(Fe,Cr,Mo)_3C$ phase together with γ-Fe by an eutectic reaction.

- Thermal stability of the martensitic phase

In the equilibrium phase diagram of the iron-carbon system there is no martensitic phase, due to its metastable nature [Haa05]. According to the thermodynamic criterions, each system tends to minimize its internal energy (Gibbs free energy ($G$)), in order to reach equilibrium [Bok05]. Obviously, the martensitic phase due to its metastability will transform into other phases (i.e. transformations observed upon heat treatment – tempering process) with lower Gibbs free energy. However, to activate such a transformation, the activation energy - defined as the minimum energy necessary for a specific chemical reaction to occur - must be overcome [Bok05]. In other words, a thermal impulse like heating is required. Since chemical processes accelerate at higher temperature, the martensite presence in the microstructure of the studied alloy (C) can be easily destroyed by the application of heat. In order to verify such an assumption systematic investigations on the thermal stability as well as microstructure evolution of the $(Fe_{84.4}Cr_{5.2}Mo_{5.2}Ga_{5.2})_{91}C_9$ specimen were carried out.

Figure 4.2.6 exhibits a DSC scan recorded using a constant heating rate of $20\,Kmin^{-1}$ for a $(Fe_{84.4}Cr_{5.2}Mo_{5.2}Ga_{5.2})_{91}C_9$ as-cast cylinder. Starting from room temperature (RT), the sample was heated up 1173 K (below the melting point $T_m \approx 1400$ K). The obtained DSC scan reveals the occurrence of several calorimetric peaks. Their presence clearly indicates that the microstructure of the investigated alloy (C) undergoes transformations (solid state phase transitions). In a first stage (for temperatures ranging from 955 to 1035 K) two distinctive exothermic events take place. Considering the BMG-forming systems, such exothermic reactions observed in a DSC curve originate from crystallization processes. With progressing heating the driving force for crystallization (approximated by the Gibbs free energy difference ΔG between the

supercooled liquid and the crystal [Bus07]) increases and an amorphous state cannot be longer retained. Consequently, the glassy structure transforms into a crystalline phase.
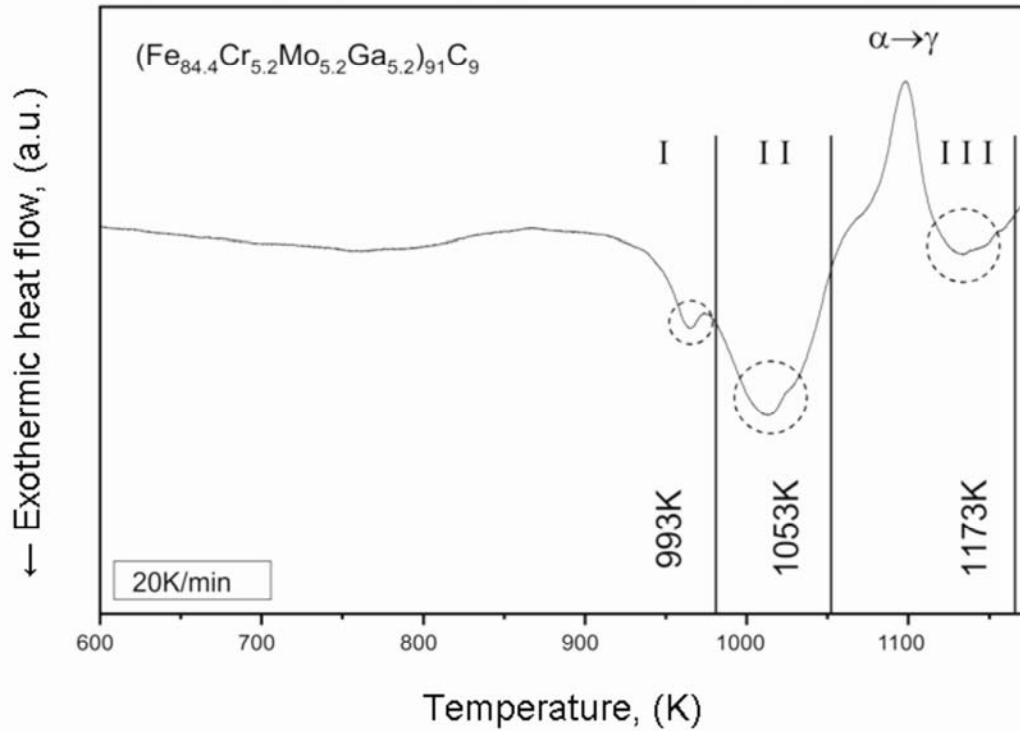


**Figure 4.2.6.**   DSC heating plot of the crystalline $(Fe_{84.4}Cr_{5.2}Mo_{5.2}Ga_{5.2})_{91}C_9$ rod-shaped specimen showing two exothermic peaks (indexed as I and II) followed by an endothermic phase transition $\alpha\rightarrow\gamma$ at T ≈ 1100 K and an exothermic event (III). The three lines are related to the temperatures of a heat treatment (993, 1053 and 1173 K). In addition, all analyzed exothermic events are marked by black dashed-circles.

In order to explore the origins responsible for the structural changes observed for the fully crystalline alloy (C), the heat treatment up to the completion of the first ($T_1 = 993$ K) and second ($T_2 = 1053$ K) exothermic peak (indicated in Figure 4.2.6 as stage I and stage II, respectively) with subsequent cooling to ambient temperature at 20 Kmin$^{-1}$ was performed. Further on, by X-ray diffraction as well as scanning electron

microscopy, the variations in phase formation between the reference as-cast state and the as-annealed states (I and II) were analyzed.

Special attention has been devoted to the endothermic reaction (at T ≈ 1100 K) which presumably corresponds to the α (b.c.t. martensite)→γ (f.c.c. austenite) phase transition. To confirm this argument, an additional DSC experiment was conducted. The scanning was running up to 1173 K – denoted as stage III (annealing above the endothermic heat flow event followed by an exothermic peak). To obtain detailed information regarding the structural evolution, which declines during the last stage, the resulting microstructure was then examined by means of XRD and SEM.

An overview of the microstructure revealed after the first stage of annealing with the corresponding diffraction pattern is displayed in Figure 4.2.7a (the XRD pattern of the as-cast state in shown in Figure 4.2.1a). Compared to the as-cast rod, slight dissimilarities regarding the occurrence and the intensity of the peaks are observable. The XRD patterns demonstrated in Figures 4.2.1a and 4.2.7a and b show a progressive increase in the intensity of the peaks corresponding to a b.c.t. martensite. Accordingly, it is concluded that the second exothermic event (the b.c.t. α-Fe phase becomes more prominent) can be linked to the martensitic transformation. Unfortunately, the reasons responsible for the γ→α transition declining during the heating process of the studied $(Fe_{84.4}Cr_{5.2}Mo_{5.2}Ga_{5.2})_{91}C_9$ sample are not well understood yet. One of the developed theories implies that, due to the extremely high cooling rates (specific cooling conditions applied), not the whole γ-Fe(Cr,Mo,C) solid solution (see Figure 4.2.5) is able to transform into the b.c.t. martensitic phase. However, it is well known that the transition between these two structures (f.c.c.→b.c.c.) requires only a small thermal activation energy because it occurs displacively or martensitically by the subtle but rapid rearrangement of atomic positions [Bok05]. Therefore, when the energy necessary for terminating such a process is provided (i.e. while heating), the residual austenite tends to transform into a martensitic phase. Taking into account these considerations, the proposed theory seems to be probable.
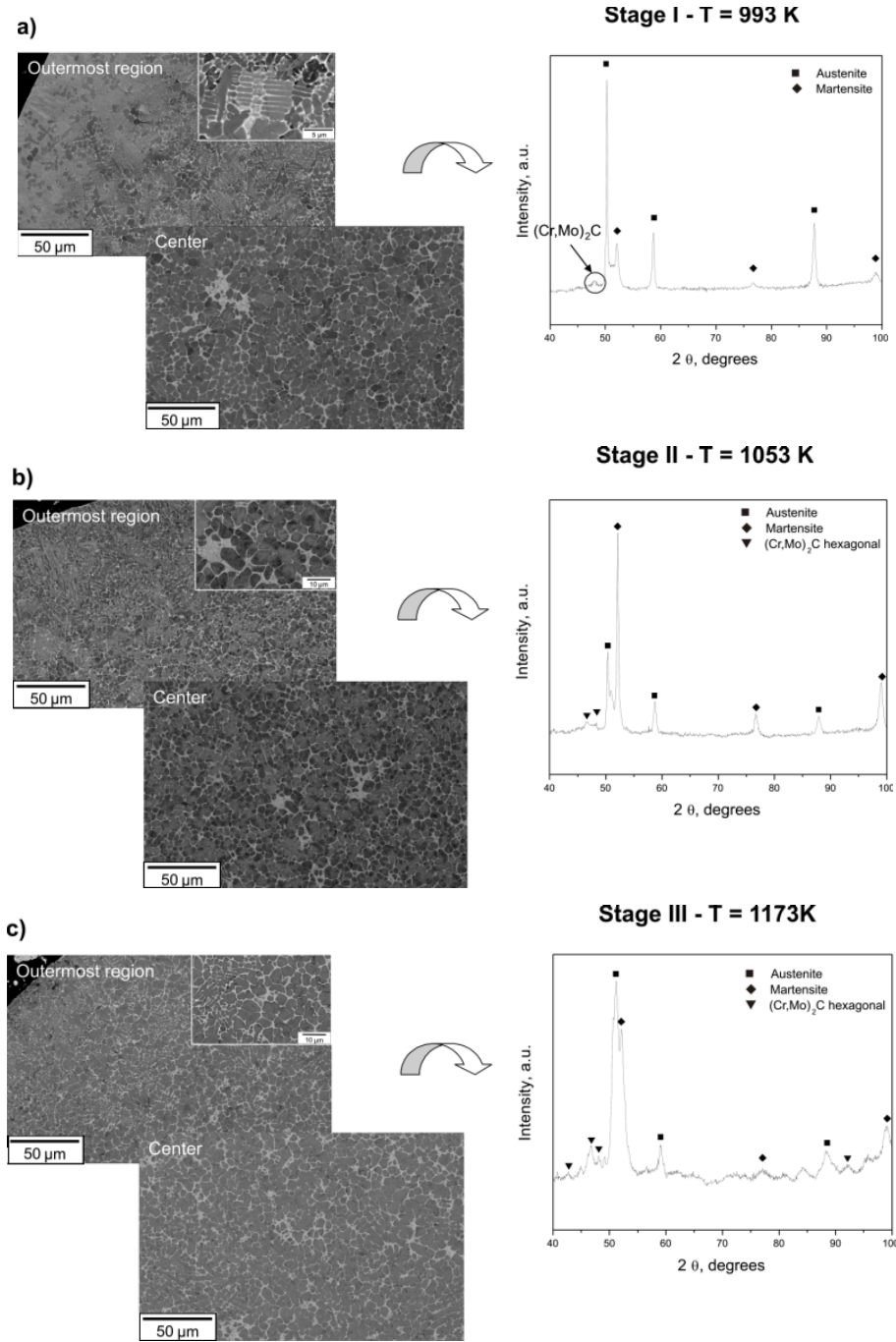
**EVOLUTION of MICROSTRUCTURE UPON ANNEALING**



**Figure 4.2.7.** SEM backscattered electron images showing the microstructure of the $(Fe_{84.4}Cr_{5.2}Mo_{5.2}Ga_{5.2})_{91}C_9$ alloy, revealed after each stage of annealing with corresponding diffraction patterns. Insets in micrographs – overview of the structure taken at higher magnification.

The phase analysis results obtained for alloy (C) after the third stage of the heat treatment are documented in Figure 4.2.7c. In addition, the SEM micrographs of the developed microstructure are presented. The obtained XRD pattern supports the assumptions regarding the identification of the endothermic signal visible in the DSC trace. As a consequence of the $\alpha \rightarrow \gamma$ phase transition at $T \approx 1100$ K, the intensity of the first reflection corresponding to b.c.t. martensite decreases. The f.c.c. austenite becomes the dominant phase.

The extensive studies on the microstructure evolution of the investigated as-annealed $(Fe_{84.4}Cr_{5.2}Mo_{5.2}Ga_{5.2})_{91}C_9$ alloy (see SEM images displayed in Figure 4.2.7) did not reveal essential dissimilarities in the morphology of the individual compounds. The structure in its appearance does not sustain any drastic changes. Concerning the precipitates of the $\gamma$-Fe phase: their shape, size and distribution, compared to the as-cast state remain unchanged. All annealed stages exhibit a slightly finer microstructure in the edge of the sample cross-section. Moreover, there are small variations in the shape of the austenitic precipitates towards the center. The mixture of dendritic, spherical, as well as elongated $\gamma$-Fe particles (outermost region) transforms into a microstructure composed mainly of round-shaped $\gamma$-Fe precipitates distributed in a complex matrix (center). These observations are in good agreement with those obtained for the examined as-prepared Fe-based rod.

Although there are no significant differences in the appearance of the microstructures of all investigated states, according to the recorded DSC plot and the X-ray diffraction analysis, it is evident that the $(Fe_{84.4}Cr_{5.2}Mo_{5.2}Ga_{5.2})_{91}C_9$ alloy undergoes phase transformations (martensitic transition followed by reverse reaction $\alpha \rightarrow \gamma$) upon the heating process. However, in order to provide accurate information on the microstructure characterization, further experiments are required (in-situ XRD, volume fraction estimation – Rietveld method, TEM observation of the fine matrix phase – future work).

- Effect of carbon on the mechanical properties

In this section the plastic deformation of the Fe-Cr-Mo-Ga-C alloy system will be discussed. Since it was recognized that a carbon addition is highly requisite for a composite structure formation, which manifests itself both in high strength and in large

plasticity (see alloys (A2) and (B2)), detailed studies regarding the carbon influence on the mechanical properties of the investigated Fe-based compositions were performed.

Figure 4.2.8 exhibits the room temperature true stress-strain curves for the as-cast alloys (C) $(Fe_{84.4}Cr_{5.2}Mo_{5.2}Ga_{5.2})_{91}C_9$ and (D) $(Fe_{84.4}Cr_{5.2}Mo_{5.2}Ga_{5.2})_{83}C_{17}$ under compression. Additionally, the engineering stress-strain plots are displayed in the inset of Figure 4.2.8.
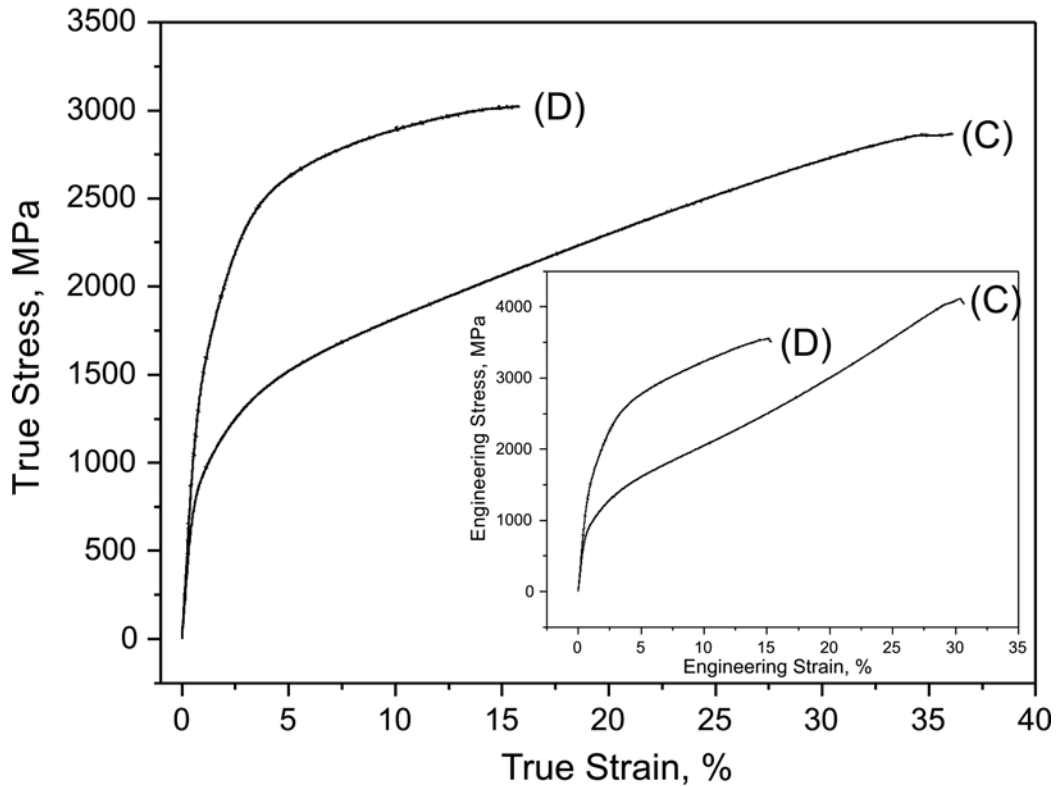


**Figure 4.2.8.** Compressive true stress-strain curves of alloys (C) $(Fe_{84.4}Cr_{5.2}Mo_{5.2}Ga_{5.2})_{91}C_9$ and (D) $(Fe_{84.4}Cr_{5.2}Mo_{5.2}Ga_{5.2})_{83}C_{17}$, illustrating the strong influence of the microstructure on the mechanical behavior. The inset shows the engineering stress-strain curves of specimens (C) and (D).

The mechanical characteristics of the deformed rods are summarized in Table 4.2.2. Moreover, to highlight their outstanding mechanical properties, the available data for the selected Fe-based fully glassy materials are given for comparison.

**Table 4.2.2.** Engineering and true values of room temperature compression tests for (C) $(Fe_{84.4}Cr_{5.2}Mo_{5.2}Ga_{5.2})_{91}C_9$ and (D) $(Fe_{84.4}Cr_{5.2}Mo_{5.2}Ga_{5.2})_{83}C_{17}$: Young's modulus $E$, yield stress $\sigma_y$, yield strain $\varepsilon_y$, fracture stress $\sigma_f$, and fracture strain $\varepsilon_f$. In addition, the mechanical properties of the $Fe_{65.5}Cr_4Mo_4Ga_4P_{12}C_5B_{5.5}$ (BMG1) – starting composition; $Fe_{77}Ga_3P_{9.5}C_4B_4Si_{2.5}$ (BMG2) and $(Fe_{0.75}B_{0.15}Si_{0.1})_{96}Nb_4$ (BMG3) glass-forming alloy systems are given for comparison.

| alloy/ | true values | | | | | engineering values | |
|---|---|---|---|---|---|---|---|
| sample dimensions | $E$ | $\sigma_y$ | $\varepsilon_y$ | $\sigma_f$ | $\varepsilon_f$ | $\sigma_f$ | $\varepsilon_f$ |
| | [GPa] | [MPa] | [%] | [MPa] | [%] | [MPa] | [%] |
| (C) / Ø 3 mm | 162 | 833 | 0.7 | 2868 | 36.2 | 4116 | 30.4 |
| (D) / Ø 3 mm | 208 | 1410 | 0.9 | 3026 | 16.4 | 3561 | 15.2 |
| (BMG1) Ø 2.5 mm [Sto05b] | 170 | 3270 | 1.91 | 3270 | 2.03 | | |
| (BMG2) Ø 2.0 mm [Ino03b] | 182 | 2980 | 1.9 | 3160 | 2.2 | | |
| (BMG3) Ø 1.5 mm [Ino03b] | 175 | 3165 | 1.8 | 3250 | 2.2 | | |

A careful analysis of the above presented stress-strain curves reveals that the most distinctive and remarkable mechanical features are on one hand the large increase in ductility to $\varepsilon_{f(true)} = 36\%$ for the sample with lower carbon content (C) and $\varepsilon_{f(true)} = 16\%$ for the sample with higher carbon content (D) without any reduction of the fracture strength compared to the reference $Fe_{65.5}Cr_4Mo_4Ga_4P_{12}C_5B_{5.5}$ bulk metallic glass. The fracture compression stress of alloy (D) ($\sigma_f = 3.03$ GPa) is congenial with the values

reported for monolithic Fe-based BMGs: BMG1 ($\sigma_f$ = 3.27 GPa), BMG2 ($\sigma_f$ = 3.16 GPa) and BMG3 ($\sigma_f$ = 3.25 GPa). On the other hand, the yield strength decreases significantly: from the BMGs ($\sigma_{yBMG1}$ = 3.27 GPa, $\sigma_{yBMG3}$ = 3.17 GPa and $\sigma_{yBMG2}$ = 2.98 GPa) to alloy (D) ($\sigma_y$ = 1.41 GPa) and to alloy (C) ($\sigma_y$ = 0.83 GPa). Obviously, the high values obtained for maximum strength for (C) and (D) are connected with a pronounced strain hardening behavior. Especially for specimen (C) (with lower carbon concentration) there is a large increase of the flow stress of about 2.0 GPa (from 0.83 to 2.87 GPa).

Based on the promising results obtained for the crystalline $(Fe_{84.4}Cr_{5.2}Mo_{5.2}Ga_{5.2})_{91}C_9$ and $(Fe_{84.4}Cr_{5.2}Mo_{5.2}Ga_{5.2})_{83}C_{17}$ materials, recently Kühn *et al.* [Küh07] developed an interesting concept of manufacturing a steel composition $Fe_{84.3}Cr_{4.3}Mo_{4.6}V_{2.2}C_{4.6}$ by employing preparation conditions typically used for fabricating glassy alloys (i.e. relatively high cooling rate and pure chemical components). As a consequence, the formation of nonequilibrium phases, such as martensite and complex carbide structures already in the as-cast state was observed [Küh07]. The combination of the high strength compounds results in an excellent mechanical behavior of the examined $Fe_{84.3}Cr_{4.3}Mo_{4.6}V_{2.2}C_{4.6}$ steel. The reported value of the engineering compression strength exceeds 4.0 GPa, whereas the corresponding fracture strain is about 12%.

It is well known that martensite, carbides and cementite are the sources of hardness and high strength in steels, but they are also responsible for the high brittleness of the material [Got07]. The reasons are manifold, e.g. the special lattice structure, generation of internal stress, solid solution strengthening, particle strengthening, etc. In order to discern the mechanical properties of the individual compounds as well as the mixed phases, microhardness experiments were additionally carried out. The average value for the Mo- and Cr-rich phases (martensite+carbide for alloy (C)) is 5.0 GPa and for the eutectic phases (austenite+cementite for alloy (D)) is 7.3 GPa, respectively. Meanwhile, the microhardness of the Ga-rich dendritic austenite was determined to be 2.9 GPa for alloy (C) and 3.3 GPa for alloy (D), respectively. The value of 7.3 GPa (austenite+cementite) is similar to the high microhardness (8 GPa) measured for the glassy $Fe_{65.5}Cr_4Mo_4Ga_4P_{12}C_5B_{5.5}$ BMG [Sto05a, Sto05b].

Based on the above-described findings, it is argued that the outstanding mechanical behavior of the as-cast samples (C) and (D), i.e. the very strong work hardening in the case of the alloy with 9 at.% carbon and the high yield and fracture strength coupled with the good ductility of the alloy with 17 at.% carbon, can be attributed to the strong and effective interactions between the soft and ductile (austenite) and hard and brittle (martensite, cementite, carbides) components of the microstructure, where the microstructure includes not only the crystallographic lattice of the present phases but also the content of point defects, dislocation density and spatial distribution, grain and twin boundaries [Pic92]. The combination of phases with significantly different hardness values clearly indicates that the presented alloys herein can be considered as composite materials, which mostly are developed to show both high strength and good ductility.

- Fracture surface analysis

Considering the fact that the martensitic transformation can also be induced by applying external stress at temperatures above $M_s$ [Pic92], detailed observations on the microstructure of as-deformed samples were performed. It was expected that the investigated alloys subjected to compressive deformation would undergo a $\gamma$ (austenite)$\rightarrow\alpha$ (martensite) transition. In order to verify such assumptions XRD measurements were performed. The XRD results obtained for the deformed compression test samples (C) and (D) (red curves in Figures 4.2.1a and b) clearly reveal a significant increase of defects compared to the as-prepared state as well as a texture formation, especially in the austenitic phase. But there is no phase transformation of the austenite into martensite, which could easily explain the large amount of work hardening. Obviously, the mechanical behavior of the presented alloys is rather governed by conventional deformation mechanisms, such as the development of a texture on one hand and a dislocation accumulation and motion as well as an obstruction of the dislocation movement by grain boundaries, obstacles, etc., on the other hand.

Because of the complexity of the structures of the studied Fe-based alloys, variations in the fracture behavior between the particular phases were investigated.
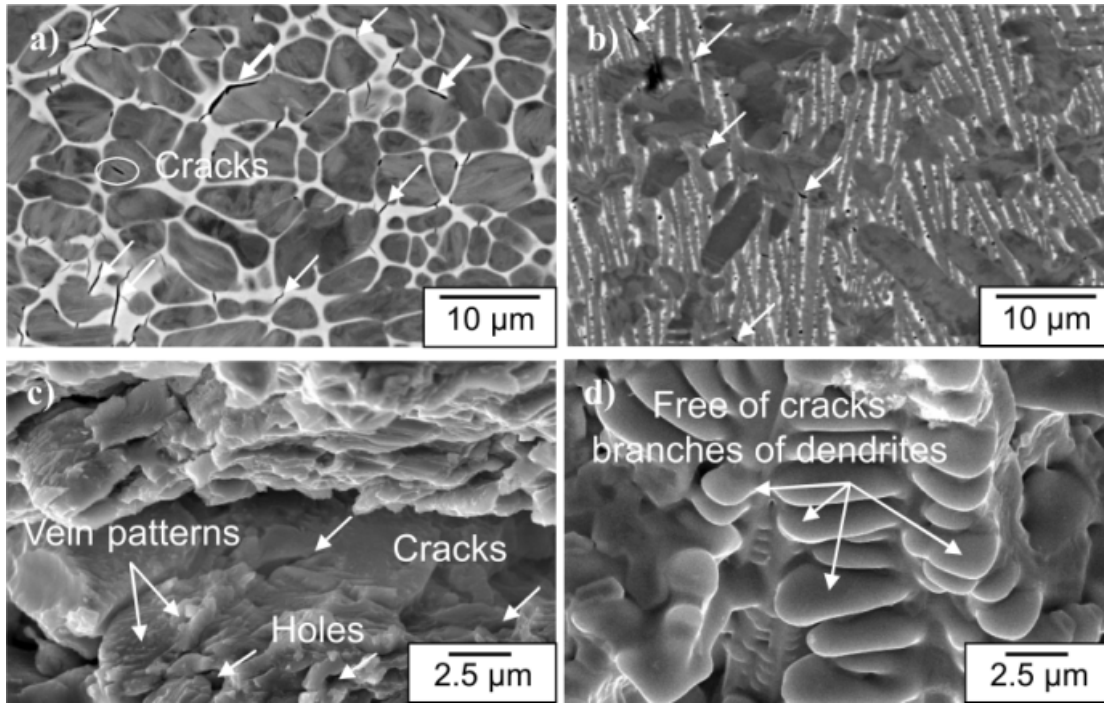
**Figure 4.2.9.** Observations on the deformed cross-section and fracture surface. SEM backscattered electron images of the cross-section (a,b) and SEM secondary electron images of the fracture surface (c,d) of alloys $(Fe_{84.4}Cr_{5.2}Mo_{5.2}Ga_{5.2})_{91}C_9$ (a,c) and $(Fe_{84.4}Cr_{5.2}Mo_{5.2}Ga_{5.2})_{83}C_{17}$ (b,d). Image a) presents the propagation paths of the cracks formed under compressive load. The deformation proceeds along the interdendritic phase either in an intergranular manner (small white arrows) or in a transgranular manner (large white arrows). Only a single crack cutting through the ductile dendritic phase was recognized (denoted by a white circle). Clearly, crack propagation is obstructed by dendrites. Micrographs c) and d) show the fracture features for samples (C) and (D). The occurrence of well-developed vein patterns, as well as cracks and holes, was observed. The presence of the vein patterns indicates that the material has sustained large deformation prior to failure. Taken at a larger magnification the picture of the interior of the dendrite (d) confirms an absence of cracks inside the f.c.c. $\gamma$-Fe dendritic phase.

It is well known that the presence of a ductile dendritic phase in the microstructure of a composite BMG is beneficial for its plasticity [Hay00, Küh02, Eck07b]. To get more information on the crack distribution appearing upon compression, the microstructures as well as the fracture surfaces of deformed specimens were analyzed by scanning electron microscopy (Figures 4.2.9a-d).

The first two pictures (Figures 4.2.9a and b) reveal a high number of cracks. The cracks propagate mostly through the interdendritic phases (as indicated by small white arrows in Figures 4.2.9a and b), whereas the interior of the dendrites remains intact. Additionally, some single cracks proceeding along the γ-Fe phase boundaries are also present (denoted by large white arrows in Figure 4.2.9b).

These observations indicate that the soft dendritic precipitates of the austenitic phase efficiently prevent the propagation of cracks. The cracks initiated under compressive loading in the investigated (C) and (D) samples are confined to the interdendritic regions. The f.c.c. γ-Fe particles act as obstacles, which hinder the flow deformation, and hence, cause pronounced strain-hardening. The described observations have been additionally proved by detailed studies of the fracture surfaces of the Fe-based composite materials. The morphology of the fracture surfaces of the as-deformed cylindrical rods is presented in Figures 4.2.9c and d. As shown in Figure 4.2.9c the surface appears to consist of a high number of cracks. Furthermore, vein patterns as well as void-like "black dimples" are visible (marked by white arrows in Figure 4.2.9c).

According to the previously described findings, the absence of cracks inside the dendritic γ-Fe phase was corroborated (as presented in Figure 4.2.9d). The appearance of the above-mentioned features on the fracture surfaces of the examined alloys undoubtedly implies that the materials have experienced large deformation before final failure.

Based on these analyses, it is evident that the combination of the hard interdendritic phases (martensite, cementite, carbide) with the ductile dendritic precipitates (austenite) leads to a high strength from the matrix connected with a very good plasticity from the dendrites. Considering the differences in the microstructures of samples (C) and (D), a detailed clarification of the applied mechanisms of the strengthening is given below.

Although alloy (C) contains a lower volume fraction of the ductility-bearing f.c.c. austenitic phase (41 vol.%) in comparison to alloy (D) (75 vol.% f.c.c.), the achieved plasticity $\varepsilon_f = 36\%$ is superior to that of alloy (D) ($\varepsilon_f = 16\%$). The high amount of martensite as well as of the carbides in the microstructure of (C) does not lead to a material with high yield strength. Furthermore, Young's modulus for alloy (C) is relatively low ($E = 162$ GPa). The advantage of this alloy is, obviously, the large work hardening ability, which is typically caused by enhancing the intensity of the elastic interaction of dislocations by increasing their density under an applied stress. The large strengthening effect can be mainly assigned to a variety of mechanisms to stop dislocation glide. The small carbides act as strong obstacles just like the solute atoms in the crystal lattices and the grain/phase boundaries.

The high yield and true fracture strength ($\sigma_y = 1.41$ GPa, $\sigma_{f(true)} = 3.03$ GPa) of alloy (D) is a consequence of the hard cementite, because the solute strengthening effect of the second existing phase, the f.c.c. phase, is rather small [Mug93]. Presumably the grain boundaries of the austenitic f.c.c. phase hinder dislocation glide leading to the development of significant strain gradients in the material. The cementite ($Fe_3C$), which additionally contains Cr and Mo, contributes hardness and brittleness to the material because of the asymmetrical orthorhombic lattice structure, which is characterized by a low number of slip systems [Got07]. In contrast, the f.c.c. phase is ductile. Therefore, the mechanical response of such a composite structure leads to high strength in combination with considerable plastic deformability.

Summarizing briefly, the studied $(Fe_{84.4}Cr_{5.2}Mo_{5.2}Ga_{5.2})_{91}C_9$ and $(Fe_{84.4}Cr_{5.2}Mo_{5.2}Ga_{5.2})_{83}C_{17}$ alloy compositions represent a promising step toward developing new Fe-based materials with improved mechanical properties. As it is demonstrated, due to their structural complexity such alloys exhibit excellent compressive strength ($\sigma_f = 2.9$ GPa for alloy (C) and $\sigma_f = 3.03$ GPa for alloy (D)) associated with good plasticity (with increasing carbon concentration, the compressive fracture strain of the investigated alloys decreases from $\varepsilon_f = 36\%$ to $\varepsilon_f = 16\%$). Compared to their amorphous $Fe_{65.5}Cr_4Mo_4Ga_4P_{12}C_5B_{5.5}$ counterpart, samples (C) and (D) manifest congenial fracture strength, while the values of fracture strain are greatly enhanced. However, in order to provide more detailed information on the factors governing the

ductility of the investigated composites, further compositional modifications were done. In principal, the effect of Ga on the microstructure and the mechanical response of the studied Fe-based materials was discerned. Due to the fact, that the soft reinforcing austenitic phase was found to be Ga-enriched, the main attention has been posed on clarifying the role of such an element in enhancing the plasticity of the studied alloys. Based on the results presented so far, it was proved that the increase in plastic deformation is due to the ductile nature of the Ga-rich γ-Fe particles…*so what will happen if Ga would be eliminated from the alloy system?* Following this idea, the last step of this work was dedicated to developing novel Ga-free alloys.

**4.3 The Fe-Cr-Mo-C alloy system** – *to add or not to add Ga?*

To answer the above question, two alloy compositions $(Fe_{89.0}Cr_{5.5}Mo_{5.5})_{91}C_9$ (E) and $(Fe_{89.0}Cr_{5.5}Mo_{5.5})_{83}C_{17}$ (F) have widely been studied. It was presumed that variations in the chemistry (Ga substitution) will lead to changes in the microstructure and in the mechanical response of the investigated alloys.

- Structure morphology

Figure 4.3.1 illustrates X-ray diffraction traces for the as-cast $(Fe_{89.0}Cr_{5.5}Mo_{5.5})_{100-x}C_x$ alloys with x = 9,17 at.%. In the case of sample (E) the predominant phases are identified as face-centered (f.c.c) austenitic (γ-Fe) and body-centered tetragonal (b.c.t.) martensitic. Moreover, additional diffraction peaks belonging to a $CFe_{2.5}$ compound are visible. Also sample (F) displays the formation of a f.c.c. austenitic phase. Several reflections can be indexed as $Fe_3C$ (cementite) with an orthorhombic crystal structure. There is no evidence of any other phases in this alloy. The mixture of phases formed upon solidification, as revealed for samples (E) and (F) is in good agreement with the phase formation reported for the Ga-comprising alloys. However, compared to its Ga-containing counterpart, alloy (E) does not manifest the formation of a chromium/molybdenum carbide $((Cr,Mo)_2C)$ phase. Instead, a $CFe_{2.5}$ compound is observed.

Unlike it was predicted the changes in the chemical composition – Ga substitution – do not cause an appreciable variation in the microstructure of the investigated Fe-based

alloy systems. On the other hand, as it will be shown in a further part of this section, such Ga-free alloys subjected to compressive load demonstrate lower plastic deformation up to catastrophic failure than previously tested compositions. Especially, for the sample with the higher carbon concentration - $(Fe_{89.0}Cr_{5.5}Mo_{5.5})_{83}C_{17}$, a remarkably smaller fracture strain was noticed. In order to elucidate the origins, which lead to such a significant drop in ductility of the as-cast specimen (F), a detailed analysis of its deformation as well as its fracture mode was performed. The obtained results will be discussed later.
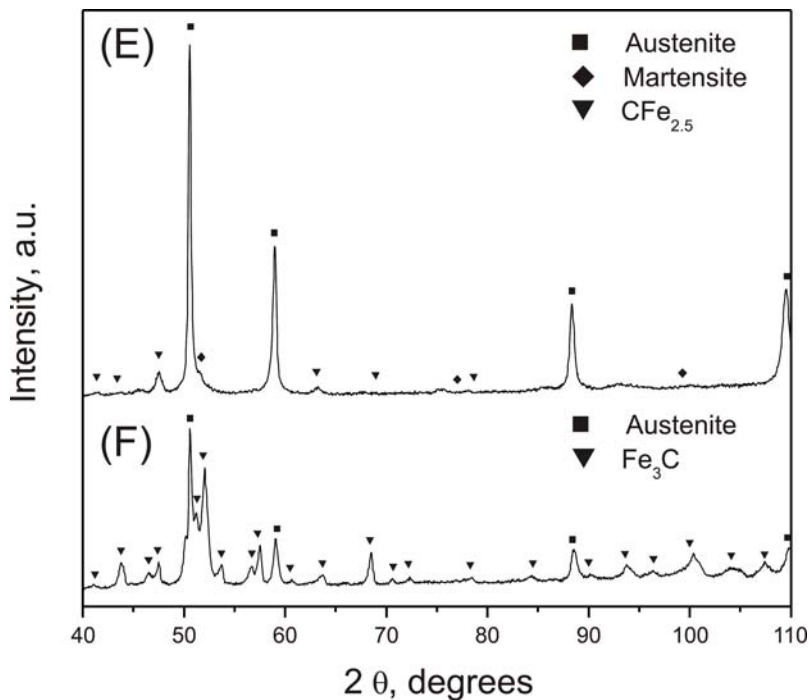


**Figure 4.3.1.** XRD patterns for the as-cast rods: (E) - $(Fe_{89.0}Cr_{5.5}Mo_{5.5})_{91}C_9$ and (F) - $(Fe_{89.0}Cr_{5.5}Mo_{5.5})_{83}C_{17}$. Except of slight differences (as described in the text), the XRD scans obtained in this study are consistent with those reported for Ga-containing alloys.

The scanning electron micrographs – see Figures 4.3.2a-f reveal the details on the microstructure of the examined alloys. Both samples possess a complex structure, which is composed of micron-sized dendrites of the austenitic phase dispersed in a matrix. However, there are considerable differences in the morphology of the observed dendrites.

For sample (E) the precipitated γ-Fe phase is more spherical. On the other hand, the shape of the dendrites varies along the cross-section from a mixture of round and elongated particles (outermost region) to mainly spherical in the inner part of the rod. In contrast, the dendrites visible for sample (F) demonstrate both a round and an elongated shape over the whole cross-section. In the case of alloy (E) – Figure 4.3.2c, the estimated average dimensions of the γ-Fe precipitates are in the range of 5-10 µm. The values achieved for alloy (F) – Figure 4.3.2f, are about 2-5 µm (spherical particles) and for the elongated precipitates a few microns in width and above 50 µm in length. Obviously, the outermost rod regions (Figures 4.3.2a and c) display a finer microstructure compared to the centre areas (Figures 4.3.2b and d). As already mentioned in section 4.2, such differences are due to the gradient of the cooling rate within the as-cast cylinders. Its appearance is associated with the heat diffusion in the cooper mold. Clearly, the direct contact between the molten liquid metal and the cold walls of the casting mold leads to a very high undercooling. From the *"nucleation and growth theory"* it is well known that such solidification conditions favour the formation of a large number of critical nuclei which, subsequently, grow until the new phase fills the whole system [Haa05]. In consequence, the outermost region of the ingot displays a fine-grained microstructure.

To evaluate the composition of the phases found for the particular samples, EDX experiments were realized. In general, both alloys exhibit an enrichment in Fe and a depletion in Mo in the dendritic f.c.c. phase, while the interdendritic phases (the martensite and the carbides) show higher Mo contents in comparison to the overall alloy composition. Additionally, for sample (E) a very high concentration of Cr was detected in the matrix. Due to the dissimilarities in the morphology of the precipitated γ-Fe particles – as observed for sample (F), the chemistry of the individual precipitates was determined. It was found that the round-shaped dendrites are reduced in Cr compared to the given nominal composition. Contrary, there is an enrichment of Cr for the elongated particles.
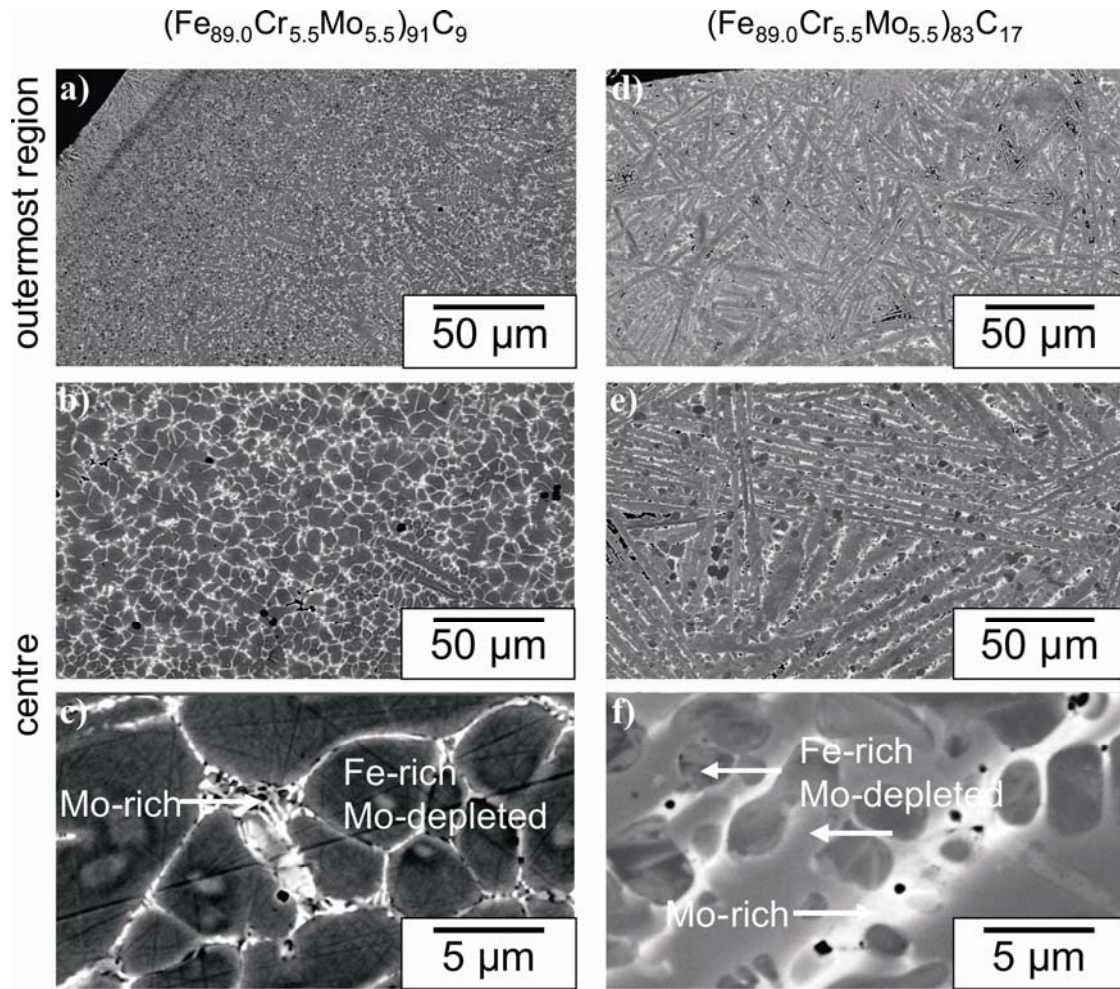
**Figure 4.3.2.** Back-scattering SEM images showing the microstructure of as-cast ingots: (E) - $(Fe_{89.0}Cr_{5.5}Mo_{5.5})_{91}C_9$ (a,b,c) and (F) - $(Fe_{89.0}Cr_{5.5}Mo_{5.5})_{83}C_{17}$ (d,e,f). Both samples display a gradual increase of the size of the dendritic phase towards the centre – images (a,b) and (d,e). Taken at higer magnification, the micrographs (c,f) present in detail the dendrite and matrix morphology in the centre area of the rods. The shape of the precipitated phase varies from globular - sample (E), to a mixture of spherical and elongated particles for sample (F). According to the EDX analysis the dendritic phase (for both samples identified as f.c.c. γ-Fe austenite) is Mo-depleted. On the contrary, the regions between the dendrites exihibt a significant enrichment of Mo compared to the overall composition.

Because of the complexity of the formed microstructures it was necessary to verify the phase identification as well as the SEM observations by means of TEM. Principally, the structure between the dendrites, which was assigned to be a mixture of martensite and a $CFe_{2.5}$ phase for sample (E) and eutectic, composed of austenite and cementite, for sample (F), was carefully analyzed by TEM.
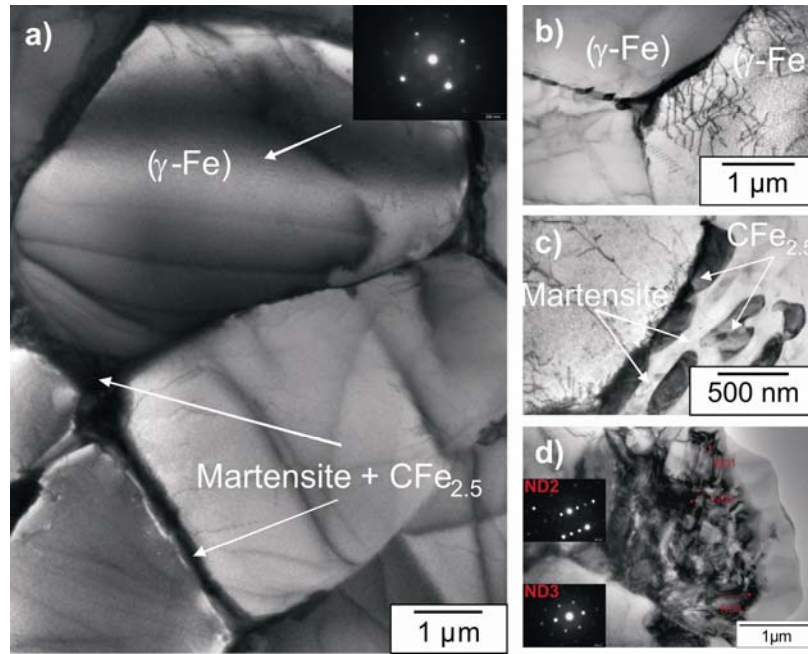


**Figure 4.3.3.**  Bright-field TEM images illustrating the characteristics of the microstructure of the as-cast $(Fe_{89.0}Cr_{5.5}Mo_{5.5})_{91}C_9$ alloy: a) overview of the microstructure with a nano-diffraction pattern taken from the dendritic f.c.c. phase; b) large number of dislocations proceeding through the austenite; c) bead-shaped carbides; d) image of the matrix with corresponding nano-diffraction patterns.

Figures 4.3.3a-d depict the as-cast microstructure of the $(Fe_{89.0}Cr_{5.5}Mo_{5.5})_{91}C_9$ alloy. The existence of large γ-Fe dendrites embedded in a matrix was clearly observed. TEM studies revealed that the carbides are bead-shaped and localized either at the phase boundaries of austenite/austenite (Figure 4.3.3b) or distributed between the martensite plates (Figure 4.3.3c). Selected area nano-diffraction patterns are shown as insets of

Figures 4.3.3a and d. The appearance of a high density of dislocations already in an undeformed state was ascertained (see images b and c). As it can be seen, the dislocation motion is confined to the austenitic f.c.c. phase. Due to the fact that the grain boundaries of the austenite as well as the small precipitates of a carbon phase obstruct a dislocation glide, it was expected that sample (E) subjected to compression loading will exhibit a large strengthening effect.

In addition, TEM-EDX results obtained for the investigated (E) cylinder are presented in Figures 4.3.4a-c.
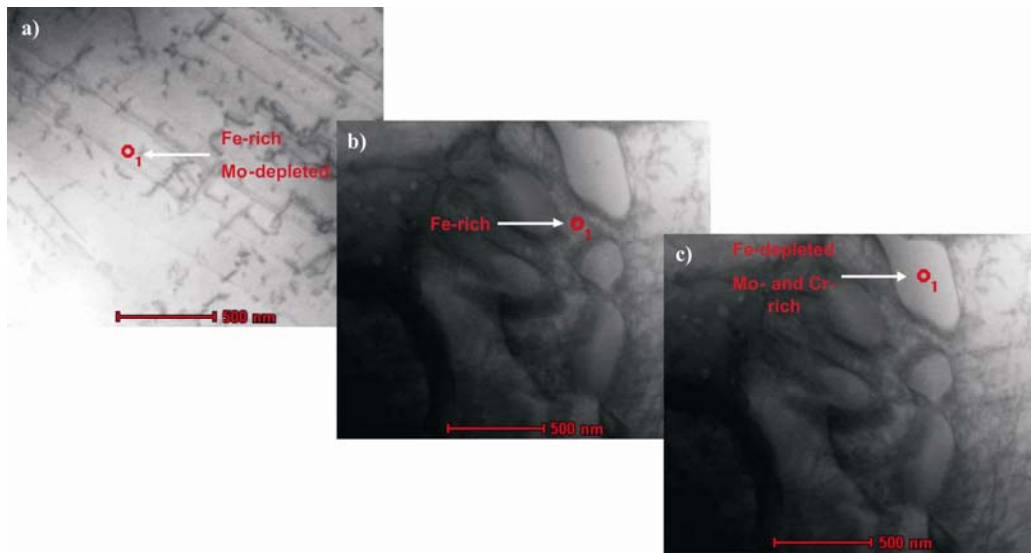


**Figure 4.3.4.**   Bright-field TEM images of the $(Fe_{89.0}Cr_{5.5}Mo_{5.5})_{91}C_9$ composite displaying changes of Fe, Mo and Cr concentration determined by TEM-EDX for the individual phases: a) dendrites of the austenite; b) matrix – bright Fe-enriched martensitic phase; c) matrix – dark Mo- and Cr-enriched and Fe-depleted carbides.

Figures 4.3.5a-c exhibit bright-field TEM micrographs of the $(Fe_{89.0}Cr_{5.5}Mo_{5.5})_{83}C_{17}$ alloy. The microstructure of the as-prepared rod (see upper image) contains micron-sized dendrites distributed in a fine and complex matrix phase, which is a mixture of a f.c.c. $\gamma$-Fe phase and a nano-sized carbide phase ($Fe_3C$). The images c) and d) show in detail the internal structure of the matrix phase. Moreover, the corresponding

selected area nano-diffraction patterns confirming the formation of the above-mentioned compounds are presented (insets of Figure 4.3.5a).
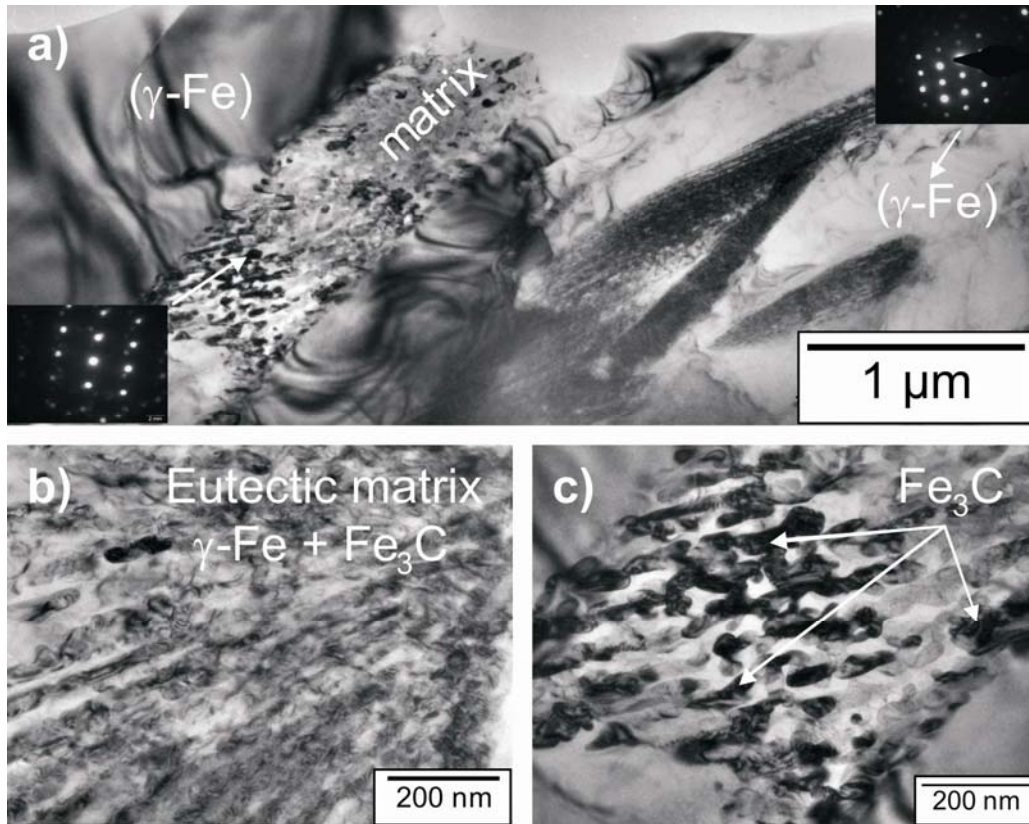


**Figure 4.3.5.**   Bright-field TEM images displaying the characteristics of the microstructure of the as-cast $(Fe_{89.0}Cr_{5.5}Mo_{5.5})_{83}C_{17}$ alloy: a) overview of the microstructure with corresponding nano-diffraction patterns; b) detailed insight into the eutectic matrix; c) enlargement of the matrix phase illustrating the carbide phase distribution.

The local variations of the concentration of the particular elements are demonstrated in Figure 4.3.6. Naturally, Mo mostly resides in the eutectic matrix (Figures 4.3.6b and c), while Fe tends to stay in the f.c.c. austenitic phase (Figures 4.3.6a and b).
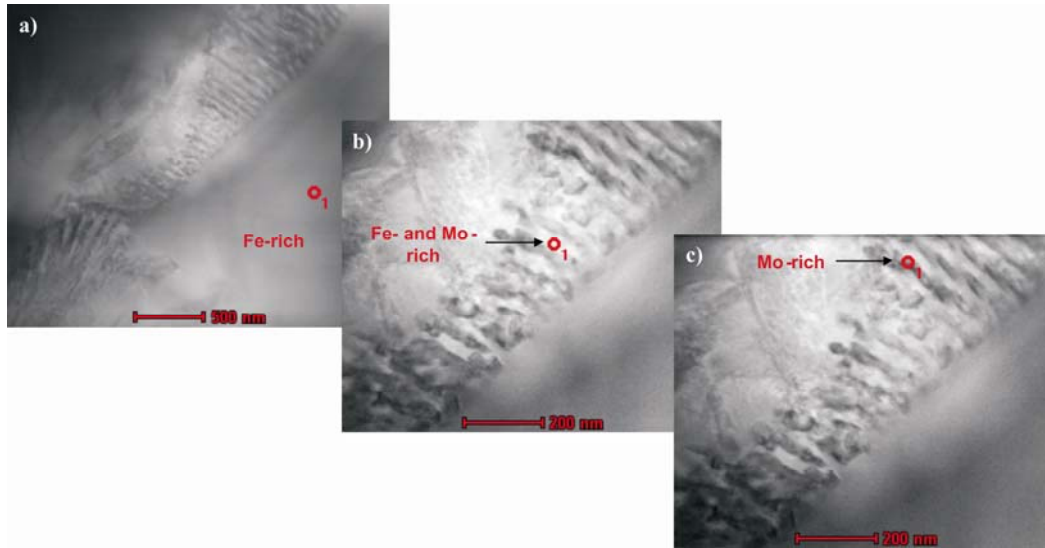
**Figure 4.3.6.** Bright-field TEM images of the $(Fe_{89.0}Cr_{5.5}Mo_{5.5})_{83}C_{17}$ composite displaying changes of the Fe, Mo and Cr concentration determined by TEM-EDX for the individual phases: a) dendrites of the austenite; b) eutectic – bright: Fe- and Mo-enriched $\gamma$-Fe phase; c) eutectic – dark: Mo-enriched carbide precipitates.

The revealed microstructural features of the studied alloys (E) and (F), show good agreement with those of their Ga-counterparts. Nevertheless, as it will be featured next, the fracture strain acquired for the as-cast $(Fe_{89.0}Cr_{5.5}Mo_{5.5})_{83}C_{17}$ sample is much lower compared to the Ga-comprising alloy. To explain this "unclearness" a series of experiments on the mechanical behavior of the investigated alloys was carried out.

- Mechanical response of the compressed $(Fe_{89.0}Cr_{5.5}Mo_{5.5})_{91}C_9$ and $(Fe_{89.0}Cr_{5.5}Mo_{5.5})_{83}C_{17}$ rods

The mechanical response of the deformed alloys (E) and (F) was investigated by room temperature compression tests. Figure 4.3.7 depicts the typical true stress-strain curves together with the corresponding mechanical properties (table-inset of Figure 4.3.7). The data reported by Stoica for the fully amorphous $Fe_{65.5}Cr_4Mo_4Ga_4P_{12}C_5B_{5.5}$ alloy are given for comparison. As displayed in Figure 4.3.7, alloy (E) - $(Fe_{89.0}Cr_{5.5}Mo_{5.5})_{91}C_9$ is characterized by a large compressive strain ($\varepsilon_{f(true)} \approx 38\%$) and a

very high compressive strength ($\sigma_{f(true)} \approx 3.0$ GPa), which are comparable with values measured for its Ga-comprising counterpart. The as-cast rods of $(Fe_{89.0}Cr_{5.5}Mo_{5.5})_{91}C_9$ and $(Fe_{84.4}Cr_{5.2}Mo_{5.2}Ga_{5.2})_{91}C_9$ subjected to compressive load behave in a similar manner. Both samples undergo elastic deformation followed by plastic yielding, plastic deformation associated with very strong work hardening, and final failure. Obviously, the pronounced strain hardening behavior as noticed for the above-mentioned alloys is responsible for their impressive mechanical strength. For both compositions the increase in the flow stress is about 2000 MPa. However, it was found that the ductility of the $(Fe_{89.0}Cr_{5.5}Mo_{5.5})_{83}C_{17}$ rod is significantly lower compared to the earlier investigated $(Fe_{84.4}Cr_{5.2}Mo_{5.2}Ga_{5.2})_{83}C_{17}$ alloy. The fracture strain decreases from $\varepsilon_{f(true)} \approx 16\%$ (Ga-containing sample) to $\varepsilon_{f(true)} \approx 5\%$ (Ga-free sample). On the other hand, there is a slight increase of the fracture strength for the as-cast $(Fe_{89.0}Cr_{5.5}Mo_{5.5})_{83}C_{17}$ alloy. Among all the Fe-based alloy systems examined in this thesis work, the $(Fe_{89.0}Cr_{5.5}Mo_{5.5})_{83}C_{17}$ composition possesses the highest compressive strength ($\sigma_f \approx 3.3$ GPa). It is well known that an increase in strength is mostly associated with a deterioration in plasticity [Pic92]. Thus, the most important issue is to find the balance between these two engineering features of the material. Such a desirable equilibrium was found for the Ga-comprising alloy with 17 at.% C. Based on this result, it is clear that Ga additions as well as a proper C concentration are essential for enhancing the mechanical properties of the complex Fe-based materials discussed here.

Although there are some differences in the mechanical response of the investigated Fe-based systems, all of them manifest an enhanced plasticity compared to monolithic $Fe_{65.5}Cr_4Mo_4Ga_4P_{12}C_5B_{5.5}$ glass ($\varepsilon_{pl} \approx 0.12\%$) - in the case of in-situ formed Fe-Cr-Mo-C composites the plastic strain for alloy (E) is 37% and for alloy (F) is 4%, respectively.

Moreover, in most cases the accessible values of the fracture compressive strength ($\sigma_f$) are equal to those achieved for the fully glassy Fe-based alloy. However, compared to the base BMG, featured in this work, complex Fe-based materials show a strong reduction of the compressive yield strength ($\sigma_y$). Obviously, this specific mechanical property is appreciably lower for the conventional crystalline alloys.
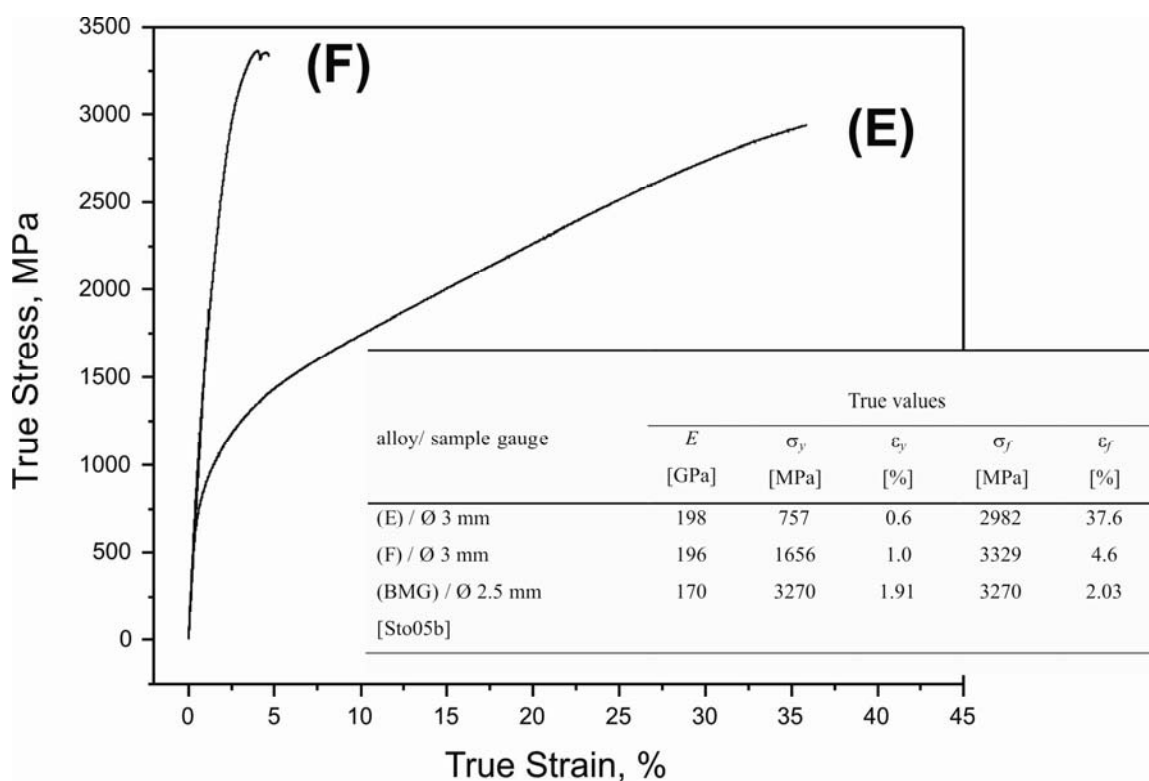
| alloy/ sample gauge | True values | | | | |
|---|---|---|---|---|---|
| | $E$ | $\sigma_y$ | $\varepsilon_y$ | $\sigma_f$ | $\varepsilon_f$ |
| | [GPa] | [MPa] | [%] | [MPa] | [%] |
| (E) / Ø 3 mm | 198 | 757 | 0.6 | 2982 | 37.6 |
| (F) / Ø 3 mm | 196 | 1656 | 1.0 | 3329 | 4.6 |
| (BMG) / Ø 2.5 mm | 170 | 3270 | 1.91 | 3270 | 2.03 |
| [Sto05b] | | | | | |

**Figure 4.3.7.**    Typical compressive true stress-strain curves of the as-cast crystalline (E)   $(Fe_{89.0}Cr_{5.5}Mo_{5.5})_{91}C_9$   and   (F)   $(Fe_{89.0}Cr_{5.5}Mo_{5.5})_{83}C_{17}$   rods demonstrating the distinctive correlation between the chemical composition, the microstructure and the mechanical behavior of the material. Additionally, the data reported by Stoica for the $Fe_{65.5}Cr_4Mo_4Ga_4P_{12}C_5B_{5.5}$ glassy alloy are given for comparison.

From the previous observation, it follows that the outstanding mechanical properties can be linked to the unique interaction between high-strength and ductile (Ga-enriched γ-Fe) areas present in the revealed microstructures. To analyze the eventual changes in their properties (due to the Ga substitution), Vickers microhardness measurements were realized. Generally, it was found that the microstructures of both (E) and (F) specimens are composed of a hard (matrix) and a soft (second phase precipitates) regions. These findings are consistent with results obtained for Ga-containing composites.

The mean value for the Mo-rich interdendritic phases (martensite+carbide for alloy (E)) is 4.0 GPa and for the eutectic phase (austenite+cementite for alloy (F)) is 10.7 GPa, respectively. Meanwhile, the microhardness of the Fe-rich dendritic austenite was evaluated to be 2.1 GPa for (E) and 3.0 GPa for (F), respectively. Comparing these values with values measured for previously studied compositions: $(Fe_{84.4}Cr_{5.2}Mo_{5.2}Ga_{5.2})_{91}C_9$ (C) and $(Fe_{84.4}Cr_{5.2}Mo_{5.2}Ga_{5.2})_{83}C_{17}$ (D), one can see a strong increase of the hardness of the matrix phase ($\uparrow \approx 3$ GPa) for the as-cast sample (F) $(Fe_{89.0}Cr_{5.5}Mo_{5.5})_{83}C_{17}$. As mentioned earlier, such an alloy exhibits the highest strength prior to failure among all the deformed Fe-based rods. Unfortunately, compared to the other compressed samples its plastic deformation response (strain to failure) is drastically reduced. These results clearly indicate that for the selected compositions (the alloys with 17 at.% of carbon) the Ga addition leads to an impressive improvement in plasticity. Moreover, the value of 10.7 GPa (martensite+carbide) is greater than the microhardness calculated for the glassy $Fe_{65.5}Cr_4Mo_4Ga_4P_{12}C_5B_{5.5}$ alloy (8 GPa) [Sto05a, Sto05b].

- Fractography - *is the Ga addition crucial for the ductility of the investigated Fe-based complex materials?*

Trying to understand further the changes in the mechanical response of the investigated Fe-based complex materials, an extensive failure analysis of the deformed rods has been conducted. In order to identify the fracture features, the microstructures as well as the fracture surfaces of the compressed specimens (E) and (F) were analyzed by scanning electron microscopy.

As illustrated in Figures 4.3.8a-c, the fractured (E) sample appears to consist of a high number of small cracks. Insight into the microstructure reveals that the cracks proceed mainly through the interdendritic phases (as denoted by white circles). In contrast, the interior of the γ-Fe dendrites remains intact. Only the SEM image taken at a higher magnification (Figure 4.3.8c) displays some single cracks travelling across the γ-Fe phase (as denoted by black arrows in Figure 4.3.8c).
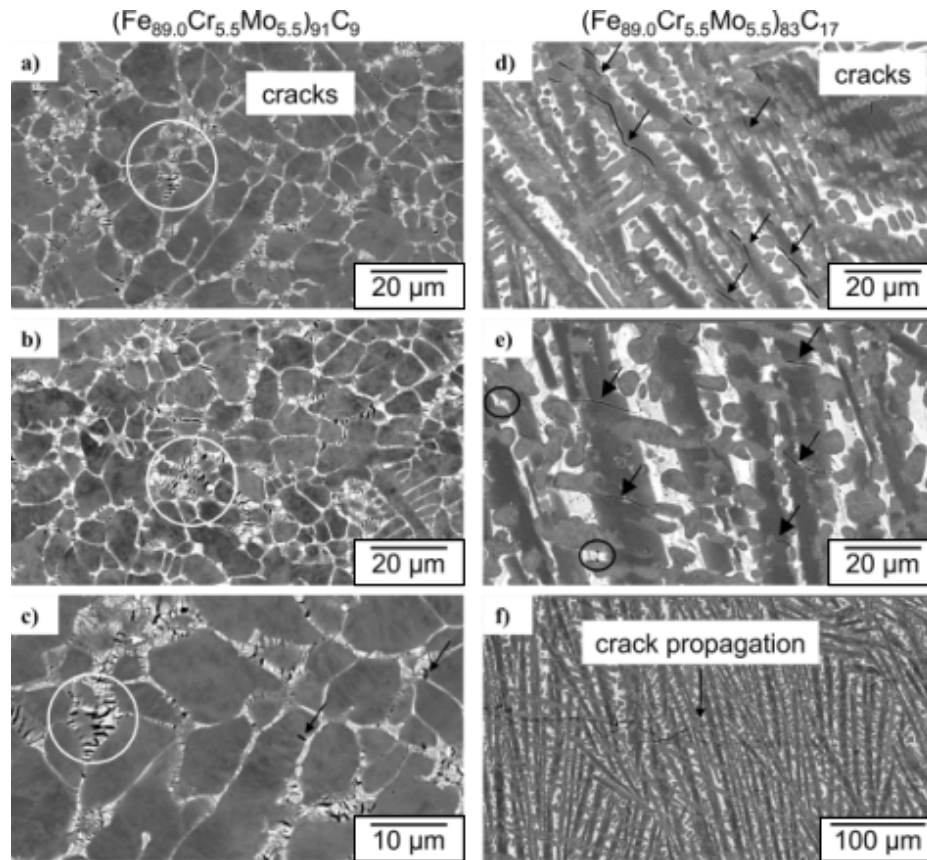
**Figure 4.3.8.** Observations on the deformed cross-section of the (E) $(Fe_{89.0}Cr_{5.5}Mo_{5.5})_{91}C_9$ (a-c) and (F) $(Fe_{89.0}Cr_{5.5}Mo_{5.5})_{83}C_{17}$ (d-f) cylinders. SEM backscattered images a),b) and c) show a high number of cracks proceeding through the interdendritic regions (white circles). Additionally, taken at higher magnification, the image c) reveals some single cracks cutting through the ductile dendritic phase (small black arrows). Obviously, the crack propagation is stopped by dendrites. In strong contrast, the cracks formed during compression of sample (F) are mainly localized in the dendritic regions (see images d) and e)). Deformation propagates either along the γ-Fe particles (small black arrows) or cuts through the dendrites (large black arrows). The occurrence of some single cracks in the matrix was also observed (black circles).

Considering the morphology of the individual phases it is clear that the observed differences are induced by the variations of their mechanical properties. The soft dendritic precipitates of the austenitic phase act as the obstacles, which efficiently hinder the propagation of cracks, and hence, lead to a pronounced strain-hardening. Therefore, the cracks initiated under compression in the investigated sample (E) are confined to the hard interdendritic regions (martensite+carbides). Combining the above findings it is claimed that the interplay between ductile and high-strength phases is responsible for the excellent mechanical behavior of the studied $(Fe_{89.0}Cr_{5.5}Mo_{5.5})_{91}C_9$ alloy.

Quite different microstructural features were observed for the deformed sample (F). Contrary to the aforementioned results, an appearance of the cracks within the dendritic phase was observed (see Figures 4.3.8c-f). A closer look at the revealed microstructure shows that the cracks propagate either along the $\gamma$-Fe particles (small black arrows) or simply cut through the dendrites (large black arrows). In addition, a small amount of cracks proceeding through the interdendritic regions was recognized (denoted by black circles). The development of a long crack is presented in Figure 4.3.8f.

The revealed features - low number of cracks in the entire fractured sample (F), deformation propagating along the soft $\gamma$-Fe dendritic phase (in this case ductile precipitates of the second phase do not prevent the crack propagation) imply that the flow deformation ability of the tested alloy is relatively low. Such observations could explain the dissimilarities in the mechanical response of the as-cast $(Fe_{89.0}Cr_{5.5}Mo_{5.5})_{91}C_9$ rod and its Ga-containing counterpart. Although both alloys are composed of a mixture of austenite and cementite, it has been found that the changes in the chemical composition (Ga substitution) affect strongly the mechanical response of the individual phases, what finally results in a deterioration of the plasticity of the Ga-free sample. It is assumed that the local enrichment in Ga in the f.c.c. $\gamma$-Fe phase as observed for the $(Fe_{84.4}Cr_{5.2}Mo_{5.2}Ga_{5.2})_{83}C_{17}$ alloy is crucial for the enhancement of its macroscopic ductility. The performed experiments proved that for the alloys with 17 at.% C the presence of soft Ga-enriched dendrites in the microstructure is beneficial for plasticity. Furthermore, the very high value of the hardness as estimated for the interdendritic regions of the as-cast $(Fe_{89.0}Cr_{5.5}Mo_{5.5})_{91}C_9$ rod suggests that such places are characterized by high stress concentrations. However, when the stress exceeds a certain

level, the cracks formed under applied load cannot be further stopped by the soft γ-Fe dendrites. Hence, the deformation is transferred from the matrix phase into the dendritic phase. As a consequence, such material does not manifest a noticeable strain-hardening (the fracture strain is low).

Subsequent detailed studies on the fracture morphology of the Fe-based composite materials have corroborated the above-described observations. The fractography of the $(Fe_{89.0}Cr_{5.5}Mo_{5.5})_{91}C_9$ (E) alloy is presented in Figures 4.3.9a-c. The revealed fracture surface shows two distinct morphologies: a) vein-like patterns (marked by large white arrows) and (b) intermittent smooth areas (marked by large black arrows) [Kus06, Eck07b]. The vein-like structure is defined as a region where due to local heating a high temperature is acquired [Kus06, Eck07b]. The presence of well-developed vein-patterns on the fracture plane is a typical characteristic of ductile fracture features – see Figure 4.3.9c. In turn, the formation of intermittent smooth areas takes place when fast crack propagation is locally established after overcoming the threshold dictated by second phase particles [Kus06, Eck07b]. The appearance of such fractography supports previously depicted results. Based on the performed analyses it is evident that the coexistence of the hard interdendritic phases (martensite, carbide) with the ductile dendritic precipitates (austenite) leads to the high strength from the matrix connected with very good plasticity from the dendrites.

The fracture surface of the $(Fe_{89.0}Cr_{5.5}Mo_{5.5})_{83}C_{17}$ (F) alloy is displayed in Figures 4.3.10a-c. Compared to the previous sample, the fracture morphology does not show a vein-like pattern. The fracture plane is covered mainly by a cleavage-like structure containing a large number of cracks (small black arrows) as well as void-like "black dimples" (white large arrows and black circles) (see Figure 4.3.10c). Besides the mentioned fractographic motives, the structure of the studied sample has also been revealed. According to the phase analysis performed, dark areas can be assigned to a f.c.c. austenitic γ-Fe phase, which is surrounded by an interdendritic eutectic phase of austenite and cementite (bright areas) – as demonstrated in Figure 4.3.10c.
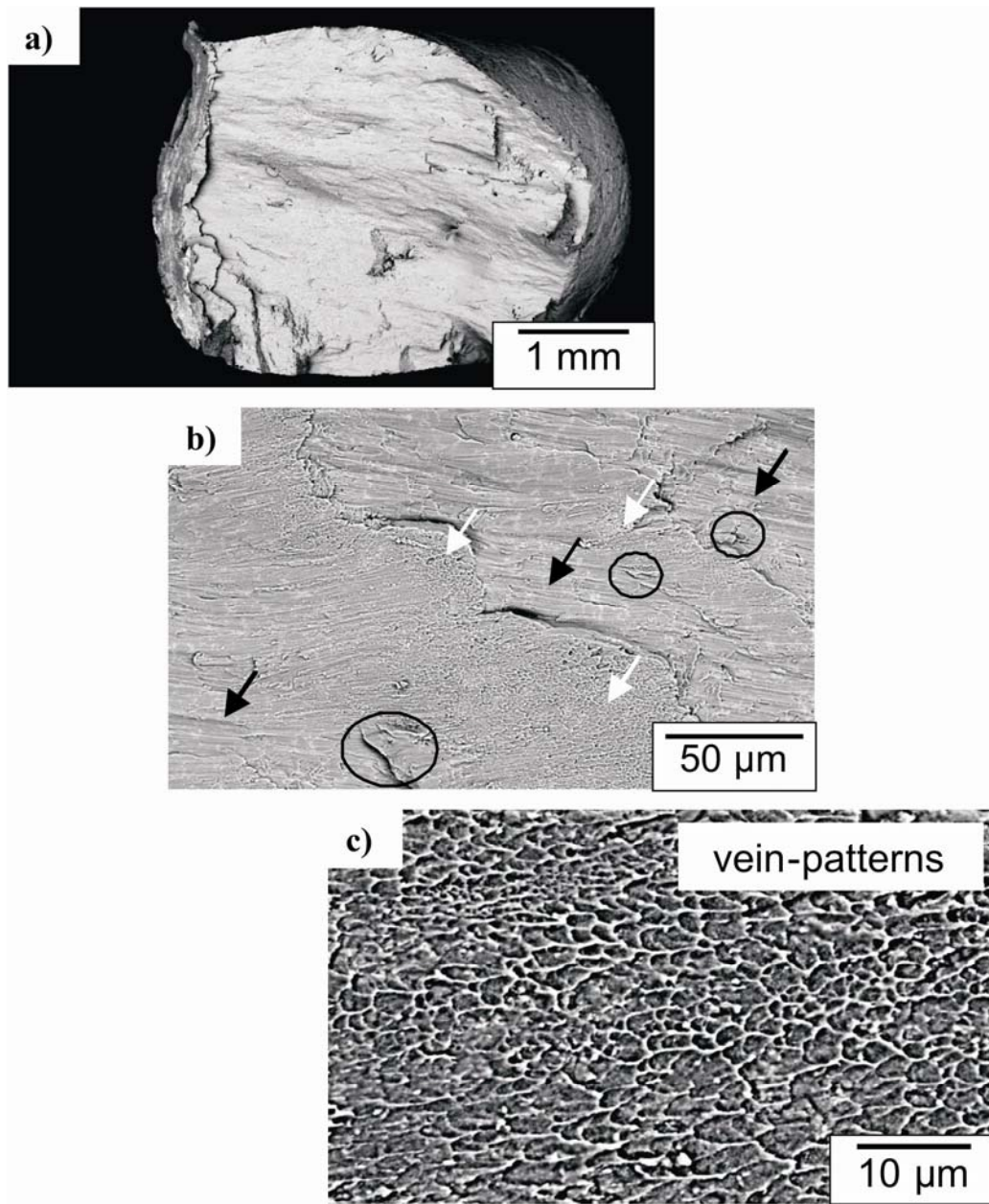
**Figure 4.3.9.** Fracture morphology formed on the fracture surface of the $(Fe_{89.0}Cr_{5.5}Mo_{5.5})_{91}C_9$ (E) alloy upon compression: a) overview of the deformed cylinder, b) coexistence of a vein-like pattern (white large arrows) and intermittent smooth regions (black large arrows), c) enlargement of a well-developed vein-like structure. Additionally, some cracks revealed on the fracture surface of the examined sample are denoted by black circles (b).
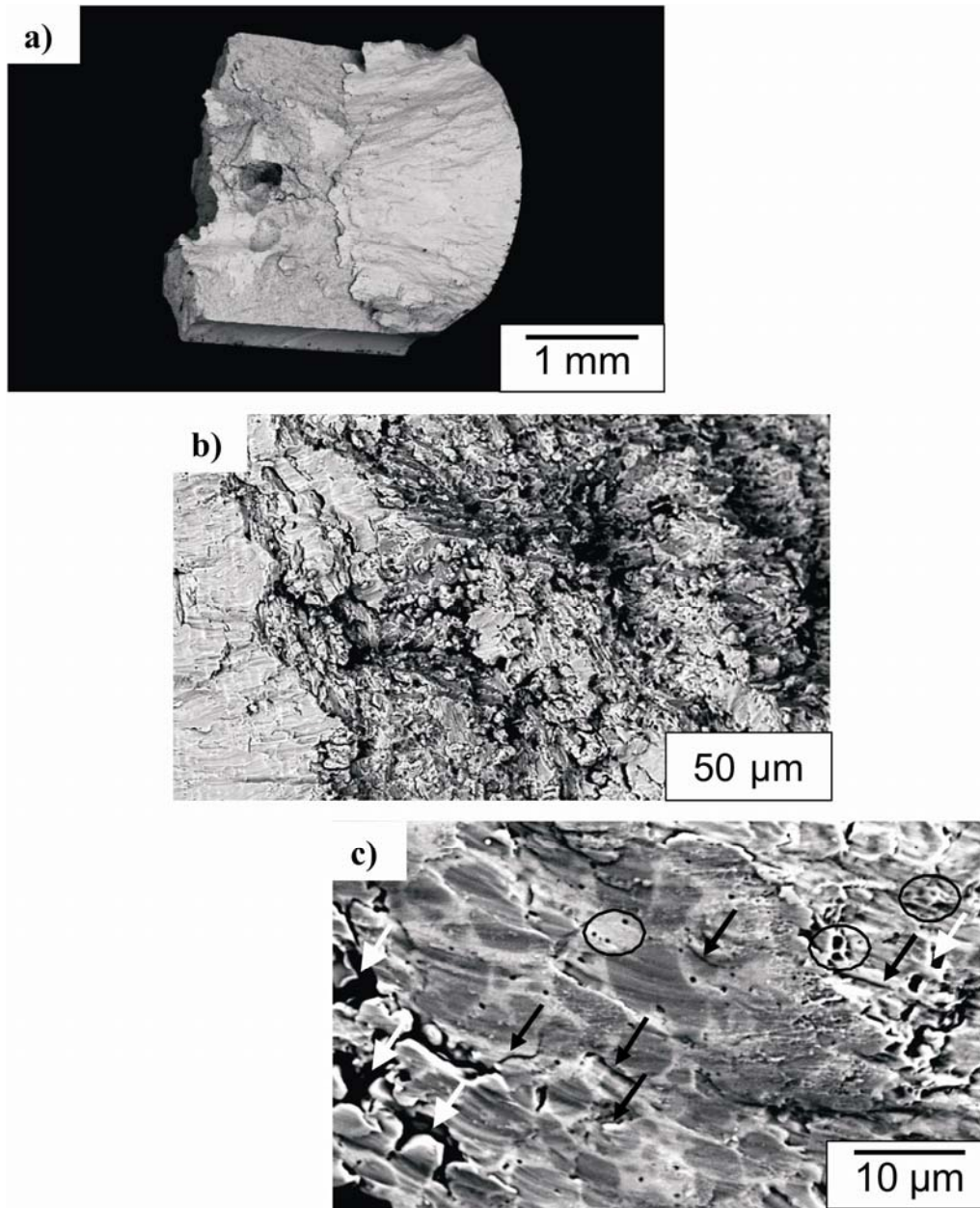
**Figure 4.3.10.** Fractography of the $(Fe_{89.0}Cr_{5.5}Mo_{5.5})_{83}C_{17}$ (F) alloy showing an overview of the fracture morphology (a-c). Images b) and c) illustrate the dendrites and the matrix phase on the fracture surface of the compressed cylinder. Moreover, the presence of a high number of cracks and void-like "black dimples" was observed. The revealed morphology evidently indicates that sample (F) behaves in a brittle manner upon deformation.

Different fractographic features observed for the investigated alloys (E) and (F) indicate the change in the deformation mode. These observations agree with the obtained mechanical characteristics. A very high fracture strength combined with an excellent fracture strain as obtained for the $(Fe_{89.0}Cr_{5.5}Mo_{5.5})_{91}C_9$ alloy and the Ga- and C-comprising compositions reported in these studies, are a consequence of the interplay between soft and hard phases. For the mentioned alloys, it was evident that γ-Fe dendrites confine the crack propagation and contribute to the plasticity. Contrary, in the case of the $(Fe_{89.0}Cr_{5.5}Mo_{5.5})_{83}C_{17}$ alloy, the plastic flow is no longer obstructed by the microscale γ-Fe precipitates. It results in catastrophic failure of the sample with insignificant plastic strain ($\varepsilon_f \approx 5\%$).

# CHAPTER 5

# Concluding remarks and future trends

*Owing to the rising materials market requirements, there is enormous potential for new compositions to be identified and then optimized...*

In this study, novel Fe-based multi-phase materials derived from a monolithic bulk metallic glass-forming composition [Sto05a, Sto05b] were successfully prepared by rapid quenching from the melt. Following the purpose of the work – *improvement of the ductility of the high-strength $Fe_{65.5}Cr_4Mo_4Ga_4P_{12}C_5B_{5.5}$ glassy alloy*, the interplay between the chemistry, the microstructure and the mechanical behavior of the studied compositions was analyzed in detail. Although, the here presented Fe-based alloys are fully crystalline, they have proved to be very fruitful in developing materials with excellent strength ($\sigma_f$ values are comparable with those reported for the reference BMG) combined with good ductility (greatly improved compared to the $Fe_{65.5}Cr_4Mo_4Ga_4P_{12}C_5B_{5.5}$ glassy alloy).

*"Since the Iron Age, iron has been the most commonly used metal in human society"* [Gu07].

Taking into account a long tradition of iron usage, its low cost and the very promising mechanical properties as observed for the alloys developed in this work, it is expected that this group of materials can play a significant role in the further development of new advanced materials, which can be exploited for a variety of engineering applications.

**5.1 Concluding remarks** – *considerations on the microstructure and the resulting mechanical properties*

*In general...*

It has been recognized that subtle modifications of the chemical composition (carbon addition) lead to appreciable changes in the phase formation, which occurs upon solidification (from *a single-phase structure* to *composite materials*). As a consequence,

significant differences in the mechanical response of the particular samples have been observed.

Considering the microstructures of the studied alloys: $Fe_{81.2}Cr_{5.2}Mo_{5.2}Ga_{5.2}Si_{3.2}$ (A), $Fe_{78.0}Cr_{5.2}Mo_{5.2}Ga_{5.2}Si_{6.4}$ (B), $(Fe_{84.4}Cr_{5.2}Mo_{5.2}Ga_{5.2})_{91}C_9$ (C), $(Fe_{84.4}Cr_{5.2}Mo_{5.2}Ga_{5.2})_{83}C_{17}$ (D), $(Fe_{89.0}Cr_{5.5}Mo_{5.5})_{91}C_9$ (E) and $(Fe_{89.0}Cr_{5.5}Mo_{5.5})_{83}C_{17}$ (F), it has been observed that the origin for the formation of a composite microstructure is directly attributed to the carbon presence. In contrast, as-cast samples (A1) and (B1) (carbon free) manifest a single-phase structure. Furthermore, the variations of the carbon content (9 at.% and 17 at.%) for the Fe-Cr-Mo-Ga-C and Fe-Cr-Mo-C alloy systems result in significant changes in the deformation mode. With increasing carbon concentration, the ductility of the investigated alloys decreases from $\varepsilon_f = 36\%$ to $\varepsilon_f = 16\%$ for alloys (C) and (D), and from $\varepsilon_f = 38\%$ to $\varepsilon_f = 5\%$ for alloys (E) and (F), respectively. On the other hand, all the alloys manifest a congenial fracture strength, i.e. $\sigma_f = 2.9$ GPa (C), $\sigma_f = 3.03$ GPa (D), $\sigma_f = 3.0$ GPa (E) and $\sigma_f = 3.3$ GPa (F). While the obtained values of fracture strength are similar to data reported by Stoica *et al.* for the $Fe_{65.5}Cr_4Mo_4Ga_4P_{12}C_5B_{5.5}$ BMG ($\sigma_f = 3.27$ GPa), the values of fracture strain are superior for the crystalline alloys.

A completely different mechanical behavior was observed for the monolithic alloys (A1) and (B1). Subjected to compressive loading such alloys display an amazing capacity for plastic deformation ($\varepsilon_f > 140\%$).

The structural observations performed for Ga-containing samples with composite structure (A2), (B2), (C) and (D) reveal the coexistence of a ductile Ga-enriched dendritic phase in combination with high strength Cr- and Mo-enriched interdendritic phases. Hence, the resulting mechanical behavior can be explained as being due to the formation of a composite material with a specific complex crystalline structure. The combination of ductile and high strength precipitates is responsible for the excellent mechanical properties.

Due to the fact, that the soft reinforcing austenitic phase was found to be Ga-enriched the main attention has been posed on clarifying the role of this element in enhancing the plasticity of the studied alloys. It was expected that the modifications of the chemical composition will lead to changes in the microstructure and, therefore, in the mechanical response of the alloys. Surprisingly, the combined results obtained from the

carried out investigations clearly indicate that the Ga substitution does not cause significant differences in the phase formation, which occurs upon casting. On the other hand, a strong increase of the hardness of the matrix phase for the as-cast sample (F) $(Fe_{89.0}Cr_{5.5}Mo_{5.5})_{83}C_{17}$ (10.7 GPa) with respect to its Ga-comprising counterpart (7.3 GPa) was observed. In general, it was found, that in the case of the alloys with higher C concentration, Ga additions lead to a tremendous improvement of the plasticity. While the as-cast $(Fe_{89.0}Cr_{5.5}Mo_{5.5})_{83}C_{17}$ rod exhibits about 5% strain up to failure, the as-cast $(Fe_{84.4}Cr_{5.2}Mo_{5.2}Ga_{5.2})_{83}C_{17}$ sample shows about 16% strain in the compression test ($\varepsilon_f$ is three times higher). In turn, the apparent fracture strength is nearly the same, i.e. $\sigma_f = 3.3$ GPa for $(Fe_{89.0}Cr_{5.5}Mo_{5.5})_{83}C_{17}$ and $\sigma_f = 3.0$ GPa for $(Fe_{84.4}Cr_{5.2}Mo_{5.2}Ga_{5.2})_{83}C_{17}$. These findings can be explained as being due to the specific interaction between the soft f.c.c. γ-Fe dendrites and the hard interdendritic phases, as observed for the Fe-based compositions. In the case of the alloys (C), (D) and (E), the dendritic phase acts as an obstacle for the crack propagation and, therefore, causes the pronounced strain-hardening. These composites are characterized by their excellent mechanical properties: high strength (from the matrix) connected with very good plasticity (from the dendrites). Contrary, such a strengthening effect has not been observed for the as-cast $(Fe_{89.0}Cr_{5.5}Mo_{5.5})_{83}C_{17}$ cylinder. The detailed studies on its fracture behavior have revealed that the cracks initiated during plastic deformation proceed through the austenitic phase. The γ-Fe dendrites do not hinder crack propagation. Taking into account all results discussed, it is evident that only appropriate alloying additions (Ga and C) lead to the improvement of the mechanical properties of the complex Fe-based materials developed here.

## 5.2 Future trends

*"Compressive „ductility" is not necessarily valid or even very interesting without corresponding measurements in tension"* – due to this fact, further, extensive studies (tensile tests) of the mechanical behavior of the presented multi-component Fe-based alloys are highly required.

Moreover, the concepts for improving the strength-plasticity balance (e.g. composite structure formation) should be further developed. As it has already been recognized, tailorable mechanical properties (strength, hardness, ductility) can be

obtained for instance from *in-situ* BMG composites by applying proper processing methods and tuned-in compositions to change the size and the volume fraction of the second phase dispersions [Eck07b]. In order to optimize the properties of the examined complex Fe-based materials, further investigations regarding the alloy design and the processing conditions must be carried out.

Finally, the thermal stability of the martensite-containing alloys should be elucidated in detail. To provide accurate information on the microstructure evolution upon heating, detailed experiments such as in-situ XRD, volume fraction estimation – Rietveld method, TEM observations are yet to be performed.

# List of references

[And79]     P. W. Anderson, *Lectures on Amorphous Systems*, *III-Condensed Matter*, edited by R. Balian, R. Maynard, and G. Toulouse, North-Holland, Amsterdam (1979).

[Ang91]     C. A. Angell, *Relaxation in liquids, polymers and plastic crystals – strong/fragile patterns and problems*, J. Non-Cryst. Solids **131-133**, 13 (1991).

[Arg79]     A. S. Argon, *Plastic deformation in metallic glasses*, Acta Metall. **27**, 47 (1979).

[Arg82]     A. S. Argon, *Mechanism of inelastic deformation in metallic glasses*, J. Phys. Chem. Solids **43**, 945 (1982).

[Ash06]     M. F. Ashby, and A. L. Greer, *Metallic glasses as structural materials*, Scripta Mater. **54**, 321 (2006).

[Ask03]     D. R. Askeland, and P. P. Phulé, *The Science and Engineering of Materials*, Thomson Brooks/Cole, USA (2003).

[Bat07]     L. Battezatti, A. Castellero, and P. Rizzi, *On the glass transition in metallic melts*, J. Non-Cryst. Solids **353**, 3318 (2007).

[Bia04]     Z. Bian, J. Ahmad, W. Zhang, and A. Inoue, *In situ formed $(Cu_{0.6}Zr_{0.25}Ti_{0.15})_{93}Nb_7$ bulk metallic glass composites*, Mater. Trans. JIM **45**, 2346 (2004).

[Bia05]     Z. Bian, H. Kato, C. L. Qin, W. Zhang, and A. Inoue, *Cu-Hf-Ti-Ag-Ta bulk metallic glass composites and their properties*, Acta Mater. **53**, 2037 (2005).

[Bil96]     H. Biloni, and W. J. Boettinger, *Chapter 8: Solidification*, in *Physical Metallurgy*, edited by R. W. Cahn, and P. Hassen, North-Holland, Amsterdam (1996).

[Bok05]     B. S. Bokstein, M. I. Mendelev, and D. J. Srolovitz, *Thermodynamics and Kinetics in Materials Science*, Oxford University Press Inc., New York (2005).

## List of references

[Bou05]    N. Boucharat, R. Hebert, H. Rösner, R. Valiev, and G. Wilde, *Nanocrystallization of amorphous $Al_{88}Y_7Fe_5$ alloy induced by plastic deformation*, Scripta Mater. **53**, 823 (2005).

[Bra05]    D. J. Branagan, *Enabling factors toward production of nanostructured steel on an industrial scale*, J. Mater. Eng. Perform. **14**, 5 (2005).

[Bus07]    R. Busch, J. Schroers, and W. H. Wang, *Thermodynamics and kinetics of bulk metallic glasses*, in *Bulk metallic glasses as new structural materials: Fundamentals and applications*, edited by A. L. Greer, and E. Ma, MRS Bulletin **32**, 620 (2007).

[Cah93]    R. W. Cahn, *Metallic Glasses*, in *Materials Science and Technology*: *A comprehensive treatment*, edited by R. W. Cahn, P. Haasen, and E. J. Kramer, Volume 9, WILEY-VCH, Weinheim (1993).

[Cai08]    A. H. Cai, H. Chen, W.-K. An, J.-Y. Tan, Y. Zhou, Y. Pan, and G.-X. Sun, *Melting enthalpy $\Delta H_m$ for describing glass forming ability of bulk metallic glasses*, J. Non-Cryst. Solids **354**, 1808 (2008).

[Cal03]    M. Calin, J. Eckert, and L. Schultz, *Improved mechanical behavior of Cu-Ti-based bulk metallic glasses by in-situ formation of nanoscale precipitates*, Scripta Mater. **48**, 653 (2003).

[Cal07]    M. Calin, L. C. Zhang, and J. Eckert*, Tailoring of microstructure and mechanical properties of a Ti-based bulk metallic glass-forming alloy*, Scripta Mater. **57**, 1101 (2007).

[Cha09]    Z. Y. Chang, X. M. Huang, L. Y. Chen, M. Y. Ge, Q. K. Jiang, X. P. Nie, and J. Z. Jiang, *Catching Fe-based bulk metallic glass with combination of high glass forming ability, ultrahigh strength and good plasticity in Fe-Co-Nb-B system*, Mater. Sci. Eng. A **517**, 246 (2009).

[Che69]    H. S. Chen, and D. Turnbull, *Formation, stability and structure of palladium-silicon based alloy glasses*, Acta Metall. **17**, 1021 (1969).

[Che70]    H. S. Chen, and C. E. Miller, *A rapid quenching technique for the preparation of thin uniform films of amorphous solids*, Rev. Sci. Instrum. **41**, 1237 (1970).

[Che75]    H. S. Chen, J. T. Krause, and E. Coleman, *Elastic constants, hardness and*

*their implications to flow properties of metallic glasses*, J. Non-Cryst. Solids **18**, 157 (1975).

[Coh59]    M. H. Cohen, and D. Turnbull, *Molecular transport in liquids and glasses*, J. Chem. Phys. **31**, 1164 (1959).

[Coh61]    M. H. Cohen, and D. Turnbull, *Composition requirements for glass formation in metallic and ionic systems*, Nature **189**, 131 (1961).

[Cot55]    A. H. Cottrell, *Theoretical Structural Metallurgy*, Edward Arnold, London, (1955).

[Das03a]   J. Das, W. Löser, U. Kühn, J. Eckert, S. K. Roy, and L. Schultz, *High-strength Zr-Nb-(Cu,Ni,Al) composites with enhanced plasticity*, Appl. Phys. Lett. **82**, 4690 (2003).

[Das03b]   J. Das, A. Güth, H-J. Klauss, C. Mickel, W. Löser, J. Eckert, S. K. Roy, and L. Schultz, *Effect of casting conditions on microstructure and mechanical properties of high-strength $Zr_{73.5}Nb_9Cu_7Ni_1Al_{9.5}$ in situ composites*, Scripta Mater. **49**, 1189 (2003).

[Das03c]   J. Das, *Novel Zr-based Nanostructure-Dendrite Composites with Enhanced Plasticity*, Master thesis, TU Dresden (2003).

[Das05]    J. Das, M. B. Tang, K. B. Kim, R. Theissmann, F. Baier, W. H. Wang, and J. Eckert, *"Work-Hardenable" ductile bulk metallic glass*, Phys. Rev. Lett. **94**, 205501 (2005).

[Das06]    J. Das, K. B. Kim, W. Xu, B. C. Wei, Z. F. Zhang, W. H. Wang, S. Yi, and J. Eckert, *Ductile metallic glasses in supercooled martensitic alloys*, Mater. Trans. JIM **47**, 2606 (2006).

[Das07]    J. Das, S. Pauly, C. Duhamel, B. C. Wei, and J. Eckert, *Microstructure and mechanical properties of slowly cooled $Cu_{47.5}Zr_{47.5}Al_5$*, J. Mater. Res. **22**, 326 (2007).

[Dav83]    H. A. Davis, *Chapter 2*: *Metallic Glass Formation*, in *Amorphous Metallic Alloys*, edited by F. E. Luborsky, Butterworths, London (1983).

[Deb01]    P. G. Debenedetti, and F. H. Stillinger, *Supercooled liquids and the glass transition*, Nature **410**, 259 (2001).

[Del04]    S. Deledda, *Mechanically Alloyed $Zr_{55}Cu_{30}Al_{10}Ni_5$ Glassy Matrix*

*Composites Containing ZrC Second-Phase Particles*, PhD thesis, TU Dresden (2004).

[Din05]     G. P. Dinda, H. Rösner, and G. Wilde, *Synthesis of bulk nanostructured Ni, Ti and Zr by repeated cold-rolling*, Scripta Mater. **52**, 577 (2005).

[Don89]     P. E. Donovan, *A yield criterion for Pd$_{40}$Ni$_{40}$P$_{20}$ metallic glass*, Acta Mater. **37**, 445 (1989).

[Dua08]     G. Duan, K. De Blauwe, M. L. Lind, J. P. Schramm, and W. L. Johnson, *Compositional dependence of thermal, elastic, and mechanical properties in Cu-Zr-Ag bulk metallic glasses*, Scripta Mater. **58**, 159 (2008).

[Duw60]     P. Duwez, R. H. Willens, and W. Klement, *Continuous series of metastable solid solutions in silver-copper alloys*, J. Appl. Phys. **31**, 1136 (1960).

[Duw65]     P. Duwez, R. H. Willens, and R. C. Crewdson, *Amorphous phase in palladium-silicon alloys*, J. Appl. Phys. **36**, 2267 (1965).

[Duw67]     P. Duwez, and S. C. H. Lin, *Amorphous ferromagnetic phase in iron-carbon-phosphorous alloys*, J. Appl. Phys. **38**, 4096 (1967).

[Eck97]     J. Eckert, *Mechanical alloying of highly processable glassy alloys*, Mater. Sci. Eng. A **226**, 364 (1997).

[Eck98]     J. Eckert, N. Mattern, M. Zinkevitch, and M. Seidel, *Crystallization behavior and phase formation in Zr-Al-Cu-Ni metallic glass containing oxygen*, Mater. Trans. JIM **39**, 623 (1998).

[Eck01]     J. Eckert, U. Kühn, N. Mattern, A. Reger-Leonhard, and L. Heilmaier, *Bulk nanostructured Zr-based multiphase alloys with high strength and good ductility*, Scripta Mater. **44**, 1587 (2001).

[Eck02]     J. Eckert, U. Kühn, N. Mattern, G. He, and A. Gebert, *Structural bulk metallic glasses with different length-scale of constituent phases*, Intermetal. **10**, 1183 (2002).

[Eck07a]    J. Eckert, J. Das, W. Löser, S. K. Roy, and A. Gebert, *Strengthening of multicomponent glass-forming alloys by microstructure design*, J. Non-Cryst. Solids **353**, 3742, (2007)

[Eck07b]    J. Eckert, J. Das, S. Pauly, and C. Duhamel, *Mechanical properties of bulk*

*metallic glasses and composites*, J. Mater. Res. **22**, 285 (2007).

[Ega83]     T. Egami, *Chapter 7: Atomic Short-Range Ordering in Amorphous Metal Alloys*, edited by F. E. Luborsky, Butterworths Monographs in Materials, London (1983).

[Ell90]     S. R. Elliot, *Physics of Amorphous Materials*, John Wiley & Sons, Inc., New York (1990).

[Fal98]     M. L. Falk, and J. S. Langer, *Dynamics of viscoplastic deformation in amorphous solids*, Phys. Rev. E **57**, 7192 (1998).

[Fan02]     C. Fan, R. T. Ott, and T. C. Hufnagel, *Metallic glass matrix composite with precipitated ductile reinforcement*, Appl. Phys. Lett. **81**, 1020 (2002).

[Fan09]     J. T. Fan, Z. F. Zhang, S. X. Mao, B. L. Shen, and A. Inoue, *Deformation and fracture behaviors of Co-based metallic glass and its composite with dendrites*, Intermetal. **17**, 445 (2009).

[Fec95]     H. J. Fecht, *Thermodynamic properties of amorphous solids – glass formation and glass transition – (Overview)*, Mater. Trans. JIM **36**, 777 (1995).

[Fuj06]     K. Fujita, T. Hashimoto, W. Zhang, N. Nishiyama, C. Ma, H. Kimura, and A. Inoue, *Fatigue strength in nanocrystalline Ti- and Cu-based bulk metallic glasses*, J. JIM **70**, 816 (2006).

[Ful25]     G. S. Fulcher, *Analysis of recent measurements of the viscosity of glasses*, J. Am. Ceram. **8**, 339 (1925).

[Geb98]     A. Gebert, J. Eckert, and L. Schultz, *Effect of oxygen on phase formation and thermal stability of slowly cooled $Zr_{65}Al_{7.5}Cu_{7.5}Ni_{10}$ metallic glass*, Acta Mater. **46**, 5475 (1998).

[Gil73]     J. J. Gilman, *Flow via dislocation in ideal glasses*, J. Appl. Phys. **44**, 675 (1973).

[Gil97]     C. Gilbert, R. O. Ritchie, and W.L. Johnson, *Fracture toughness and fatigue crack propagation in a Zr-Ti-Ni-Cu-Be bulk metallic glass*, Appl. Phys. Lett. **71**, 476 (1997).

[Got07]     G. Gottstein, *Physikalische Grundlagen der Materialkunde*, Springer-Verlag Berlin Heidelberg (2007).

[Gre07]     A. L. Greer, and E. Ma, *Bulk metallic glasses: At the cutting edge of metals research*, in *Bulk metallic glasses as new structural materials: Fundamentals and applications*, edited by A. L. Greer, and E. Ma, MRS Bulletin **32**, 611 (2007).

[Gu07]      X. J. Gu, S. J. Poon, and G. J. Shiflet, *Mechanical properties of iron-based bulk metallic glasses*, J. Mater. Res. **22**, 344 (2007).

[Guo05]     F. Q. Guo, H. J. Wang, S. J. Poon, and G. J. Shiflet, *Ductile titanium-based glassy alloy ingots*, Appl. Phys. Lett. **86**, 091907 (2005).

[Haa05]     P. Haasen, *Phase Transformation in Materials*, in *Materials Science and Technology*: *A Comprehensive Treatment*, edited by R. W. Cahn, P. Haasen, and E. J. Kramer, Volume 5, WILEY-VCH, Weinheim (2005).

[Han07]     Z. Han, J. Zhang, and Y. Li, *Quaternary Fe-based bulk metallic glasses with diameter of 5 mm*, Intermetal. **15**, 1447 (2007).

[Haj06]     K. Hajlaoui, A. R. Yavari, B. Doisneau, A. Le Moulec, W. J. Botta, G. Vaughan, A. L. Greer, A. Inoue, W. Zhang, and A. Kvick, *Shear delocalization and crack blunting of a metallic glass containing nanoparticles: In situ deformation in TEM analysis*, Scripta Mater. **54**, 1829 (2006).

[Haj07]     K. Hajlaoui, A. R. Yavari, A. Le Moulec, W. J. Botta, G. Vaughan, J. Das, A. L. Greer, and A. Kvick*, Plasticity induced by nanoparticle dispersions in bulk metallic glasses*, J. Non-Cryst. Solids **353**, 327 (2007).

[Hay00]     C. C. Hays, C. P. Kim, and W. L. Johnson, *Microstructure controlled shear pattern formation and enhanced plasticity of bulk metallic glasses containing in situ formed ductile phase dendrite dispersions*, Phys. Rev. Lett. **84**, 2901 (2000).

[He03a]     G. He, J. Eckert, W. Löser, and L. Schultz, *Novel Ti-base nanostructure-dendrite composite with enhanced plasticity*, Nat. Mater. **2**, 33 (2003).

[He03b]     G. He, W. Löser, J. Eckert, and L. Schultz, *Improved mechanical behavior of Cu-Ti-based bulk metallic glass by in situ formation of nanoscale precipitates*, Scripta Mater. **48**, 653 (2003).

[Hol53]     J. H. Hollomon, and D. Turnbull, *Nucleation*, Progress in Metal Physics **4**,

333 (1953).

[Hoo96]      R. Hooker, *Civilization in Africa: The Iron Age South of the Sahara*, Washington State University (1996).

[Ino89]      A. Inoue, T. Zhang, and T. Masumoto, *Al-La-Ni amorphous alloys with a wide supercooled liquid region*, Mater. Trans. JIM **30**, 965 (1989).

[Ino90a]     A. Inoue, H. Yamaguchi, T. Zhang, and T. Masumoto, *Al-La-Cu amorphous alloys with a wide supercooled liquid region*, Mater. Trans. JIM **31**, 104 (1990).

[Ino90b]     A. Inoue, T. Zhang, and T. Masumoto, *Zr-Al-Ni amorphous alloys with high glass transition temperature and significant supercooled liquid region*, Mater. Trans. JIM **31**, 177 (1990).

[Ino91]      A. Inoue, A. Kato, T. Zhang, S. G. Kim, and T. Masumoto, *Mg-Cu-Y amorphous alloys with high mechanical strength produced by a metallic mold casting method*, Mater. Trans. JIM **32**, 609 (1991).

[Ino93a]     A. Inoue, T. Zhang, N. Nishiyama, K. Ohba, and T. Masumoto, *Preparation of 16 mm diameter rod of amorphous $Zr_{65}Al_{7.5}Ni_{10}Cu_{17.5}$ alloy*, Mater. Trans. JIM **34**, 1234 (1993).

[Ino93b]     A. Inoue, T. Zhang, and T. Masumoto, *Glass forming ability of alloys*, J. Non-Cryst. Solids **156-158**, 473 (1993).

[Ino95]      A. Inoue, and J. S. Gook, *Fe-based ferromagnetic glassy alloys with wide supercooled liquid region*, Mater. Trans. JIM **36**, 1180 (1995).

[Ino96]      A. Inoue, N. Nishiyama, and T. Matsuda, *Preparation of bulk glassy $Pd_{40}Ni_{10}Cu_{30}P_{20}$ alloy of 40 mm in diameter by water quenching*, Mater. Trans. JIM **37**, 181 (1996).

[Ino97]      A. Inoue, and N. Nishiyama, *Extremely low critical cooling rates of new Pd-Cu-P base amorphous alloys*, Mater. Sci. Eng. A **226-228**, 401 (1997).

[Ino00]      A. Inoue, *Stabilization of metallic supercooled liquid and bulk amorphous alloys*, Acta Mater. **48**, 279 (2000).

[Ino01]      A. Inoue, *Bulk amorphous and nanocrystalline alloys with high functional properties*, Mater. Sci. Eng. A **304-306**, 1 (2001).

[Ino02]      A. Inoue, and A. Takeuchi, *Recent Progress in Bulk Glassy Alloys*, Mater.

Trans. JIM **43**, 1892 (2002).

[Ino03a]     A. Inoue, B. L. Shen, H. Koshiba, H. Kato, and A. R. Yavari, *Cobalt-based bulk glassy alloy with ultrahigh strength and soft magnetic properties*, Nature Mater. **2**, 661 (2003).

[Ino03b]     A. Inoue, B. L. Shen, A. R. Yavari, and A. L. Greer, *Mechanical properties of Fe-based bulk glassy alloys in Fe-B-Si-Nb and Fe-Ga-P-C-B-Si system*, J. Mater. Res. **18**, 1487 (2003).

[Ino04a]     A. Inoue, B. L. Shen, and C. T. Chang, *Super-high strength of over 4000 MPa for Fe-based bulk glassy alloys in $[(Fe_{1-x}Co_x)_{0.75}B_{0.2}Si_{0.05}]_{96}Nb_4$ system*, Acta Mater. **52**, 4093 (2004).

[Ino04b]     A. Inoue, and B. L. Shen, *A new Fe-based bulk glassy alloy with outstanding mechanical properties*, Adv. Mater. **16**, 2189 (2004).

[Ino05]      A. Inoue, W. Zhang, T. Tsurui, A. R. Yavari, and A. L. Greer, *Unusual room-temperature compressive plasticity in nanocrystal-toughened bulk copper-zirconium glass*, Philos. Mag. Lett. **85**, 221 (2005).

[Jäc86]      J. Jäckle, *Models of the glass transition*, Rep. Prog. Phys. **49**, 171 (1986).

[Joh99]      W. L. Johnson, *Bulk glass-forming metallic alloys: Science and technology*, MRS Bulletin **24**, 42 (1999).

[Kau48]      W. Kauzmann, *The nature of the glassy state and the behavior of liquids at low temperatures*, Chem. Rev. **43**, 219 (1948).

[Kim90]      S. G. Kim, A. Inoue, and T. Masumoto, *High mechanical strengths of Mg-Ni-Y and Mg-Cu-Y amorphous alloys with significant supercooled liquid region*, Mater. Trans. JIM **31**, 929 (1990).

[Kim06]      K. B. Kim, J. Das, F. Baier, M. B. Tang, W. H. Wang, and J. Eckert, *Heterogeneity of a $Cu_{47.5}Zr_{47.5}Al_5$ bulk metallic glass*, Appl. Phys. Lett. **88**, 051911 (2006).

[Kit05]      Ch. Kittel, *Introduction to Solid Sate Physics*, John Wiley & Sons, Inc., New York (2005).

[Kle60]      W. Klement, R. H. Willens, and P. Duwez, *Non-crystalline structure in solidified gold-silicon alloys*, Nature **187**, 896 (1960).

[Kös80]      U, Köster, and U. Herold, *Crystallization of Metallic Glasses*, in *Glassy

*Metals I*, Springer-Verlag, Heidelberg (1980).

[Kös96]     U. Köster, J. Meinhardt, S. Roos, and H. Liebertz, *Formation of quasicrystals in bulk glass forming Zr-Cu-Ni-Al alloys*, Appl. Phys. Lett. **69**, 179 (1996).

[Krs81]     V. V. Krstic, P.S. Nicholson, and R. G. Hoagland, *Toughening of glasses by metallic particles*, J. Am. Ceram. Soc. **64**, 499 (1981).

[Kui84]     H. W. Kui, A. L. Greer, and D. Turnbull, *Formation of bulk metallic glass by fluxing*, Appl. Phys. Lett. **45**, 615 (1984).

[Kus06]     M. Kusy, U. Kühn, A. Concustell, A. Gebert, J. Das, J. Eckert, L. Schultz, and M. D. Baro, *Fracture surface morphology of compressed bulk metallic glass-matrix-composites and bulk metallic glass*, Intermetal. **14**, 982 (2006).

[Küh00]     U. Kühn, J. Eckert, and L. Schultz, *As-cast quasicrystalline phase in a Zr-based multicomponent bulk alloy*, Appl. Phys. Lett. **77**, 3176 (2000).

[Küh02]     U. Kühn, J. Eckert, N. Mattern, and L. Schultz, *ZrNbCuNiAl bulk metallic glass matrix composites containing dendritic bcc phase precipitates*, Appl. Phys. Lett. **80**, 4525 (2002).

[Küh05]     U. Kühn, J. Eckert, S. Scudino, A. Gebert, N. Radke, N. Mattern, and L. Schultz, *Formation of quasicrystals in Zr-Ti-Nb-Cu-Ni-Al alloys by casting or annealing*, Journal of Metastable and Nanocrystalline Materials **24-25**, 511 (2005).

[Küh07]     U. Kühn, N. Mattern, T. Gemming, U. Siegel, K. Werniewicz, and J. Eckert, *Superior mechanical properties of FeCrMoVC*, Appl. Phys. Lett. **90**, 261901 (2007).

[Lan01]     J. S. Langer, *Microstructural shear localization in plastic deformation of amorphous solids*, Phys. Rev. E **64**, 011504 (2001).

[Lee04]     M. L. Lee, Y. Li, and C. A. Schuh, *Effect of controlled volume fraction of dendritic phases on tensile and compressive ductility in La-based metallic glass matrix composites*, Acta Mater. **52**, 4121 (2004).

[Lee05]     J. C. Lee, Y. C. Kim, J. P. Ahn, and H. S. Kim, *Enhanced plasticity in a bulk amorphous matrix composite: macroscopic and microscopic*

*viewpoint studies*, Acta Mater. **53**, 129 (2005).

[Lee06]    K. A. Lee, Y. C. Kim, J. H. Kim, C. S. Lee, J. Namkung, and M. C. Kim, *Mechanical properties of Fe–Ni–Cr–Si–B bulk glassy alloy*, Mater. Sci. Eng. A **449-451**, 181 (2006).

[Lee06]    S.-W. Lee, M.-Y. Huh, S.-W. Chae, and J.C. Lee, *Mechanism of the deformation-induced nanocrystallization in a Cu-based bulk amorphous alloy under uniaxial compression*, Scripta Mater. **54**, 1439 (2006).

[Len90]    Y. Leng, and T. H. Courtney, *Fracture behavior of laminated metal-metallic glass composite*, Metall. Trans. A **21**, 2159 (1990).

[Lew05]    J. J. Lewandowski, W. H. Wang, and A. L. Greer*, Intrinsic plasticity or brittleness of metallic glasses*, Philos. Mag. Lett. **85**, 77 (2005).

[Li07]    Y. Li, S. J. Poon, G. J. Shiflet, J. Xu, D.H. Kim, and J. F. Löffler, *Formation of bulk metallic glasses and their composites*, in *Bulk metallic glasses as new structural materials: Fundamentals and applications*, edited by A. L. Greer, and E. Ma, MRS Bulletin **32**, 624 (2007).

[Li08]    S. Li, G. Xie, D. V. Louzguine-Luzgin, and A. Inoue, *Glass forming ability and mechanical properties of new Ni-based bulk metallic glasses*, Mater. Trans. **49**, 494 (2008).

[Liu07]    Y. H. Liu, G. Wang, M. X. Pan, P. Yu, D. Q. Zhao, and W. H. Wang, *Deformation behaviors and mechanism of Ni-Co-Nb-Ta bulk metallic glasses with high strength and plasticity*, J. Mater. Res. **22**, 869 (2007).

[Lu04]    Z. P. Lu, C. T. Liu, J. R. Thompson, and W. D. Porter, *Structural amorphous steels*, Phys. Rev. Lett. **92**, 245503 (2004).

[Löf00]    J. F. Löffler, S. Bossuyt, S. C. Glade, W. L. Johnson, W. Wagner, and P. Thiyagarajan, *Crystallization of bulk amorphous Zr-Ti(Nb)-Cu-Ni-Al*, Appl. Phys. Lett. **77**, 525 (2000).

[Löf03]    J. F. Löffler, *Bulk metallic glasses*, Intermetal. **11**, 529 (2003).

[Ma03]    H. Ma, J. Xu, and E. Ma, *Mg-based bulk metallic glass composites with plasticity and high strength*, Appl. Phys. Lett. **83**, 2793 (2003).

[Mas92]    T. B. Massalski, *Binary Alloy Phase Diagram*, Volume 1, ASM International, Materials Park, Ohio (1992).

[Mas71]     T. Masumoto, and R. Maddin, *The mechanical properties of palladium 20 at.% silicon alloy quenched from the liquid state*, Acta Metall. **19**, 725 (1971).

[Mas78]     T. Masumoto, and K. Hashimoto, *Chemical properties of amorphous metals*, Ann. Rev. Mater. Sci. **8**, 215 (1978).

[Men05]     H. Men, S. J. Pang, A. Inoue, and T. Zhang, *New Ti-based bulk metallic glasses with significant plasticity*, Mater. Trans. JIM **46**, 2218 (2005).

[Mir04]     D. B. Miracle, *A structural model for metallic glasses*, Nature Mater. **3**, 697 (2004).

[Mir07]     D. B. Miracle, T. Egami, K. M. Flores, and K. F. Kelton, *Structural aspects of metallic glasses*, in *Bulk metallic glasses as new structural materials: Fundamentals and applications*, edited by A. L. Greer, and E. Ma, MRS Bulletin **32**, 629 (2007).

[Mor79]     R. C. Morris, *Disclination-dislocation model of metallic glass structures*, J. Appl. Phys. **50**, 3250 (1979).

[Mug93]     H. Mughrabi, *Chapter 1: Microstructure and Mechanical Properties*, in *Materials Science and Technology*: *A Comprehensive Treatment*, edited by R. W. Cahn, P. Haasen, and E. J. Kramer, Volume 6, WILEY-VCH, Weinheim (1993).

[New05]     R. E. Newnham, *Properties of Materials*, OXFORD University Press, Oxford (2005).

[Owe85]     A. E. Owen, *The Glass Transition*, in *Amorphous Solids and the Liquid State*, edited by N. H. March, R. A. Street, and M. Tosi, Plenum Press, New York (1985).

[Pam74a]    C. A. Pampillo, and H. S. Chen, *Comprehensive plastic deformation of a bulk metallic glass*, Mater. Sci. Eng. **13**, 181 (1974).

[Pam74b]    C. A. Pampillo, and D. E. Polk, *The strength and fracture characteristics of Fe, Fe-Ni, and Ni-based glasses at various temperatures*, Acta Metall. **22**, 741 (1974).

[Par05]     E. S. Park, and D. H. Kim, *Formation of Mg-Cu-Ni-Ag-Zn-Y-Gd bulk glassy alloy by casting into cone-shaped copper mold in air* atmosphere, J.

Mater. Res. **20**, 1465 (2005).

[Par08]      J. M. Park, K. B. Kim, W. T. Kim, M. H. Lee, J. Eckert, and D. H. Kim, *High strength ultrafine eutectic Fe-Nb-Al composites with enhanced plasticity*, Intermetal. **16**, 642 (2008).

[Pek93]      A. Peker, and W. L. Johnson, *A highly processable metallic glass: $Zr_{41.2}Ti_{13.8}Cu_{12.5}Ni_{10.0}Be_{22.5}$*, Appl. Phys. Lett. **63**, 2342 (1993).

[Pek01]      E. Pekarskaya, C. P. Kim, and W. L. Johnson, *In situ transmission electron microscopy studies of shear bands in a bulk metallic glass based composite*, J. Mater. Res. **16**, 2513 (2001).

[Pel05]      A. D. Pelton, *Thermodynamics and Phase Diagrams of Materials*, in *Materials Science and Technology*: *A Comprehensive Treatment*, edited by R. W. Cahn, P. Haasen, and E. J. Kramer, Volume 5, WILEY-VCH, Weinheim (2005).

[Per98]      J. H. Perepezko, and G. Wilde, *Alloy metastability during nucleation-controlled reactions*, Ber. Bunsenges. Phys. Chem. **102**, 1074 (1998).

[Pic92]      E. B. Pickering, *Constitution and Properties of Steels*, in *Materials Science and Technology*: *A Comprehensive Treatment*, edited by R. W. Cahn, P. Haasen, and E. J. Kramer, Volume 7, WILEY-VCH, Weinheim (1992).

[Pol72]      D. E. Polk, and D. Turnbull, *Flow of melt and glass forms of metallic alloys*, Acta Metall. **20**, 493 (1972).

[Pon03]      V. Ponnambalam, S. J. Poon, and G. J. Shiflet, V. M. Keppens, R. Taylor, and G. Petculescu, *Synthesis of iron-based bulk metallic glasses as nonferromagnetic amorphous steel alloys*, Appl. Phys. Lett. **83**, 1131 (2003).

[Pon04]      V. Ponnambalam, S. J. Poon, and G. J. Shiflet, *Fe-based bulk metallic glasses with diameter thickness larger than one centimeter*, J. Mater. Res. **19**, 1320 (2004).

[Qia08]      J. B. Qiang, W. Zhang, and A. Inoue, *Formation and compression mechanical properties of Ni-Zr-Nb-Pd bulk metallic glasses*, J. Mater. Res. **23**, 1940 (2008).

List of references

[Rag75]    V. Raghavan, and M. Cohen, *Solid-State Phase Transformation*, in *Treatise on Solid State Chemistry*, edited by N. B. Hannay, Volume 5 entitled *Changes of State*, Plenum Press, New York (1975).

[Ray68]    R. Ray, B. C. Giessen, and N. J. Grant, *New non-crystalline phases in splat cooled transition metal alloys*, Scripta Metall. **2**, 357 (1968).

[Rie93]    H. Riedel, *Chapter 12: Fracture Mechanisms*, in *Materials Science and Technology*: *A Comprehensive Treatment*, edited by R. W. Cahn, P. Haasen, and E. J. Kramer, Volume 6, WILEY-VCH, Weinheim (1993).

[Ruh67]    R. C. Ruhl, B. C. Giessen, M. Cohen, and N. J. Grant, *New microcrystalline phases in the Nb-Ni and Ta-Ni systems*, Acta Metall. **15**, 1693 (1967).

[Sai99]    J. Saida, M. Matsushita, T. Zhang, A. Inoue, M. W. Chen, and T. Sakurai, *Precipitation of icosahedral phase from a supercooled liquid region in $Zr_{65}Cu_{7.5}Al_{7.5}Ni_{10}Ag_{10}$ metallic glass*, Appl. Phys. Lett. **75**, 3497 (1999).

[Sai03]    J. Saida, and A. Inoue, *Quasicrystals from glass devitrification*, J. Non-Cryst. Solids **317**, 97 (2003).

[Sch81]    H. Schmalzried, *Solid Sate Reactions*, Verlag Chemie, Weinheim (1981).

[Sch94]    L. Schultz, and J. Eckert, *Mechanically alloyed glassy metals*, in *Glassy Metals* III, *Topics in Applied Physics*, Springer-Verlag, Berlin, **72**, 69 (1994).

[Sch04]    J. Schroers, and W. L. Johnson, *Ductile bulk metallic glass*, Phys. Rev. Lett. **93**, 255506 (2004).

[Sch07]    C. A. Schuh, T. C. Hufnagel, and U. Ramamurty, *Mechanical behavior of amorphous alloys*, Acta Mater. **55**, 4067 (2007).

[Sco62]    G. D. Scott, K. R. Knight, J. D. Bernal, and J. Mason, *Radial distribution of random close packing of equal spheres*, Nature **194**, 956 (1962).

[Sco83]    M. G. Scott, *Chapter 10: Crystallization*, in *Amorphous Metallic Alloys*, edited by F. E. Luborsky, Butterworths Monographs in Materials, London (1983).

[Scu06a]   S. Scudino, J. Eckert, H. Breitzke, K. Lüders, and L. Schultz, *Influence of ball milling on quasicrystals formation in melt-spun Zr-based glassy*

*ribbons*, Philos. Mag. **86**, 367, 2006.

[Scu06b]   S. Scudino, J. Das, M. Stoica, K. B. Kim, M. Kusy, and J. Eckert, *High strength hexagonal structured dendritic phase reinforced Zr-Ti-Ni bulk alloy with enhanced ductility*, Appl. Phys. Lett. **88**, 201920 (2006).

[Sha72]   J. H. Sharp, *Section D: Physical Chemistry, Reaction Kinetics*, in *Differential Thermal Analysis*, edited by R. C. Mackenzie, Volume 2, Academic Press, New York (1972).

[She84]   D. Shechtman, I. Blech, D. Gratias, and J. W. Cahn, *Metallic phase with long-range orientational order and no translational symmetry*, Phys. Rev. Lett. **53**, 1951 (1984).

[She99]   T. D. Shen, and R. B. Schwarz, *Bulk ferromagnetic glasses prepared by flux melting and water quenching*, Appl. Phys. Lett. **75**, 49 (1999).

[She05]   J. Shen, Q. J. Chen, J. F. Sun, H. B. Fan, and G. Wang, *Exceptionally high glass-forming ability of an FeCoCrMoCBY alloy*, Appl. Phys. Lett. **86**, 151907 (2005).

[She05]   B. L. Shen, and A. Inoue, *(Fe,Co,Ni)-B-Si-Nb bulk glassy alloy with super-high strength and some ductility*, J. Mater. Res. **20**, 1 (2005).

[Spa77]   F. Spaepen, *A microscopic mechanism for steady-state inhomogeneous flow in metallic glasses*, Acta Metall. **25**, 407 (1977).

[Spa83]   F. Spaepen, and A. I. Taub, *Chapter 13: Flow and Fracture*, in *Amorphous Metallic Alloys*, edited by F. E. Luborsky, Butterworths Monographs in Materials, London (1983).

[Sta]   www.stahldat.de

[Ste82]   P. S. Steif, F. Spaepen, and J. W. Hutchinson, *Strain localization in amorphous metals*, Acta Metall. **30**, 447 (1982).

[Ste05]   W. Steurer, *Elements of Symmetry in Periodic Lattices, Quasicrystals*, in *Materials Science and Technology*: *A Comprehensive Treatment*, edited by R. W. Cahn, P. Haasen, and E. J. Kramer, Volume 1, WILEY-VCH, Weinheim (2005).

[Sto02]   M. Stoica, J. Degmova, S. Roth, J. Eckert, H. Grahl, L. Schultz, A. R. Yavari, A. Kvick, and G. Heunen, *Magnetic properties and phase*

*transformations of bulk amorphous Fe-Based alloys obtained by different techniques*, Mater. Trans. **43**, 1966 (2002).

[Sto04]   M. Stoica, J. Eckert, S. Roth, and L. Schultz, *Preparation of bulk amorphous Fe-Cr-Mo-Ga-P-C-B alloys by copper mold casting*, Mater. Sci. Eng. A **375-377**, 399 (2004).

[Sto05a]  M. Stoica, J. Eckert, S. Roth, Z. F. Zhang, L. Schultz, and W. H. Wang, *Mechanical behavior of $Fe_{65.5}Cr_4Mo_4Ga_4P_{12}C_5B_{5.5}$ bulk metallic glass*, Intermetal. **13**, 764 (2005).

[Sto05b]  M. Stoica, *Casting and Characterization of Fe-(Cr,Mo,Ga)-(P,C,B) Soft Magnetic Bulk Metallic Glasses*, PhD thesis, TU Dresden (2005).

[Sto08]   M. Stoica, K. Hajlaoui, J. Das, J. Eckert, and A. R. Yavari, *FeNbB bulk metallic glass with high boron content*, Rev. Adv. Mater. Sci. **18**, 61 (2008).

[Tam26]   V. G. Tamman, and H. Z. Hesse, *The dependence of viscosity upon the temperature of supercooled liquids*, Anorg. Allg. Chem. **19**, 245 (1926).

[Tan03]   H. Tan, Y. Zhang, D. Ma, Y. P. Feng, and Y. Li, *Optimum glass formation at off-eutectic composition and its relation to skewed eutectic coupled zone in the La-based La–Al–(Cu,Ni) pseudo ternary system*, Acta Mater. **51**, 4551 (2003).

[Tar09]   N. H. Tariq, B. A. Hasan, J. I. Akhter, and F. Ali, Mechanical and tribological properties of Zr–Al–Ni–Cu bulk metallic glasses, Journal of Alloys and Compounds **469**, 179 (2009).

[Tur61]   D. Turnbull, *The liquid state and the liquid-solid transition*, Transactions of the Metallurgical Society of AIME **221**, 422 (1961).

[Tur69]   D. Turnbull, *Under what conditions can a glass be formed?*, Contemp. Phys. **10**, 473 (1969).

[Tur70]   D. Turnbull, and M. H. Cohen, *On the free-volume model of the liquid-glass transition*, J. Chem. Phys. **52**, 3038 (1970).

[Vog22]   H. Vogel, *The law of the relation between the viscosity of liquids and the temperature*, Physikalische Zeitschrift **22**, 645 (1922).

[Wan06]    H. Wang, H. M. Fu, and H. F. Zhang, *In-situ Cu-based bulk metallic glass composites*, International Journal of Modern Physics B **20**, 3963 (2006).

[Wil05]    G. Wilde, G. P. Dinda, and H. Rösner, *Synthesis of bulk nanocrystalline materials by repeated cold rolling*, Adv. Eng. Mater. **7**, 11 (2005).

[Wil06]    G. Wilde, N. Boucharat, G. P. Dinda, H. Rösner, and R. Z. Valiev, *New routes for synthesizing massive nanocrystalline materials*, Mater. Sci. Forum **503-504**, 425 (2006).

[Wil07]    G. Wilde, N. Boucharat, R. Hebert, H. Rösner, and R. Z. Valiev, *New ways to obtain bulk nanostructured materials*, Mater. Sci. Eng. A **449-451**, 825 (2007).

[Woll05]   H. J. Wollenberger, *Point Defects in Crystals*, in *Materials Science and Technology*: *A Comprehensive Treatment*, edited by R. W. Cahn, P. Haasen, and E. J. Kramer, Volume 1, WILEY-VCH, Weinheim (2005).

[Xin99]    L. Q. Xing, J. Eckert, W. Löser, and L. Schultz, *High-strength materials produced by precipitation of icosahedral quasicrystals in bulk Zr-Ti-Cu-Ni-Al amorphous alloys*, Appl. Phys. Lett. **74**, 664 (1999).

[Yao06]    K. F. Yao, F. Ruan, Y. Q. Yang, and N. Chen, *Superductile bulk metallic glass*, Appl. Phys. Lett. **88**, 122106 (2006).

[Yav05]    A. R. Yavari, A. Le Moulec, A. Inoue, N. Nishiyama, N. Lupo, E. Matsubara, W. J. Botta, G. Vaughan, M. Di Michiel, and A. Kvick, *Excess free volume in metallic glasses measured by X-ray diffraction*, Acta Mater. 53, 1611 (2005).

[Yav07]    A. R. Yavari, J. J. Lewandowski, and J. Eckert, *Mechanical properties of bulk metallic glasses*, in *Bulk metallic glasses as new structural materials: Fundamentals and applications*, edited by A. L. Greer, and E. Ma, MRS Bulletin **32**, 635 (2007).

[You93]    R. A. Young, *The Rietveld Method*, Intern. Union of Crystallography, Oxford University Press, 1-298 (1993).

[Zha91]    T. Zhang, A. Inoue, and T. Masumoto, *Amorphous Zr-Al-TM (TM=Co, Ni, Cu) alloys with significant supercooled liquid region of over 100 K*, Mater. Trans. JIM **32**, 1005 (1991).

[Zha99]     T. Zhang, and A. Inoue, *Preparation of Ti-Cu-Ni-Si-B amorphous alloys with a large supercooled liquid region*, Mater. Trans., JIM **40**, 301 (1999).

[Zha07]     Z. F. Zhang, F. F. Wu, G. He, and J. Eckert, *Mechanical properties, damage and fracture mechanisms of bulk metallic glass materials*, J. Mater. Sci. Tech. **23**, 747 (2007).

List of references

# List of publications

1.  U. Kühn, A. Schlieter, U. Siegel, H. Wendrock, <u>K. Werniewicz</u>, L. Schultz and J. Eckert, *Microstructure and thermomechanical properties of FeCrMoVC*, RQ 13 (International Conference on the Rapidly Quenched and Metastable Materials), Dresden (2008).

2.  <u>K. Werniewicz</u>, U. Kühn, N. Mattern, B. Bartusch, J. Eckert, U. Siegel, L. Schultz and T. Kulik, *Fe-based materials with improved mechanical properties*, in Glass Materials Research Progress, Nova Publisher, Chapter 9, 259-274 (2008).

3.  <u>K. Werniewicz</u>, U. Kühn, N. Mattern, B. Bartusch, U. Siegel, L. Schultz and T. Kulik, *Advanced high-strength and ductile Fe-Cr-Mo-Ga-Si alloys*, ISMANAM-2006**,** Conference held Aug. 27-31, 2006 Warsaw/Poland, in Reviews on Advanced Materials Science; **18**, 140-143 (2008).

4.  U. Kühn, N. Mattern, T. Gemming, U. Siegel, <u>K. Werniewicz</u> and J. Eckert, *Superior mechanical properties of FeCrMoVC*, Appl. Phys. Lett. **90**, 261901 (2007).

5.  <u>K. Werniewicz</u>, U. Kühn, N. Mattern, B. Bartusch, J. Eckert, J. Das, U.Siegel, L. Schultz and T. Kulik, *Novel high-strength Fe-based composite materials with large plasticity*, in The World of Bulk Metallic Glasses and Their Composites, Published by Research Signpost, Chapter 3, 53-72 (2007).

6.  <u>K. Werniewicz</u>, U. Kühn, N. Mattern, B. Bartusch, J. Eckert, J. Das, L. Schultz and T. Kulik, *New Fe-Cr-Mo-Ga-C composites with high compressive strength and large plasticity*, Acta Mater. **55**, 3513-3520 (2007).

# List of publications

# ACKNOWLEDGEMENTS

I would like to express my sincerest thanks and gratitude to a number of people who encouraged me and who continuously supported me in making my dreams come true. I am extremely fortunate to work at the Leibniz-Institut für Festkörper- and Werkstoffforschung (IFW) Dresden, Germany. The financial support by Deutsche Forschungsgemeinschaft (DFG) in the framework of the project KU 1974/1-1 entitled „Hochfestigkeit and Duktilität von teilamorphen und nanostrukturierten vielkomponentigen Eisen-Basislegierungen" is gratefully acknowledged.

First and foremost I wish to thank my *Mentor* Prof. Ludwig Schultz for…

| | |
|---|---|
| *his trust* | thank you for giving me a chance to join your group at the IFW, |
| *invaluable scientific care* | he is an unending source of knowledge, his advices, comments, ideas, were guiding me during my entire PhD "journey", |
| *his wonderful personality* | his enthusiasm, optimism, endless vitality kept me going during the difficult days of my research, |
| *every single minute* | he spent on discussing with me important scientific as well as personal issues. |

This work would not have been accomplished without Dr. Uta Kühn who served as my supervisor. Most of the knowledge on bulk metallic glasses I have now was gained from discussions with Dr. Uta Kühn during the past years. She was my inspiration, her exceptional intuition, outstanding ideas, tremendous scientific and mental support have been decisive for this research. She has been for me an example of a successful, brilliant, hard-working, beautiful woman who is also a warm, wonderful person. It was a pleasure to be a part of her team.

My special thanks are due to Prof. Jürgen Eckert, who is a great expert in the field of metastable and nanostructured materials. The discussions I had with him have enabled

Hiermit versichere ich, dass ich die vorliegende Arbeit ohne unzulässige Hilfe Dritter und ohne Benutzung anderer als der angegebenen Hilfsmittel angefertigt habe; die aus fremden Quellen direkt oder indirekt übernommenen Gedanken sind als solche kenntlich gemacht.

Bei der Auswahl und Auswertung des Materials sowie bei der Herstellung des Manuskripts habe ich Unterstützungsleistungen von folgenden Personen erhalten: Prof. Dr. Ludwig Schultz, Dr. Uta Kühn, Prof. Dr. Jürgen Eckert. Weitere Personen waren an der geistigen Herstellung der vorliegenden Arbeit nicht beteiligt. Insbesondere habe ich nicht die Hilfe eines kommerziellen Promotionsberaters in Anspruch genommen.

Dritte haben von mir keine geldwerten Leistungen für Arbeiten erhalten, die in Zusammenhang mit dem Inhalt der vorgelegten Dissertation stehen. Die Arbeit wurde bisher weder im Inland noch im Ausland in gleicher oder ähnlicher Form einer anderen Prüfungsbehörde vorgelegt und ist auch noch nicht veröffentlicht worden.

Ich erkenne die Promotionsordnung der Fakultät Maschinenwesen der TU Dresden an.

Weiterhin erkläre ich, bei der zuständigen Meldebehörde ein Führungszeugnis beantragt zu haben.


Dresden, 05.01.2010                                                    Katarzyna Werniewicz